



U.S. Department of Energy  
**Energy Efficiency  
and Renewable Energy**

Bringing you a prosperous future where energy  
is clean, abundant, reliable, and affordable

**Industrial Technologies Program**  
**Industrial Materials for the Future**

Final Technical Report

***Physical and Numerical Analysis of  
Extrusion Process for Production of  
Bimetallic Tubes***

August 2006

**Principal Investigators:**

Wojciech Z. Misiolek  
*Lehigh University*

Vinod K. Sikka  
*Oak Ridge National Laboratory*



OAK RIDGE NATIONAL LABORATORY

Managed by  
UT-Battelle, LLC

ORNL/TM-2006/72

## DOCUMENT AVAILABILITY

Reports produced after January 1, 1996, are generally available free via the U.S. Department of Energy (DOE) Information Bridge.

**Web site** <http://www.osti.gov/bridge>

Reports produced before January 1, 1996, may be purchased by members of the public from the following source.

National Technical Information Service

5285 Port Royal Road

Springfield, VA 22161

**Telephone** 703-605-6000 (1-800-553-6847)

**TDD** 703-487-4639

**Fax** 703-605-6900

**E-mail** [info@ntis.gov](mailto:info@ntis.gov)

**Web site** <http://www.ntis.gov/support/ordernowabout.htm>

Reports are available to DOE employees, DOE contractors, Energy Technology Data Exchange (ETDE) representatives, and International Nuclear Information System (INIS) representatives from the following source.

Office of Scientific and Technical Information

P.O. Box 62

Oak Ridge, TN 37831

**Telephone** 865-576-8401

**Fax** 865-576-5728

**E-mail** [reports@osti.gov](mailto:reports@osti.gov)

**Web site** <http://www.osti.gov/contact.html>

This report was prepared as an account of work sponsored by an agency of the United States Government. Neither the United States Government nor any agency thereof, nor any of their employees, makes any warranty, express or implied, or assumes any legal liability or responsibility for the accuracy, completeness, or usefulness of any information, apparatus, product, or process disclosed, or represents that its use would not infringe privately owned rights. Reference herein to any specific commercial product, process, or service by trade name, trademark, manufacturer, or otherwise, does not necessarily constitute or imply its endorsement, recommendation, or favoring by the United States Government or any agency thereof. The views and opinions of authors expressed herein do not necessarily state or reflect those of the United States Government or any agency thereof.

## FINAL TECHNICAL REPORT

**Project Title:** Physical and Numerical Analysis of Extrusion Process for Production of Bi-Metallic Tubes

**Award No.:** DE-FC36-01ID14254

**Project Period:** 09/30/2001 to 09/29/2005

**PI(s):** Dr. Wojciech Z. Misiolek  
(610) 758-4252  
wzm2@lehigh.edu

Dr. Vinod K. Sikka  
(865) 574-5112  
sikkavk@ornl.gov

**Additional Researchers:** Dr. Pawel Kazanowski  
Dr. Mario Epler  
Dr. Gail Ludtka

**Recipient Organization:** Lehigh University  
242 Whitaker Building  
Bethlehem, PA 18015-3195

**National Laboratory:** Oak Ridge National Laboratory  
One Bethel Valley Road  
P.O. Box 2008  
Oak Ridge, TN 37831

**Industrial Partners:** Altair Engineering, Inc.  
Dynamet Technology  
Energy Industries of Ohio  
Special Metals Corporation



**Physical and Numerical Analysis of Extrusion Process  
for Production of Bimetallic Tubes**

Wojciech Z. Misiolek  
*Lehigh University*

Vinod K. Sikka  
*Oak Ridge National Laboratory*

August 2006

Prepared by  
OAK RIDGE NATIONAL LABORATORY  
P.O. Box 2008  
Oak Ridge, Tennessee 37831-6283  
managed by  
UT-Battelle, LLC  
for the  
U.S. DEPARTMENT OF ENERGY  
under contract DE-AC05-00OR22725

## **Acknowledgments and Disclaimer**

### **Acknowledgments**

This report is based upon work supported by the U.S. Department of Energy, Energy Efficiency and Renewable Energy, Industrial Technologies Program, Industrial Materials for the Future, under Award No. DE-FC36-01ID14254.

Research at the Oak Ridge National Laboratory was sponsored by the U.S. Department of Energy, Office of Energy Efficiency and Renewable Energy, Industrial Technologies Program, under contract DE-AC05-00OR22725 with UT-Battelle, LLC. The authors wish to thank Dr. Peter Angelini for reviewing the document, Ms. Millie Atchley for preparation of documents, and Jeanne Dole for technical editing.

### **Disclaimer**

This report was prepared as an account of work sponsored by an agency of the United States Government. Neither the United States Government nor any agency thereof, nor any of their employees, makes any warranty, express or implied, or assumes any legal liability or responsibility for the accuracy, completeness, or usefulness of any information, apparatus, product, or process disclosed, or represents that its use would not infringe privately owned rights. Reference herein to any specific commercial product, process, or service by trade name, trademark, manufacturer, or otherwise, does not necessarily constitute or imply its endorsement, recommendation, or favoring by the United States Government or any agency thereof. The views and opinions of authors expressed herein do not necessarily state or reflect those of the United States Government or any agency thereof.

# Contents

|  |    |
|--|----|
| List of Figures .....  | v  |
| List of Tables.....  | ix |
| Abbreviations and Acronyms .....   | xi |
| 1. Executive Summary .....   | 1  |
| 1.1 Purpose .....  | 1  |
| 1.2 Research .....   | 1  |
| 1.3 Results .....  | 2  |
| 1.4 Conclusions .....  | 2  |
| 1.5 Accomplishments .....  | 3  |
| 1.6 Commercialization.....   | 3  |
| 2. Introduction .....  | 5  |
| 3. Background .....  | 7  |
| 3.1 Extrusion Process .....  | 7  |
| 3.1.1 Steel Extrusion.....   | 11 |
| 3.1.2 Diffusion and Co-extrusion Bonding: Microstructural Development .....                        | 20 |
| 3.1.3 Previous Work on Similar Alloy Systems .....   | 22 |
| 3.2 Modeling and Simulation .....  | 23 |
| 3.2.1 Finite Element Modeling .....  | 23 |
| 3.2.2 Thermomechanical Simulation.....   | 23 |
| 4. Results and Discussion.....   | 25 |
| 4.1 Billet Design for Extrusion of Bimetallic Tubes .....  | 25 |
| 4.1.1 Billet Materials and Chosen Conditions.....  | 25 |
| 4.1.2 Bimetallic Billet Assembly Procedure .....   | 25 |
| 4.1.3 Extrusion Conditions .....   | 28 |
| 4.1.4 Finite Element Modeling Simulation using DEFORM-2D and Experimental Validation (Case 1)..... | 29 |
| 4.1.5 Finite Element Modeling Simulation Using DEFORM-2D and Experimental Validation (Case 2)..... | 35 |
| 4.1.6 Discussion of Results for Finite Element Modeling Analysis of New Billet Design.....         | 44 |
| 4.1.7 Conclusions for Use of Finite Element Modeling Analysis for New Billet Design.....           | 46 |
| 4.2 Analysis of Eccentricity in Bimetallic Extruded Tubes.....                                     | 46 |
| 4.2.1 Eccentricity Measurements.....   | 47 |
| 4.2.2 Discussion of Eccentricity Observations .....  | 52 |
| 4.2.3 Conclusions from Eccentricity Analysis of Bimetallic Tubes.....                              | 53 |
| 4.3 Metallurgical Interface Development as a Result of Co-extrusion of Ferrous Material Tubes..... | 53 |
| 4.3.1 Compositions of Steels Used and Their Possible Effects on Interface.....                     | 54 |
| 4.3.2 Experimental Details for Interface Study .....   | 54 |
| 4.3.3 Finite Element Modeling.....   | 55 |
| 4.3.4 Gleeble Simulation of Extrusion Process .....  | 56 |

|       |   |    |
|-------|---|----|
| 4.3.5 | Microstructural Analysis.....                                       | 59 |
| 4.3.6 | Discussion of Results for Interface Study of Co-extruded Tubes..... | 73 |
| 4.3.7 | Conclusions from Interface Study of Co-extruded Tubes.....          | 79 |
| 5.    | Accomplishments.....  | 81 |
| 5.1   | Technical Accomplishments.....                                      | 81 |
| 5.2   | Publications and Presentations.....                                 | 82 |
| 5.3   | Development of Students.....  | 82 |
| 6.    | Summary and Conclusions.....  | 83 |
| 6.1   | Summary.....  | 83 |
| 6.2   | Conclusions.....  | 83 |
| 6.3   | Commercialization Aspects, Plans, Status, and Barriers.....         | 84 |
| 7.    | Recommendations.....  | 85 |
| 8.    | References.....   | 87 |
|       | Appendix: Farmer’s Marine Copper Works Letter.....                  | 89 |



## List of Figures

|      |  |    |
|------|--|----|
| 3.1  | Schematic load versus ram displacement curves for extrusion shows.....   | 9  |
| 3.2  | Eccentricity definitions for tubes .....   | 10 |
| 3.3  | Fe-C equilibrium phase diagram.....  | 12 |
| 3.4  | Vertical section of Fe-Ni-Cr ternary phase diagram at 70% Fe.....  | 13 |
| 3.5  | Schematic representation of the flow of material during direct extrusion through a flat face die .....   | 16 |
| 3.6  | Schematic representation of material flow in a bimetallic billet through a flat face die.....  | 17 |
| 3.7  | Types of flow behavior observed during the co-extrusion of a rod from a bimetallic billet .....  | 18 |
| 3.8  | Co-extruded rod of modeling material, hard core/soft sleeve, showing the core ballooning at the front of the extrudate (right) and core pinch-off at the back end (left) ..... | 18 |
| 3.9  | Schematic cross section of unextruded billet: (a) traditional design and (b) novel design with shortened core.....   | 19 |
| 3.10 | Stages of development in a diffusion bond.....   | 21 |
| 3.11 | Stages of development in a co-extruded bond .....  | 21 |
| 4.1  | Front of shrink fitted bimetallic billet before welding (full-length core).....  | 26 |
| 4.2  | Front end of bimetallic steel billet with full-length core and weld .....  | 26 |
| 4.3  | Front end of bimetallic steel billet with shortened core and weld .....  | 27 |
| 4.4  | Back side of bimetallic steel billet with welds, weld plate, and degassing tube.....   | 27 |
| 4.5  | Bimetallic billets being degassed.....   | 28 |
| 4.6  | Back side of bimetallic steel billet with welds, weld plate, and crimped-off degassing tube .....  | 28 |
| 4.7  | Comparison of average core thickness for the low extrusion ratio extrudates.....   | 29 |
| 4.8  | Comparison of average core thickness for the high extrusion ratio extrudates .....   | 30 |
| 4.9  | Finite element modeling versus actual average core thickness as a function of distance for sample Low1 .....   | 31 |
| 4.10 | Finite element modeling versus actual average core thickness as a function of distance for sample Low2 .....   | 31 |
| 4.11 | Finite element modeling versus actual average core thickness as a function of distance for sample Low3 .....   | 32 |
| 4.12 | Finite element modeling at early stage of extrusion and front-end geometry development for low extrusion ratio extrudates.....   | 32 |
| 4.13 | Finite element modeling versus actual average core thickness as a function of distance for sample High1 .....  | 33 |
| 4.14 | Finite element modeling versus actual average core thickness as a function of distance for sample High2 .....  | 33 |
| 4.15 | Finite element modeling versus actual average core thickness as a function of distance for sample High3 .....  | 34 |
| 4.16 | Finite element modeling at early stage of extrusion and front-end geometry development for high extrusion ratio extrudates.....  | 34 |
| 4.17 | Comparison of finite element modeling predicted core thickness for high extrusion ratio samples. Note that the graph has been truncated at 800 mm on the x-axis .....          | 35 |
| 4.18 | Comparison of average core thickness for the B-Series extrudates .....   | 36 |
| 4.19 | Comparison of average core thickness for the F-Series extrudates .....   | 37 |

|      |   |    |
|------|---|----|
| 4.20 | Finite element modeling versus actual average core thickness as a function of distance for Sample B1.....   | 37 |
| 4.21 | Finite element modeling at early stage of extrusion and front-end geometry development for Sample B1 .....  | 38 |
| 4.22 | Finite element modeling versus actual average core thickness as a function of distance for Sample B2.....   | 38 |
| 4.23 | Finite element modeling at early stage of extrusion and front-end geometry development for Sample B2 .....  | 39 |
| 4.24 | Finite element modeling versus actual average core thickness as a function of distance for Sample B3.....   | 39 |
| 4.25 | Finite element modeling at early stage of extrusion and front-end geometry development for Sample B3 .....  | 40 |
| 4.26 | Finite element modeling versus actual average core thickness as a function of distance for Sample F1 .....  | 41 |
| 4.27 | Finite element modeling at early stage of extrusion and front-end geometry development for Sample F1 .....  | 41 |
| 4.28 | Finite element modeling versus actual average core thickness as a function of distance for Sample F2.....   | 42 |
| 4.29 | Finite element modeling at early stage of extrusion and front-end geometry development for Sample F2 .....  | 42 |
| 4.30 | Finite element modeling versus actual average core thickness as a function of distance for Sample F3.....   | 43 |
| 4.31 | Finite element modeling at early stage of extrusion and front-end geometry development for Sample F3 .....  | 43 |
| 4.32 | Schematic representation of the cross section of a co-extruded tube showing orientation definitions and sleeve and core thickness designations.....       | 48 |
| 4.33 | Eccentricity of tube HighCore1 (extrusion ratio of 3.3, full-length core); percentage of error in wall thickness versus fraction of extrudate length..... | 49 |
| 4.34 | Eccentricity of tube HighCore2 (extrusion ratio of 3.3, 90% length core); percentage of error in wall thickness versus fraction of extrudate length.....  | 50 |
| 4.35 | Eccentricity of tube HighCore3 (extrusion ratio of 3.3, 80% length core); percentage of error in wall thickness versus fraction of extrudate length.....  | 50 |
| 4.36 | Eccentricity of tube LowCore1 (extrusion ratio of 10.6, full-length core); percentage of error in wall thickness versus fraction of extrudate length..... | 51 |
| 4.37 | Eccentricity of tube LowCore2 (extrusion ratio of 10.6, 90% length core); percentage of error in wall thickness versus fraction of extrudate length ..... | 51 |
| 4.38 | Eccentricity of tube LowCore3 (extrusion ratio of 10.6, 80% length core); percentage of error in wall thickness versus fraction of extrudate length ..... | 52 |
| 4.39 | Effective strain measurement from point tracking in finite element modeling of the Low1 sample .....  | 56 |
| 4.40 | Effective strain rate measurement from point tracking in finite element modeling of the Low1 sample .....   | 57 |
| 4.41 | Effective strain measurement from point tracking in finite element modeling of the High1 sample.....  | 57 |
| 4.42 | Effective strain rate measurement from point tracking in finite element modeling of the High1 sample.....   | 58 |
| 4.43 | Low strain/strain rate Gleeble sample furnace cool time versus temperature profile .....  | 58 |
| 4.44 | Banded pearlite in a longitudinal section of 1020 plain carbon steel stock material prior to processing: etched using 4% picral for 25 s .....            | 59 |

|      |   |    |
|------|---|----|
| 4.45 | Equiaxed austenite and delta ferrite in longitudinal section of stock 304 stainless steel material: electrolytically etched using 60% HNO <sub>3</sub> /40% H <sub>2</sub> O at 3V for 6 s.....   | 60 |
| 4.46 | Interface between (left) 1020 steel and (right) 304 stainless steel after 2.5 h at 1200°C: unetched.....  | 60 |
| 4.47 | Development stages in diffusional bonding/solid state welding.....  | 61 |
| 4.48 | Interface between (left) 1020 steel and (right) 304 stainless steel cut from the shrink-fit billet after 2.5 h at 1200°C; etched with agitated 60 mL HCl, 60 mL HNO <sub>3</sub> , and 60 mL distilled H <sub>2</sub> O for 30 s.....   | 61 |
| 4.49 | Interface between (left) 1020 steel and (right) 304 stainless steel after 2 h at 1100°C and co-extruded followed by air cool to room temperature.....   | 62 |
| 4.50 | Higher magnification of the interface between (left) 1020 steel and (right) 304 stainless steel after 2 h at 1100°C and co-extruded followed by air cool to room temperature.....   | 63 |
| 4.51 | Higher magnification of the interface between (left) 1020 steel and (right) 304 stainless steel after 2 h at 1100°C and co-extruded followed by air cool to room temperature.....   | 63 |
| 4.52 | Composite micrograph of the regions adjacent to the interface after extrusion with high extrusion ratio.....  | 64 |
| 4.53 | Transformation layer thickness measurements taken from the etched, extruded samples.....  | 64 |
| 4.54 | Gleeble samples for deformation simulation.....   | 65 |
| 4.55 | Interface between (left) 1020 steel and (right) 304 stainless steel after 2.5 h at 1200°C held at 100 lb-f in Gleeble Hydrowedge unit.....  | 65 |
| 4.56 | High magnification of the interface between (left) 1020 steel and (right) 304 stainless steel after 2.5 h at 1200°C held at 100 lb-f in Gleeble Hydrowedge unit and deformed to a strain of 2.74 at a strain rate of 22.8 s <sup>-1</sup> and air cooled.....                                 | 66 |
| 4.57 | Light optical micrograph of the interface between (left) 1020 steel and (right) 304 stainless steel after 2 h at 1100°C held at 100 lb-f in Gleeble Hydrowedge unit and deformed to a strain of 1.2 at a strain rate of 2.10 s <sup>-1</sup> and air cooled.....                              | 66 |
| 4.58 | Scanning electron microscopy secondary electron image of the interface between (left) 1020 steel and (right) 304 stainless steel after 2 h at 1100°C held at 100 lb-f in Gleeble Hydrowedge unit and deformed to a strain of 1.2 at a strain rate of 2.10 s <sup>-1</sup> and air cooled..... | 67 |
| 4.59 | Low strain/strain rate extrudate sample etched for 240 s using Murakami's reagent.....  | 68 |
| 4.60 | Low strain/strain rate Gleeble simulated sample etched for 240 s using Murakami's reagent.....  | 68 |
| 4.61 | Low strain/strain rate extrudate sample etched for 240 s using Murakami's reagent followed by 15 s using equal parts agitated H <sub>2</sub> O, HCl, and HNO <sub>3</sub> .....   | 69 |
| 4.62 | Low strain/strain rate Gleeble simulated sample etched for 240 s using Murakami's reagent followed by 15 s using equal parts agitated H <sub>2</sub> O, HCl, and HNO <sub>3</sub> .....   | 69 |
| 4.63 | Qualitative elemental maps of the interface of the low strain/strain rate extrudate.....  | 70 |
| 4.64 | Qualitative elemental maps of the interface of the Gleeble simulated low strain/strain rate extrudate.....  | 70 |
| 4.65 | Quantitative wavelength dispersive spectroscopy line scan across interface of sample subjected to 2 h at 1200°C in Gleeble and then is air cooled.....  | 71 |
| 4.66 | Quantitative wavelength dispersive spectroscopy line scan across interface of sample subjected to 2 h at 1100°C in Gleeble and deformed according to the low strain/strain rate sample and is furnace cooled.....   | 71 |
| 4.67 | Quantitative wavelength dispersive spectroscopy line scan across interface of extrudate that has a designated low strain/strain rate.....   | 72 |
| 4.68 | Electron backscatter diffraction phase map of interface.....  | 72 |

|      |   |    |
|------|---|----|
| 4.69 | Electron backscatter diffraction orientation map and inverse pole figure of the regions directly adjacent to the interface..... | 73 |
| 4.70 | Solvus curve for $\text{Cr}_{23}\text{C}_6$ in 304 stainless steel .....  | 77 |
| 4.71 | Microstructural development schematic for the co-extruded stainless and plain carbon steel .....                                | 79 |

## List of Tables

|     |  |    |
|-----|--|----|
| 3.1 | Flow stress, extrusion temperatures, and compositions of some common ferrous alloys .....  | 11 |
| 3.2 | Chemistry in weight percent of the steels obtained via arc-spark spectroscopy .....  | 13 |
| 4.1 | Billet geometry identification .....   | 25 |
| 4.2 | Ratio of core to sleeve thickness from the steady state region after extrusion. ....   | 35 |
| 4.3 | Billet geometry identification for Case 2.....   | 36 |
| 4.4 | Billet geometry identification for eccentricity measurements .....   | 47 |
| 4.5 | Percentage of the absolute maximum error in wall thickness from nominal for<br>extrudates, along with location and average error and deviation for the entire tube ..... | 49 |
| 4.6 | Chemical analysis in weight percent of the steels used for this project using the arc-<br>spark spectroscopy method .....  | 54 |
| 4.7 | Extrudate sample information for the geometry of the initial billet.....   | 55 |
| 4.8 | Cr and Ni equivalent values for stock materials .....  | 76 |



## Abbreviations and Acronyms

|      |                                    |
|------|------------------------------------|
| bcc  | body-centered cubic                |
| CCT  | continuous cooling transformation  |
| EBSD | electron backscatter diffraction   |
| EDS  | electron-dispersive spectrum       |
| EMPA | electron microprobe analysis       |
| EIO  | Energy Industries of Ohio          |
| FEM  | finite element modeling            |
| HAZ  | heat-affected zone                 |
| ID   | inner diameter                     |
| IMF  | Institute for Metal Forming        |
| OD   | outer diameter                     |
| ORNL | Oak Ridge National Laboratory      |
| SEM  | scanning electron microscopy       |
| TMAZ | thermomechanically affected zone   |
| TT   | time-temperature                   |
| WDS  | wavelength-dispersive spectroscopy |





# 1. Executive Summary

## 1.1 Purpose

The objective of the project described here was to develop design tools that will allow for the selection of compatible metals for co-extrusion of bimetallic tubes. A combination of two metals was selected based on their service properties (e.g., corrosion resistance, elevated temperature performance, strength, ductility, and surface finish).

Bimetallic tubes are used for very specific applications where one of the two metals provides strength and the other provides specific properties such as aqueous corrosion and carburization, coking resistance, and special electrical and thermal properties. Bimetallic tubes have applications in the pulp and paper industry for heat-recovery boilers, in the chemical industry for ethylene production, and in the petrochemical industry for deep oil well explorations. Although bimetallic tubes have major applications in energy-intensive industry, they often are not used because of their cost and manufacturing sources in the United States. This project was intended to address both of these issues.

## 1.2 Research

This research project was led by the Institute for Metal Forming (IMF) at Lehigh University. The other research partner was Oak Ridge National Laboratory (ORNL). The industrial partners on this project were Special Metals Corporation, Dynamet Technology, and Altair Engineering, Inc., who provided technical assistance to the project. Energy Industries of Ohio also participated in the project because its constituency could greatly benefit from the outcome of this work.

IMF conducted both numerical and physical simulations of deformation processing and analyzed the interface integrity of the extruded bimetallic tubes. All of the billet preparation and extrusion of bimetallic bars and tubes were carried out using the 1250-ton extrusion press at ORNL.

The project goals were achieved by investigating the fundamentals of metal flow during co-extrusion of bimetallic tubes. The task was complicated by three factors: (1) the complex geometry of the final product, (2) the different physical and mechanical properties of the two materials, and (3) the complicated mechanics of the co-extrusion process. The project used an engineering science approach that resulted in the development of a co-extrusion model for the production of bimetallic tubes.

The research focused on a physical and numerical analysis of the extrusion process. A multitool approach was used to simulate the extrusion process for bimetallic tubes. The numerical model used was the finite-element modeling (FEM) code DEFORM-2D™, which described the material flow during extrusion. The FEM simulations were also used to predict the state variables of strain and strain rate that are used to model the bonding and interface development that occurs between the alloys during the co-extrusion process.

The results of multitool approach were validated by preparing bimetallic billets of 1020 carbon steel for the outside of the tubes and 304 stainless steel as the core. The 1020 validation was performed on two types of billets:

- **the traditional design**, where core and outside are the same length and
- **a new design**, where the length of the core is reduced by 8 to 20%.

The geometrical results from the FEM simulations were validated on experimental extrusions by measuring the thickness of the inside tube as a function of distance. There was good agreement for all conditions tested. In addition to wall thickness, measurements were also made for the wall thickness eccentricity, and no adverse effects were noted from the new billet design using core shortening.

The FEM simulation of the state variables was validated by detailed investigation of the microstructure at and on either side of the interface of the co-extruded tubes. The simulation and microstructural analysis indicated that most of the carbide precipitation in 304 stainless steel and decarburization of the carbon steel occurs after extrusion during cooldown to room temperature.

### **1.3 Results**

The most important result from this project was the successful use of FEM simulation (using the DEFORM code) to predict the geometrical changes that take place during the extrusion of bimetallic billets into tubing. The FEM simulation was also successful in simulating the state variables of strain and strain rate at the interface of co-extruded tubes. The prediction of state variables was useful in predicting the microstructure that develops at the interface of co-extruded tubing.

A new billet design with 8–20% reduced core length was developed to produce bimetallic tubes with improved uniformity of inside wall thickness and with minimum eccentricity as a function of tube length.

The reduced scrap along with the improved quality of the bimetallic tubes will result in significant energy savings.

### **1.4 Conclusions**

- Use of the simulation based on FEM code DEFORM-2D was successful in predicting the geometrical changes of wall thickness as a function of tube length. On the basis of the validated simulation method, a new billet design based on core shortening was developed. This design provides a significant reduction in scrap produced as compared with the traditional billet design.
- The FEM simulation of the state variables of strain and strain rate was successful in predicting microstructure development at the bimetallic tube interface.
- The reduction in scrap of the bimetallic tube, based on multiple simulation tools when applied to commercial production of bimetallic tube, has a potential for significant savings in energy.
- The project team from Lehigh University and ORNL was very successful in carrying out this project because of the unique characterization facilities at Lehigh and the unique hot-extrusion press facility at ORNL.
- The project topic was carried out as a Ph.D. dissertation. The training gained through this project has led the student to accept a job at Carpenter Technology Corporation in Reading, Pennsylvania.
- The project provided an opportunity for a postdoctoral fellow to gain experience in the simulation of extrusion of bimetallic billets. This postdoctoral fellow is now employed in the aluminum industry.

## **1.5 Accomplishments**

This project designed and successfully implemented a multitool approach to simulate the co-extrusion process. Numerical modeling was used to simulate the extrusion process and to understand metal flow during the co-extrusion process as well as to understand the influence of a new billet design involving a shortened core. The FEM simulations were also used to determine state variables (strain and strain rate) that are used to physically model the bonding and interface development that occurs between different alloys during the co-extrusion process. This cross-disciplinary approach provides geometrical and physical metallurgy results that provide understanding of the co-extrusion process as well as insight in designing the billet and processing steps.

## **1.6 Commercialization**

This project did not include a formal commercialization effort. However, the papers presented at technical meetings and the Department of Energy's description of this project on the Internet have led to interest in this project by bimetallic tubing producers. One of these producers is Farmer's Marine Copper Works, whose staff contacted us (see letter in Appendix) about the outcome of our project on August 26, 2005. The information generated from this project could be critical in meeting the requirements of this company's customers for bimetallic copper and steel systems. Our plans are to meet with staff at Farmer's Marine Copper Works and further explore how best the outcome from this project can be utilized.

There have also been strong expressions of interest from Plymouth Extruded Shapes regarding this project. ORNL staff has visited the Plymouth facility, and staff from this company have made a few trips to Lehigh University.

It is anticipated that commercial interest in the results of this work will increase further as additional presentations are made at technical meetings and as students graduated with Ph.D. degrees from the project start to disseminate the findings of this project among various companies.

One of the barriers to the commercialization of this project could be access to the DEFORM-2D software at companies and availability of dedicated staff to run this type of software. However, project team members intend to continue to run simulation trials for companies using the software available at Lehigh University.



## 2. Introduction

The purpose of the research described in this report was to model the co-extrusion process for forming bimetallic tubes, including the effect of a new billet design, on the geometry and eccentricity of the extruded product using numerical modeling procedures and microstructural development with physical modeling procedures. Co-extrusion is the process of concurrently extruding two or more materials from a single, composite billet. The extrudate is a composite structure of laminate layers that are metallurgically bonded under the pressures and temperatures of the extrusion process. Although it is possible to cold-extrude certain materials, this research focuses on the hot extrusion of ferrous-based alloys.

The market for co-extruded tubes is large and includes applications in the petrochemical, chemical, pulp and paper, and power-generation industries. The use of composites is economically beneficial when the material cost associated with a mono-material component is high and when process efficiency is reduced by excessive corrosion (coking for ethylene production) and process downtime. For example, bimetallic tubes for ethylene production require an inner tube made of a noncoking material. The use of a noncoking inner tube in this application would result in an energy saving of 19 trillion Btu/year and an associated energy cost savings of \$173 million.

In addition to the current challenges associated with the extrusion process, several additional ones are associated with multimaterial extrusion. A concurrent flow of the billet materials needs to be controlled. Often, the material that is the “core” will extrude prior to the “sleeve,” causing a balloon defect at the front of the extrudate. This volume of material is unavailable for the back end of the extrudate, leading to the “pinch-off” defect (a lack of core material at the back). These two defects can be significant, generate a large amount of scrap material, and lower the efficiency of the process.

The development of the bond between the component materials is important to the physical and mechanical properties of the extrudate. Due to the difference in material chemistry as well as the temperature associated with the process, a diffusion of critical elements occurs between the materials. This diffusion layer is termed the thermomechanically affected zone (TMAZ) and is similar to the heat-affected zone (HAZ) in traditional fusion welding with a few distinct differences. Since no liquid phases are present, traditional solidification structures and defects are not present. The formation of intermetallics and other solidification products does not occur; however, solid state metallurgical transformations do occur. Depending on the alloys and the chemical species of the materials, many different deleterious structures may develop. It is of critical importance to understand and control the processing variables (such as time, temperature, strain) that affect these transformations.

Plain carbon steel 1020 and stainless steel 304 were investigated in this research. These alloys were chosen because of their industrial importance as well as their flow stress compatibility; however, the investigation of these two materials serves only a model for investigation of the influence of initial billet geometry on extrudate geometry as well as of the feasibility of both numerical and physical modeling of the process. There is no intended application for this particular materials system and extrudate geometry.

Two different approaches and tools were used to model numerous aspects of the co-extrusion process: numerical and physical modeling. Both modeling approaches were verified using experiments with industrially produced extrusions. Comparison between the modeling efforts and the industrial results shows that the results are similar and that it is feasible to model the process.

Numerical modeling was used to investigate the influence of initial billet geometry as well as the effect of various processing parameters on the final extrudate geometry and eccentricity. A commercial finite element modeling (FEM) package, DEFORM-2D™, was used to perform a series of simulations. Variables investigated included various core and sleeve thicknesses in the initial billet, different extrusion ratios, and a new billet design. For each experiment with the core/sleeve thickness ratio, three billet designs were modeled. The new billet geometry varied the length of the core material: full length, 90% of the overall sleeve billet length, and 80% of the sleeve billet length. By reducing the core length in the billet, concurrent material flow is promoted during early stage extrusion (prior to steady state). State variables corresponding to regions at interface between the materials during extrusion were calculated using the FEM software. These values of strain and strain rate were used to simulate the metallurgical development with a thermomechanical simulator.

Thermomechanical simulation was performed using cylindrical samples of the co-extruded alloys. A Gleeble unit was used to deform the materials using the state variables from the FEM simulations. Accurate temperature control was achieved via resistive heating. Although the state of stress and deformation conditions in an upsetting test is somewhat different from what is experienced during extrusion, this method allowed for a simple laboratory simulation that included a significant amount of deformation at process temperature, strain, and strain rate. Other research performed on physical simulation of the bond has used hot isostatic pressing, but this approach does not significantly deform the materials and also produces lower strain rates than can be achieved using the Gleeble system.

A series of industrial extrusions were performed so that the results of the modeling could be verified. By utilizing both tools, the co-extrusion process can be simulated and optimized without a large matrix of industrial experiments. Assembly of a composite billet is laborious and can be costly due to the materials and press-down time associated with experimentation production delays. Simulation of the co-extrusion process allows for process and product design at a lower cost and a faster pace than traditional experimentation.

## 3. Background

### 3.1 Extrusion Process

The process of metal extrusion involves forcing a block of material, usually cylindrical, through a fixed die in order to reduce its cross sectional area and provide a functional shape. The undeformed material is referred to as the “billet” while the deformed material is referred to as the “extrudate.” The resultant shape of the extrudate is dependant on the shape of the die orifice through which the material is forced. Details of the extrusion process are available in Laue and Stenger’s *Extrusion*.<sup>1</sup>

The benefits of extrusion include the ability to produce products with large and complex cross sections or many products from a single billet in an economical and high-productivity process. Die design can be either simple, for axi-symmetric extrusion of pieces such as rod and tube, or complex for non-axi-symmetric extrudates. As die complexity increases, so does material flow from the billet through the die. The material flow through a complex-shaped die increases in complexity because of non-uniform material flow and significant increase in friction at the material/die interface. Due to the scientific and engineering focus of this work, the simple axi-symmetric extrusion of a tube was investigated. This allowed for the optimization of the process by minimizing the number of processing variables.

To extrude geometries with hollow cross sections, such as tubes, several different approaches may be taken. The starting billet may have a hollow cross section, as is the case in this research. The hole may be machined/gun-drilled prior to its being loaded into the press, or the hole may be produced using an operation known as “piercing.” In piercing, a broach is forced through the preheated billet leaving a hole.

Extrusion is performed using a mandrel, which is a solid rod that is inserted in the hole. The mandrel helps to maintain the hollow cross section and prevents it from collapsing during deformation. The mandrel may be attached to the dummy block, known as a moving mandrel. Static mandrels may also be used, as in the case where complicated internal geometries are desired and a double-action extrusion press is available.<sup>1</sup> The second approach to extrusion of a hollow cross section can also involve a special porthole die.<sup>1</sup> The material is forced into separate material streams over a bridge or spider in the die. The material is then forced back together in the welding chamber portion of the die where it diffusionally bonds together from the elevated temperature and pressure imposed by the weld chamber geometry. The resultant weld is known as a longitudinal weld and runs the length of the extrudate. Aluminum alloys are very often produced using this method because of their excellent extrudability and flow properties. Ferrous products are generally extruded using a moving mandrel because of their significantly high flow stress.

In extrusion, the reduction in cross sectional area is known as the extrusion ratio, which is the ratio of cross-sectional area of the upset extrusion billet to that of the extruded product (Eq. 1).

$$R = \frac{A_0}{A_1} \quad (1)$$

where

- R = extrusion ratio,
- $A_0$  = cross-sectional area of the upset billet, and
- $A_1$  = cross-sectional area of the extrudate.

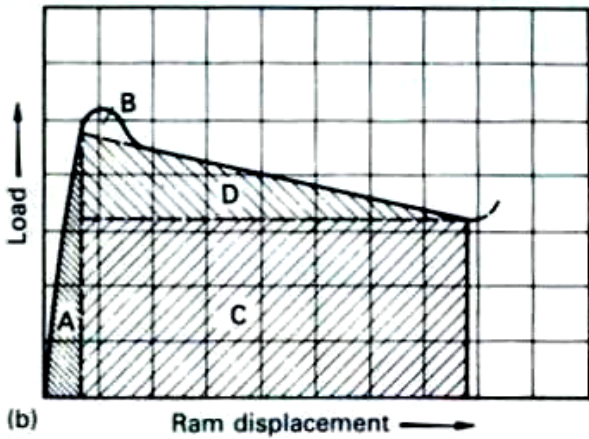
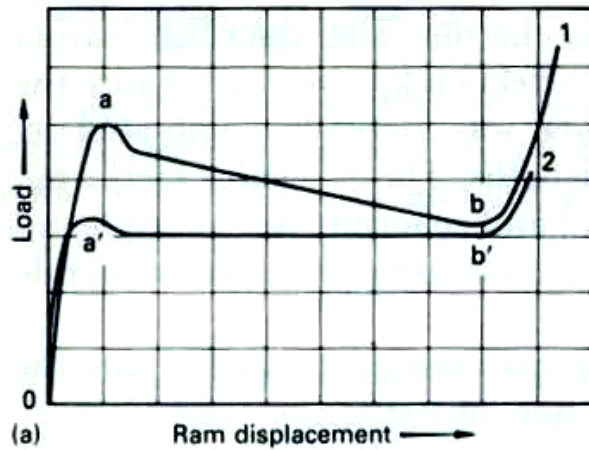
The amount of deformation in the process is proportional to the extrusion ratio. The initial billet cross-sectional area,  $A_i$ , refers the billet prior to any deformation. During upsetting (prior to extrusion), the billet expands to fill the extrusion chamber, shortening in length and increasing in cross-sectional area. Higher values of R can be obtained successfully with materials that exhibit lower flow stress (or by reducing flow stress caused by increased temperature), up to the point where extrusion defects occur. High-temperature defects include “hot shortness” where localized surface melting or cracking occurs, which results in surface tearing, galling, or die pickup that occurs when the lubricant breaks down. Low temperature/high strain rate/flow stress failures include chevron cracking, in which a series of v-shaped cracks appear in the center of the extrudate. Typical extrusion ratios for aluminum are above 40, and for steel typical values are lower than 40. Both material families are generally extruded at elevated temperatures.

Typical load versus stroke behavior during extrusion (both indirect and direct) can be observed in Fig. 3.1(a). In Fig. 3.1(b) the individual components of the overall work to extrude a material in direct extrusion are noted. Section A describes the work (force x ram displacement) needed to upset the material to fill the extrusion chamber. The amount of work needed is influenced by both the diameter of the billet and the chamber as well as the flow stress of the material at the upsetting temperature. Area B describes the work needed to initiate extrusion, also referred to as “break through,” with the maximum load defined as the break-through force (or pressure). It is the least understood component due to the complex flow of material during the initial, non-steady state flow conditions of extrusion.<sup>1</sup> Region C is the work associated with material deformation and is directly influenced by the flow stress of the material at the extrusion temperature. The final area, D, represents the work associated with friction in the process. Generally, this region decreases in magnitude as extrusion progresses due to the decrease in surface contact of the billet with the press chamber. This region is influenced by the type and amount of lubricant on the billet during extrusion as well as the lubricant’s stability.

Friction plays an extremely important role in extrusion. As shown in Fig. 3.1(b), region D, it can play a significant role in extrusion force. Lubricants are used in order to reduce the friction during extrusion. This is important not only to lower the extrusion force that is necessary, but it also to reduce the wear on the tooling (extrusion chamber, mandrel, and extrusion die) as well as to minimize any surface temperature increase associated with frictional heating during deformation that may result in surface-defect generation. Additional roles of lubricants during deformation include thermal shielding of the heated billet from temperature loss to tooling (especially the extrusion chamber) as well as acting to prevent or minimize oxidation of the billet due to the high temperatures associated with the preheat. The lubricant that is used should not react chemically with the work piece.

One defect associated with the extrusion of hollow cross sections or multi-material extrudates is eccentricity. Eccentricity is defined differently for each of the two cases. Figure 3.2 shows examples of some of the different types of eccentricity that may develop during the extrusion of tubes or bimetallic tubes. As expected, there are more definitions of eccentricity for the bimetallic tubes due to the additional variables (core location and thickness). In general, there are two types of eccentricity: the location of the center hole and the shape of the center hole. For the bimetallic tubes, the additional types of eccentricity are the location and shape of the core layer. The different types of eccentricity may be present alone or in combination with other types. Eccentricity is affected by many different factors. One major cause is the localized temperature loss of the billet while sitting in the extrusion





- (a) Dependence of the extrusion load on the ram displacement:  
 $a-b$  = Direct extrusion  
 $a'-b'$  = Indirect extrusion
- (b) Division of the work of deformation  
**A** = Work of upsetting  
**B** = Work needed to initiate deformation  
**C** = Work of deformation  
**D** = Work to overcome friction and shearing in direct extrusion

Fig. 3.1. Schematic load versus ram displacement curves for extrusion shows: (a) the difference between direct and indirect extrusion and (b) division of the work of deformation of the direct extrusion process (Source: Laue, K., and Stenger, H. *Extrusion*, Metals Park, American Society for Metals, 1981).

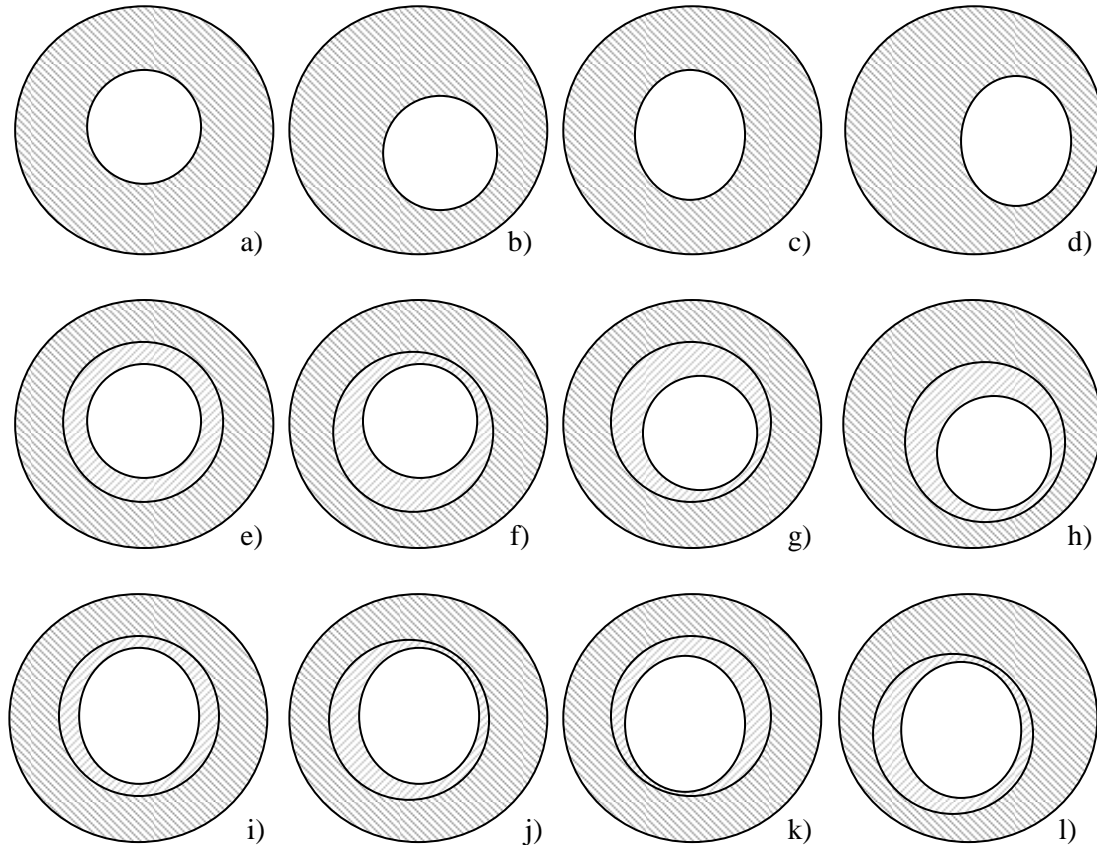


**Fig. 3.2. Eccentricity definitions for tubes (a–d) and bimetallic tubes (e–l).** (a) tube with no eccentricity, (b) off-center hole in tube, (c) oval center hole in tube, (d) oval off-center hole in tube, (e) bimetallic tube with no eccentricity, (f) core material off center in bimetallic tube, (g) off-center hole in bimetallic tube, (h) off-center hole and core in bimetallic tube, (i) oval center hole in bimetallic tube, (j) oval center hole and off-center core in bimetallic tube, (k) oval off-center hole in bimetallic tube, and (l) oval off-center hole as well as core material off-center in bimetallic tube.

container prior to extrusion. In order to maintain structural integrity and minimize tooling wear, the extrusion chamber is usually at a lower temperature than the billet to be extruded. The container temperature is based on the material to be extruded and its thermal characteristics, including thermal conductivity and heat capacity. As the billet sits in the chamber, the bottom portion of the billet is in contact with the chamber allowing for heat flow from the higher temperature material into the lower temperature chamber. As the material locally cools, the flow stress in that region increases; thus, the material flow during extrusion becomes heterogeneous giving rise to eccentricity. Similarly, heat flow from the inner diameter (ID) of the billet to the mandrel may cause changes in material flow and result in eccentricity.

Gravity plays a role in the development of eccentricity as well; since the center hole in the billet must be larger than the mandrel for it to be inserted, uneven flow may occur in the center of the billet during initial upsetting. This is caused by the billet settling in the chamber causing the mandrel to be off center in the billet center hole.

### 3.1.1 Steel Extrusion

For each material system that is extruded, specific needs and methods are associated with the process. This section deals specifically with processing variables associated with ferrous material extrusion.

In general, the flow stress of ferrous materials requires high extrusion temperatures between 1000 and 1300°C, Table 3.1, for successful extrusion. It can be observed that there is not a great difference in mean flow stress between carbon steel (i.e., 1020 plain carbon steel) and stainless steel [corrosion-resistant steel (i.e., 304 stainless steel)] at the common extrusion temperatures.

**Table 3.1. Flow stress, extrusion temperatures, and compositions of some common ferrous alloys<sup>a</sup>**

| Alloy   | Extrusion temperature (°) | Mean flow stress (MPa) |
|---|---------------------------|------------------------|
| Carbon steels (0.1–1 C)                                 | 1200 ± 100                | 150                    |
| Low-alloy steels (0.2–0.6 C, Cr, Ni, Mo)                | 1200 ± 70                 | 130                    |
| Corrosion-resistant steels                              |                           |                        |
| (<0.15 C, 11.5–13 Cr)                                   | 1175 ± 25                 | 180                    |
| (<0.15 C, 11.5–13 Cr)                                   | 1175 ± 25                 | 190                    |
| (0.03–0.1 C, 18–20 Cr, 8–12 Ni)                         | 1180 ± 30                 | 200                    |
| (<0.08 C, 17–19 Cr, 9–12 Ni)                            | 1180 ± 30                 | 230                    |
| (<0.25 C, 24–26 Cr, 10–12 Ni)                           | 1170 ± 30                 | 240                    |
| (0.03–0.08 C, 16–18 Cr, 10–14 Ni)                       | 1160 ± 20                 | 250                    |
| High-speed steels (2 C, 12 Cr, 0.9 V)                   | 1140 ± 80                 | 300                    |
| Spheroidal cast iron (3.1–3.5 Cr, 2.4–3 Si, 1.1–1.8 Ni) | 1050 ± 25                 | 200                    |

<sup>a</sup>Source: Laue, K., and Stenger, H. *Extrusion*, Metals Park, American Society for Metals, 1981.

Microstructural phase changes associated with temperature are important in controlling material flow stress as well as ductility.<sup>1</sup> At lower temperatures, plain carbon steel (1020 as investigated in this research) alloys are primarily  $\alpha$ -ferrite plus some cementite ( $\text{Fe}_3\text{C}$ ), as denoted in the equilibrium binary Fe-C phase diagram shown in Fig.3.3.

Lamellar structures composed of alpha-ferrite and cementite are referred to pearlite, which is a common phase combination in carbon steels at room temperature. Material of this phase exhibits higher flow stress as well as reduced ductility when compared to the higher temperature  $\gamma$ -austenite phase (Fig. 3.3). At even higher temperatures, the material once again goes through a phase change to  $\delta$ -ferrite (Fig. 3.3) where ductility begins to decrease. For optimal extrudability, a homogenous  $\gamma$ -austenitic microstructure lacking large grain boundary precipitates is desired in plain carbon steel alloys.

Austenitic stainless steels, such as the 304 stainless steel investigated in this research, exhibit primarily the  $\gamma$ -austenite phase at room temperature due to the addition of alloying elements such as Ni and Mn. Although the structure is primarily austenitic at room temperature, the material still exhibits a very high flow stress, and high temperatures are required for successful extrusion. Typically, extrusion temperatures for stainless steels fall into the upper end of the 1000–1300°C temperature range. Figure 3.4 shows a vertical section of the ternary phase diagram for the Fe-Ni-Cr system at 70%Fe.

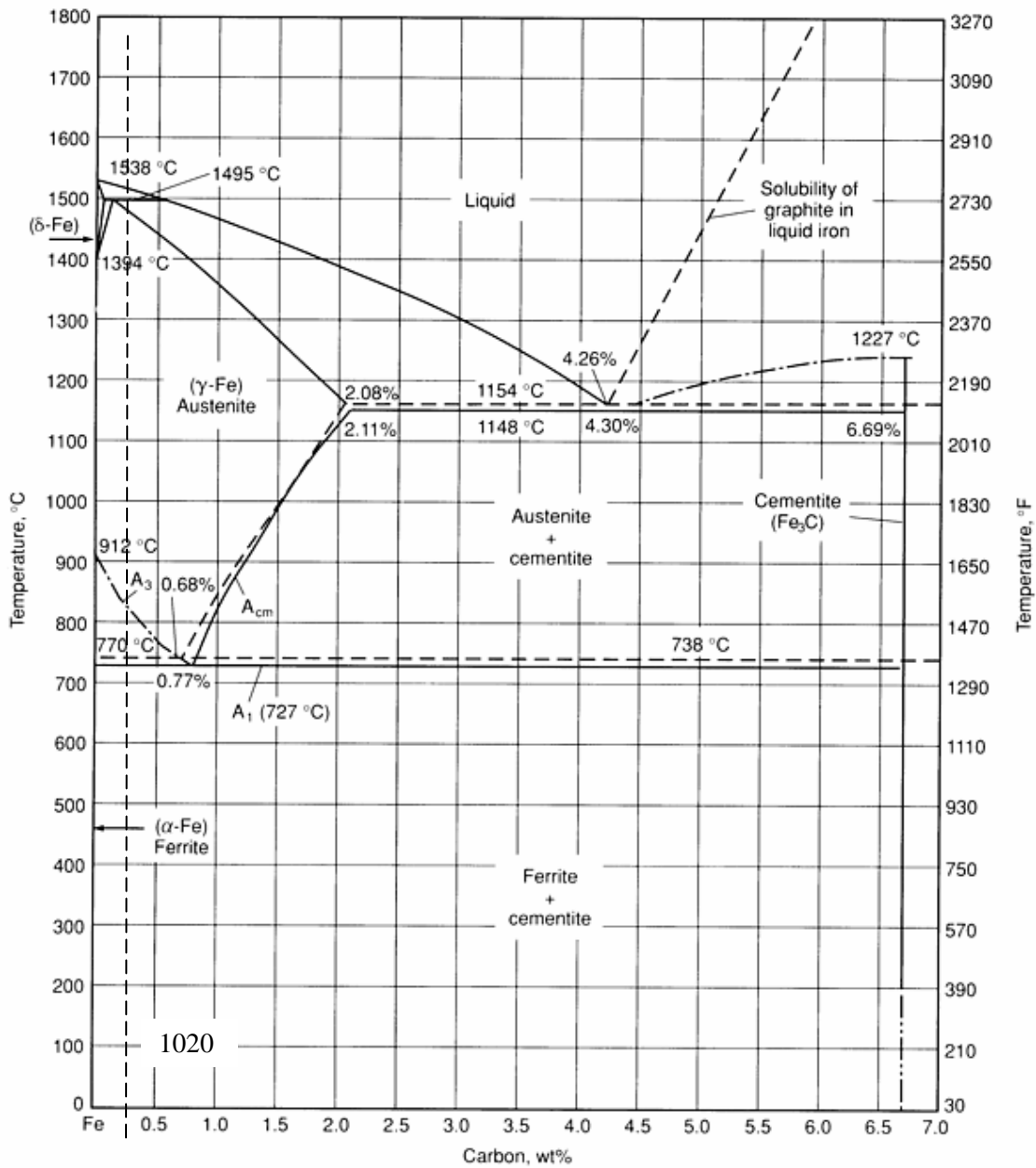


Fig. 3.3. Fe-C equilibrium phase diagram.

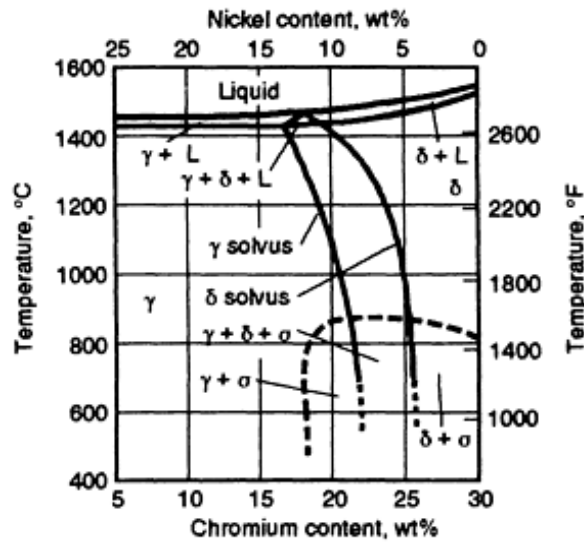


Fig. 3.4. Vertical section of Fe-Ni-Cr ternary phase diagram at 70% Fe.

The Cr content of the 304 stainless steel is approximately 18% (Table 3.2), which at the extrusion temperatures of 1100–1200°C is fully austenitic is located in the phase field that is continuous to room temperature.

Table 3.2. Chemistry in weight percent of the steels obtained via arc-spark spectroscopy

| Alloy | C    | Cr    | Mn   | Ni   | P     | S     | Si   | Fe      |
|-------|------|-------|------|------|-------|-------|------|---------|
| 1020  | 0.19 | -     | 0.71 | -    | 0.009 | 0.050 | -    | Balance |
| 304   | 0.02 | 18.27 | 1.13 | 9.32 | 0.028 | 0.025 | 0.41 | Balance |

Because of the strong influence of temperature on microstructure and thus on the extrudability of ferrous materials, great care must be taken in temperature management during extrusion. If the preheat temperature is too high, temperature increases due to frictional and deformation heating may result in a heterogeneous microstructure consisting of both  $\gamma$ -austenite and  $\delta$ -ferrite that may lead to hot shortness or localized material tearing. Low preheat temperatures or excessive heat loss to tooling prior to extrusion, on the other hand, will lead to the formation of  $\alpha$ -ferrite and the associated decrease in ductility and increase in flow stress leading to nonuniform material flow as well as extrusion defect formation. As flow stress increases, tooling life decreases rapidly; however, excessive tooling temperature also reduces tooling life.

Lubricants commonly employed in non-ferrous material extrusion for the most part are unsuitable for ferrous material extrusion. The high temperatures and extrusion pressures associated with steel extrusion cause most conventional extrusion lubricants to break down or fail. Two common methods exist for steel lubrication. The first is a thin film of highly viscous molten glass. The glass softens at temperatures below the steel extrusion temperature and is often applied in a powdered form that rapidly melts to become a surface film that acts to insulate the billet. Another suitable lubricant for high-temperature ferrous extrusion is a suspension of graphite in liquid that evaporates when applied to the hot billet. This type of lubricant was used in this research (Necrolene). The paste is applied to the billet and begins to vaporize, leaving behind a graphite film that acts as the lubricant during extrusion.

Due to the relatively high flow stress of ferrous materials as well as the difficulty associated with lubrication, practical values for the extrusion ratio,  $R$ , fall within the range of 10 to 100. In reality, the upper limit is usually set between 20 and 25. Maximum extrudate length is generally between 15 and 25 m due to the breakdown of the lubricant.<sup>1</sup> Extremely complex shapes such as those extruded for aluminum are not common, thus steel extrusion is generally limited to fairly symmetric cross sections.

### **Co-extrusion**

Co-extrusion is an extrusion process where the initial billet is composed of more than one specific material. Other terms used to describe the process are bimetallic or multi-metallic extrusion, concurrent extrusion, extrusion bonding, solid state welding extrusion, and composite extrusion. Multi-material extrusions may include two solid layers surrounding a layer of difficult-to-deform powder. After hot extrusion, the powder forms a solid, sintered intermediate layer. At times, the term “co-extrusion” is used to describe a situation where a coating is applied to a rod that is being extruded or drawn, such as the case of placing insulation on a conductive wire; however, for this document, this definition is not used. For this research, a longitudinal arrangement of layers in the billet/extrudate will be investigated, which results in a laminated product.

Two different alloys of the same material system or two radically different materials (e.g., Cu and Ti) may be used to form a final, sound, composite product. Production of composites in this manner maximizes the benefits of the individual component materials. Often, one alloy or material is selected because of a specific property, such as corrosion resistance or electrical conductivity. This is then paired with another material that may be either lower density or less expensive, or has other desirable properties for the final product. The first alloy may be in the form of a cladding in the final product, with the additional material present to provide support and strength. The extrusion process provides an economical method for producing long length products, including tubes, rods, and ribbed structures.<sup>2</sup> One of the major benefits of using extrusion to produce composite parts is that there is no need for any additional joining/bonding process to manufacture the final part. As the materials are deformed into a net or near net shape, they are concurrently metallurgically bonded. This eliminates the need for processes such as fusion welding (both overlays and joining) or mechanical joining (through the use of fasteners or adhesives); however, the process is limited to geometries that can be extruded.

Extruding bimetals presents problems that are not encountered when extruding a single material. Dimensional tolerances between the two materials become an important consideration, along with the strength of the bond, and the potential for greater amounts of scrap. The continuity of the bond is an important consideration for both strength and physical properties (corrosion resistance, thermal conductivity, etc.). The presence of porosity at any level negatively affects the performance of the final product. Both rolling and drawing are other metal-forming processes that are commonly used to produce mass amounts of bimetallic products, such as wire or sheet and plate, as well as other simple geometries that result from shape rolling.

Growth of applications utilizing bimetallic extruded products inspired many theoretical and experimental works that have been performed in recent years to understand the bond development of bimetallic extrudates.<sup>3,4,5,6,7,8,9,10,11,12,13,14,15,16,17,18,19,20</sup> Additional resources regarding “solid-state welding” show investigations into the microstructural development and mechanical testing.<sup>16,17,19,20</sup> Properly designed bimetallic products exhibit an optimal combination of desired properties while minimizing their restrictive properties. Many factors controlling bimetallic rod and wire manufacturing processes were established and optimized. The often cited work of Avitzur<sup>9</sup> summarizes the factors that influence the extrudability of a composite rod, and are as follows:

1. Extrusion ratio (R) or percentage of area reduction
2. Semi-cone angle of the die,  $\alpha$
3. Length of the land or bearing in the die ( $L$ )
4. Friction between the billet and the container ( $m$ )
5. Ratio of the diameter of the core to the billet (or sleeve diameter) ( $D_c/D_0$ )
6. Ratio of the core and sleeve flow stresses ( $\sigma_c/\sigma_s$ )
7. Presence of front tension
8. The interfacial bond strength between the sleeve and core, or the friction between the two materials ( $m_i$ )

It is not only the mechanical properties of the materials making up the billet that have an effect, but also a combination of geometric and process parameters. As shown by Sliwa,<sup>8</sup> the geometrical parameters affect the plastic deformation and flow of the material more significantly than the various properties of the materials. In general, low, semi-die angles,  $\alpha$ , encourage sound flow.<sup>9,21</sup> Sleeve fracture may be minimized by using either low or high die angles where intermediate die angles may promote fracture.<sup>9</sup> The effect of the extrusion ratio on the extrudability of a composite material is generally coupled with the ratio of the core-to-billet diameter. Low core-to-billet diameter ratios decrease the occurrence of core fracture,<sup>9</sup> while increasing R negatively affects uniform deformation of the core and sleeve.<sup>21</sup> As core diameter decreases, the effect of R is less severe, and successful extrusion can be carried out at relatively high R values.<sup>22</sup>

One of the strongest influences on concurrent flow and failure of the extruded material is the interfacial friction  $m_i$  or interface bond strength. As has been shown in the work by Avitzur<sup>9</sup> as well as others,<sup>23</sup> the higher the friction between the materials/bond strength, the lower the occurrence of core failure. Zoerner et al.<sup>23</sup> have shown that when the interface between the core and the sleeve is lubricated, no successful extrusion conditions were found in hard core/soft sleeve-clad systems. When the bond strength is low and a soft sleeve material is used, the sleeve is unable to transfer force to the hard core material, preventing concurrent extrusion.

Studies<sup>2,4,9,21,22,24</sup> have shown that the ratio of flow stress between the two materials at the extrusion temperature must be below two for successful extrusion. The most uniform flow (neglecting friction as well as die geometry) occurs when the ratio approaches unity. An increase in the ratio of only 25 to 50% will decrease the operating window in which successful extrusion may occur.<sup>2,4,9,22,24</sup> When the ratio becomes higher, extremely nonuniform flow occurs, and the material does not concurrently extrude or bond together.

Figure 3.5 is a schematic representation of a flow net located at the center of a billet during extrusion. The schematic labeled “S” shows a billet exhibiting uniform flow during extrusion. As can be observed, the flow net is undistorted at the top of the billet (the unextruded portion farthest away from the die face) and maintains equal grid spacing. The only distortion of the grid occurs near the die orifice, where a zone of shear flow develops (noted by the highly distorted grid). This shear zone marks the interface between fast- and slow-flowing materials. The height of the shear zone, or the highly distorted grid pattern, is inversely proportional to the uniformity of the flow (i.e., a low shear zone height corresponds to uniform flow conditions). These conditions are generally met when the frictional force between the billet and both the die face and the container are very low. Additionally, when a hollow cross section extrudate is produced using a mandrel, the interfacial friction between the core and mandrel ( $m_m$ ) must be low so as not to restrict the flow of the core. Figure 3.5A shows less uniform flow, which is observed by the larger shear region (distorted grid) that is associated with high friction between the billet and the die face. When the friction between the billet and both the die face and the container are significant, nonuniform flow occurs, as shown in Fig. 3.5B. Highly nonuniform flow that is shown in Fig. 3.5C occurs when there is a large frictional force between all of

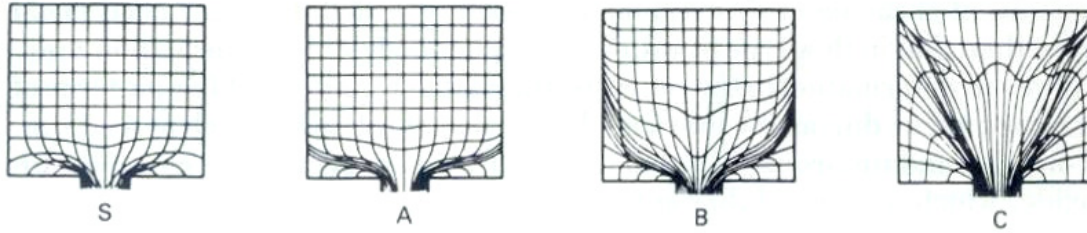


**Fig. 3.5. Schematic representation of the flow of material during direct extrusion through a flat face die.** S—uniform flow with minimal friction between the billet and the container and the die face, A—less uniform flow associated with low billet-container friction but high friction between the billet and die face, B—significant friction between the billet and both the die and the container, and C—very nonuniform flow associated with high friction between the billet and both the die and the container as well as variation in flow stress near the billet surface due to localized decrease in temperature. (Source: Dürschnabel, W., *Metall.* 22 (1968), 476–437.)

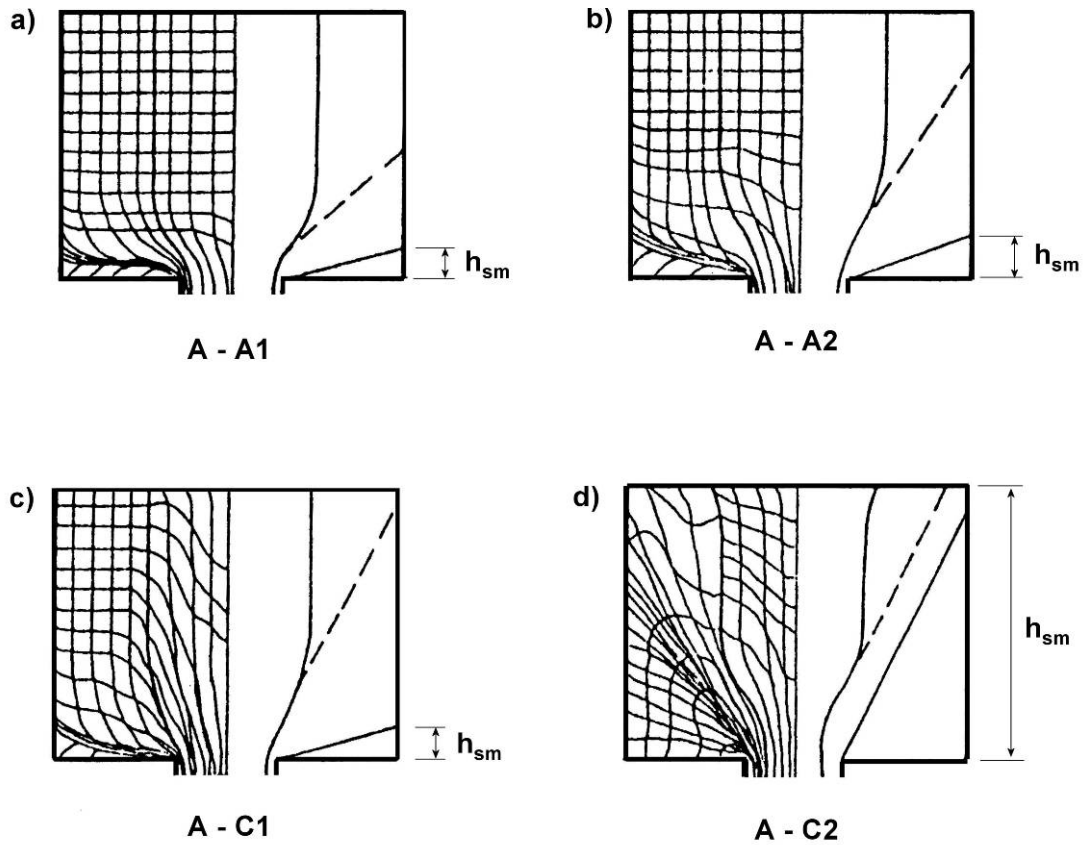
the billet contact areas, as well as an increase in the flow stress of the material at the surface, which is a result of local cooling. As heat is lost to the container prior to and during extrusion, the flow stress of the material increases, which acts to complicate the flow pattern (observe the highly distorted grid elements). This final case is analogous to the type of flow observed in a bimetallic billet extrusion of a solid cross section, where the core material is softer (lower flow stress) and the sleeve material is harder (higher flow stress).

Figure 3.6 shows a series of flow net patterns for the extrusion of a solid rod from a bimetallic billet. Figs. 3.6(a) and 3.6(b) show fairly uniform flow between the two materials while Figs. 3.6(c) and 3.6(d) illustrate the nonuniform flow that is undesirable. In Figs. 3.6(a) and 3.6(b), the height of the shear zone is not very great, and the flow net does not exhibit a discontinuity across the sleeve and core materials. Although the height of the shear zone is not great in Fig. 3.6(c), there is a sharp change in the grid pattern between the sleeve and core material. The samples in Figs. 3.6(a) and 3.6(c) have the core material as the higher flow stress, and Figs. 3.6(b) and 3.6(d) have a soft core material and the higher flow stress material in the sleeve.

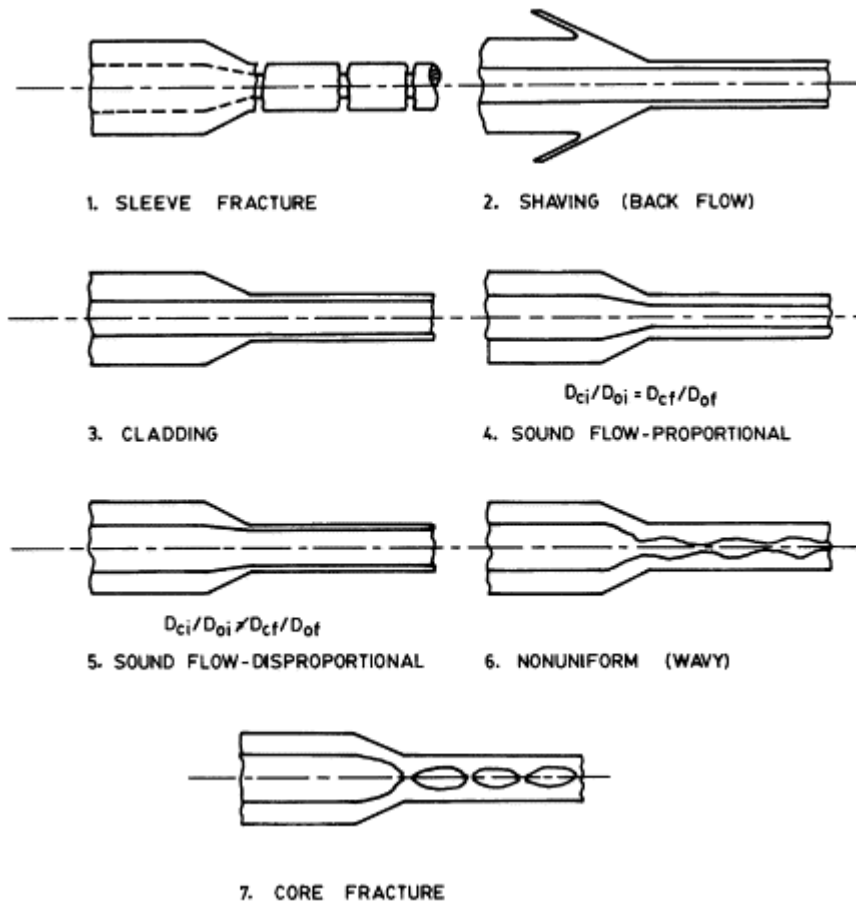
The extrusion experiments performed in the work had the 304 stainless steel material as the core and the 1020 plain carbon steel as the sleeve. This corresponds to a hard-core, soft-sleeve scenario, such as shown in Fig. 3.6(a and c).

Figure 3.7 presents the different types of flow that may occur during bimetallic extrusion, including both sound or desirable flow as well as defects.<sup>4</sup> Sleeve fracture is different than the “palm tree defect,” named for the resemblance to the tropical plant.<sup>24</sup> Sleeve fracture is a result of the shear and tensile stresses experienced by the sleeve material exceeding the tensile strength of the material.<sup>4,24</sup> The palm tree defect occurs in systems with soft sleeve material and hard core material where the sleeve extrudes at a velocity much greater than that of the core and forms overlapping sections.<sup>24</sup> The sleeve material shears at both the tool and core interfaces.<sup>24</sup> Core fracture or pinch off (Fig. 3.7-7) occurs in the case of a hard core material and soft sleeve<sup>4,9,24</sup> and is promoted by large extrusion ratios and intermediate initial core thickness values.<sup>4,25</sup> As shown by Avitzur,<sup>9,25</sup> the harder component in the bimetallic billet is the most likely to fail due to tensile fracture during extrusion. Nonuniform or wavy-core failure (Fig. 3.7-6) is incipient pinch-off or core fracture.<sup>4,22</sup> Shaving, also known as back flow or sleeve ironing, occurs when very low extrusion ratios are used; these are more prevalent with a hard core material and in dies with a large cone angle.<sup>4,22,24</sup> In this case, the core material does not deform, or deforms only slightly, preventing the sleeve material from entering the die orifice. Due to conservation of volume, the sleeve material flows backwards (expedited by its lower flow stress).





**Fig. 3.6. Schematic representation of material flow in a bimetallic billet through a flat face die.** (a, b) similar flow between the two components, (c, d) extremely different types of flow between the components, (a, c) hard core, soft sleeve, (b, d) soft core, hard sleeve. (Source: Sliwa, R., *Journal of Materials Processing Technology* (Netherlands) 67, Issues 1–3 (1997), 29–35.)



**Fig. 3.7. Types of flow behavior observed during the co-extrusion of a rod from a bimetallic billet** (Source: Apperley, M. H., Sorrell, C.C., and Crosky, A., *Journal of Materials Processing Technology* **102**, Issues 1–3, 2000, pp. 193–202).

Since the materials being investigated in this project exhibit good ductility and flow characteristics, the focus is on controlling the distribution of sleeve and core thicknesses in the extrudate, with emphasis on promoting proportionate sound flow (Fig. 3.7).<sup>4</sup> The continuity/soundness of the bond is an important consideration for both strength and physical properties (corrosion resistance, thermal conductivity, etc.).

The above parameters focus on promoting concurrent flow during the steady state regime of extrusion. Often during the initial breakthrough portion as well as the final stage of extrusion, non-concurrent material flow occurs. Figure 3.8 presents the cross section of a co-extruded modeling material rod with hard core and soft sleeve material.

During the initial part of extrusion, an excess of core material extrudes at the front of the extrudate, so-called core “ballooning.” In turn, this leads to a deficiency of core material at the back end of the extrudate, known as core pinch-off. These two regions where the thickness of the core and sleeve are



**Fig. 3.8. Co-extruded rod of modeling material, hard core/soft sleeve, showing the core ballooning at the front of the extrudate (right) and core pinch-off at the back end (left).**

not constant must be discarded as scrap due to the lack of geometrical tolerances. These regions can be very large depending on processing. Understandably, there is a need to minimize the amount of scrap material that is generated during extrusion due to the inherent costs of billet preparation and assembly, as well as the potential financial losses associated with the core material. In addition to cost, the scrap produced from defects discussed above also cause significant energy waste. The energy waste results from a combination of factors, including (1) loss of energy required during billet heating and extrusion process and (2) energy required to replace the wasted material. As stated earlier, it is common to produce composite structures in an effort to minimize the amount of an expensive material in a given product. In the case where there is an expensive alloy as the core material, losses due to premature extrusion are greater and minimize the benefits of composite extrusion.

During steady state material flow, the bond location is constant. Because steady state material flow has been managed by the variables listed above, a new approach has been proposed in the current project to promote an earlier onset of steady state material flow as well as to reduce material that is extruded “out of tolerance” during the initial breakthrough.<sup>14</sup> Figure 3.9 illustrates a conventional and a novel billet design for a bimetallic tube. In the novel design, the core material is recessed (Fig. 3.9) at the nose of the billet. This is to minimize the amount of core material that tends to extrude prematurely (before the sleeve), which results in the ballooning of the core at the front of the extrudate (Fig. 3.8). The findings are presented in the next chapter, Results and Discussion.

Eccentricity in co-extruded materials is similar to that in normal extrusion but complicated by the variance in flow of different materials. Sensitivity to temperature/flow stress gradients is increased due to the potentially greater difference in flow stresses at a constant temperature. A greater number of eccentricity cases exist as a result of the additional variable (location of the bond between the two materials) as shown in Fig. 3.2.

An additional and important consideration in preparing a co-extruded product is the chemical compatibility of the component alloys. Much like fusion welding of dissimilar metals, great

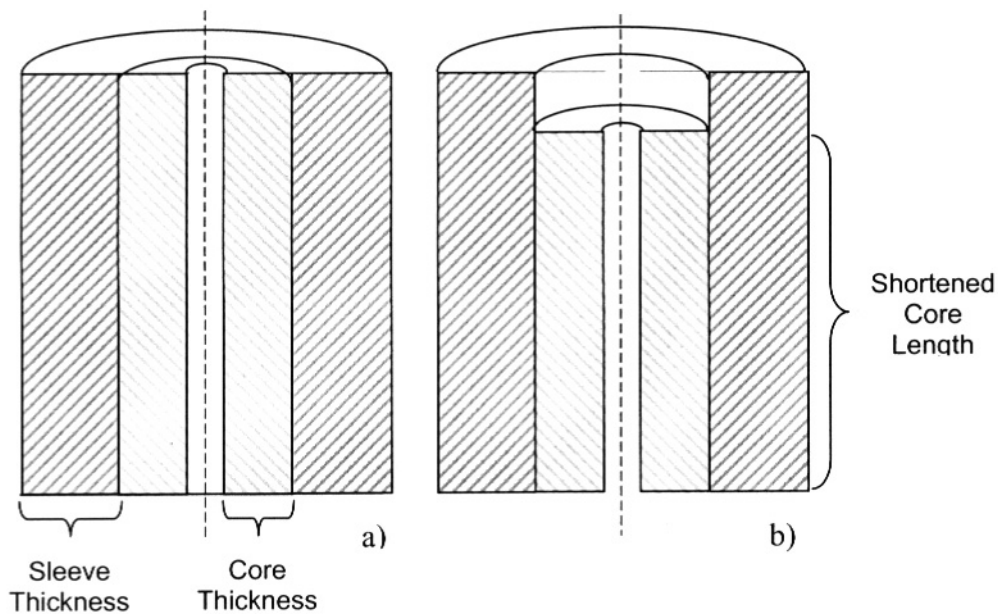


**Fig. 3.9. Schematic cross section of unextruded billet: (a) traditional design and (b) novel design with shortened core.**

consideration must be given to the potential microstructural transformation products that will be a result of the process. Since no melting occurs in co-extrusion, there are no solidification concerns like there are in fusion welding. Diffusional transformations are of concern, and it is important to consider the effects on mechanical, electrical, or thermal properties of the final product.

### 3.1.2 Diffusion and Co-extrusion Bonding: Microstructural Development

Solid-state welding processes are used to join two (or more) work pieces together without heating the materials to their melting temperature or by using an intermediate liquid phase. The most common metals welded by the co-extrusion process include low-carbon and stainless steel, aluminum, aluminum alloys, copper, and copper alloys. Additional applicable materials include nickel, zirconium, titanium, tantalum, niobium, and their alloys.<sup>26</sup> The benefits of using co-extrusion are several-fold and include the ability to have a semi-continuous process to produce large products, the ability to join dissimilar and difficult to join materials, the ability to minimize the formation of undesirable phases (such as brittle intermetallics), and no phase melting during deformation processing. The formation of undesirable phases is often a limitation that is associated with fusion welding because of liquid formation. Additionally, in fusion welding processes, an undesirable cast or solidification microstructure may evolve that requires additional post processing heat treatments to ensure acceptable physical and mechanical properties. Co-extrusion differs from diffusion bonding because pressure and metal flow is used in addition to chemical transport at the interface to join the materials.

The interface between the materials is of the highest importance because it is the most likely region for failure to occur and will exhibit the most complex microstructure. In the case of two materials joined via co-extrusion, failure may occur at the exact interface, or in either of the two materials in the region adjacent to the new bond. However, the failure will be a result of the interaction between the materials and their chemistry, and microstructure that developed as a result of processing. An understanding of the development of the interfaces between materials systems is critical for meeting production needs; however, even for simple systems that form solid solution alloys there is a lack of knowledge of the interface reactions.<sup>26</sup> Much like a HAZ forms in a fusion weld from elevated temperatures, a thermomechanically affected zone (TMAZ) forms during co-extrusion. It encompasses the region of microstructure adjacent to the bond affected by the pressure-temperature history during extrusion.

Solid-state welding processes include friction welding, friction stir welding, impact or explosion welding, forge welding, roll welding, clad welding, friction bonding, and diffusion bonding. Diffusion bonding is the process most similar to the bonding that occurs during co-extrusion. Figure 3.10 illustrates the various stages of diffusion bonding that occur without the application of an external pressure. Initial contact between the two materials is limited to a few asperities, which occurs at room temperature, Figure 3.10(a). During the first stage of bonding, Figure 3.10(b), surface asperities begin to deform from either plastic flow, creep, or a combination of both. In co-extrusion welding, an external force is applied to the bond due to the nature of the geometry of the process as the billet is forced through the extrusion die. As the asperities deform, the interface becomes a discontinuous network of pores. The second stage of diffusion bonding, Figure 3.10(c), begins with grain boundary diffusion of atoms to the voids and grain boundary migration. Pores may shrink as well as become trapped in the interiors of grains as the grain boundaries begin their movement. The third and final stage of bonding involves volume diffusion of atoms to the voids, Figure 3.10(d).

The interfacial bonding process during co-extrusion can be separated into three different stages: primary bonding, bond-surface extension, and elimination of original joining surface.<sup>26</sup> Figure 3.11 is a schematic representation of the development of the interface and the different stages: (a) faying

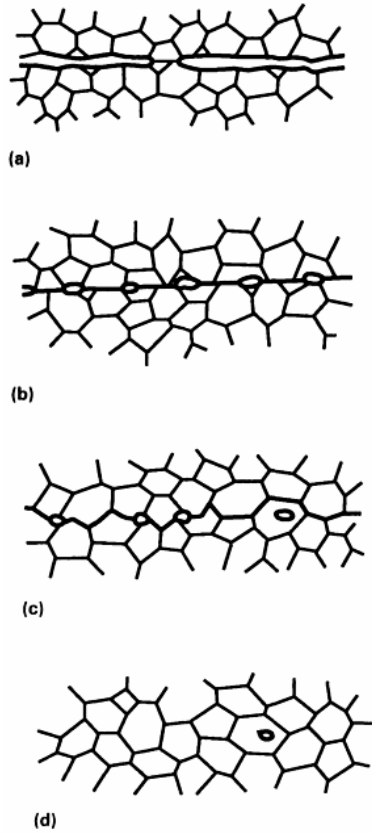


**Fig. 3.10. Stages of development in a diffusion bond.** (a) initial contact: limited to a few asperities (at room temperature), (b) first stage: deformation of surface asperities by plastic flow and/or creep, (c) second stage: grain boundary diffusion of atoms to voids and grain boundary migration, and (d) third stage: volume diffusion of atoms to the voids.

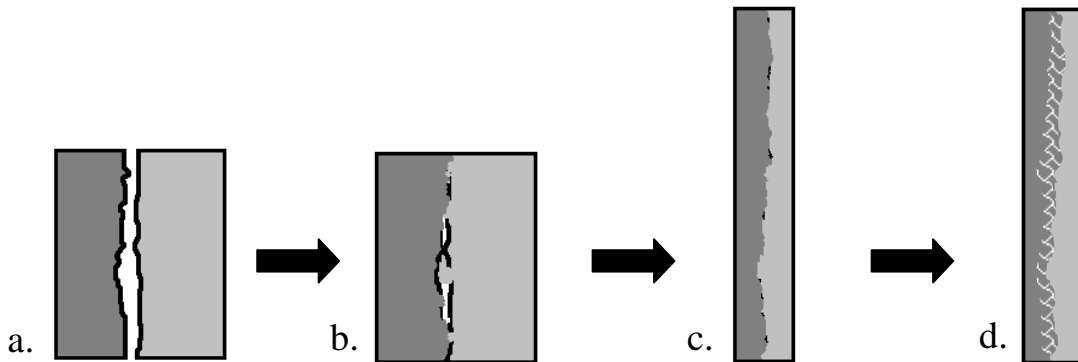


**Fig. 3.11. Stages of development in a co-extruded bond.** (a) initial surfaces, (b) primary bonding, (c) bond-surface extension, and (d) elimination of the original surface.

surfaces are covered by a layer of surface oxidation/film, (b) primary bonding: initial contact of surfaces causes break up of surface oxide as asperities deform locally, (c) bond-surface extension: bulk plastic deformation (metal flow) occurs which generates new film-free surface area; small amounts of film/oxide are still trapped in the interface, and (d) elimination of original surface: film is dissolved into solution, microstructural changes occur in the regions near the bond.

During primary bonding, Figure 3.11(b), asperities and localized deformation act to break up surface oxidation and surface layers (surface layers are indicated by the heavy black line in the figure). This allows for metal-metal contact and the beginnings of the bond to develop. Fresh material is exposed allowing for initial diffusion between the materials. Surface oxidation may be present as a result of room temperature or preheat surface oxidation. Oxides typically reduce diffusion of atomic species, which prevents a full adherent and tenacious bond between the two alloys. Pressure at the interface between the materials composing the pre-extruded bimetallic billet may result from either initial deformation / upsetting in extrusion or residual stresses from “shrink fitting” of billet components.

Bond-surface extension, the second stage of the solid-state weld development, occurs when large-scale plastic deformation begins, Figure 3.11(c). Plastic flow is governed by applied stress and the mechanical properties of the materials involved. Conservation of volume governs that the surface area between the two materials will increase with deformation for a process such as extrusion and axial flow. Bonding improves due to several different effects: surface films and impurity layers may dissolve and return to solution, diffusion of elements across the interface may take place, and atoms located near the interface may re-orient themselves to facilitate stronger bonding. As a result of deformation heating (internal material friction and external frictional forces) and temperature increase these processes may be accelerated above initial material temperature.

The final stage of the weld development is the elimination of the original joining surface, Figure 3.11(d). Microstructural and subgrain changes such as recrystallization, grain growth, transformations, precipitation, and diffusion may occur. These reactions render the initial-near bond new microstructure and the metallic bond is completed. A new microstructure is noted in Figure 3.11(d).

### 3.1.3 Previous Work on Similar Alloy Systems

Similar ferrous alloy systems using austenitic stainless steels and plain carbon steels have been investigated for the co-extrusion process in recent years.<sup>17,18,20</sup> The focus of some of these studies was for applications in the power generation industry.<sup>3,17,18,20</sup> Commercial extrudates were produced and characterized; however, the main focus was only on chemical compatibility and microstructural evolution.

The five zones can be described as follows: Zone I is the base low alloy steel exhibiting ferrite/pearlite and a decarburized layer near the interface with the superalloy. Zone II occurs directly adjacent to the interface between the low alloy steel and the superalloy. A thin band of austenite is present on low alloy steel side. In low alloy iron based alloys, ferrite is generally the stable microstructural phase present at room temperature. This austenite band is caused by high Ni and Mn diffusion into the steel that stabilizes the higher temperature austenite. In Zone III, a large precipitate filled region,  $M_7C_3$  carbides are found near interface, while  $M_{23}C_6$  are found farther away from the interface. The precipitates are found on grain boundaries and the interiors of grains.  $M_7C_3$  carbides are carbon rich and therefore they are located nearest to the source of higher carbon content—the low alloy steel. Regions where carbon has not readily diffused show  $M_{23}C_6$  type carbides. Zone IV marks the lower amount of precipitates region, where the  $M_{23}C_6$  type carbides are located at the grain boundaries. Zone V is composed of the bulk material, in this case—superalloy base metal.

Precipitates form preferentially at grain boundaries due to increased diffusivity (pipe diffusion) as well as the boundary acting as a site for heterogeneous nucleation. Heterogeneous nucleation is energetically favorable to homogeneous nucleation due to the reduction of surface energy that occurs by grain boundary nucleation. Each precipitate that nucleates and grows reduces the amount of high energy surface at the intersection between adjacent grains.

## **3.2 Modeling and Simulation**

### **3.2.1 Finite Element Modeling**

The FEM is a method used to solve engineering problems through numerical analysis. The process relies on the use of fundamental equations related to material behavior and established mathematical approaches to iteratively solving the equations to determine state variables such as stress, strain, strain rate and temperature related to a given deformation problem.

Decreasing costs associated with computer hardware and the increased availability of software and increasing costs associated with “in-house” experimentation are driving forces for use of FEM in industrial practice. Proper use of FEM can result in lower turn around times from design to product.

Commercial and in-house/self-programmed versions of FEM code are used to solve a large number of engineering related problems. Each version has its own advantages and disadvantages which must be understood before applying the solutions. For the work performed in this project, DEFORM-2D commercial FEM package was used.

With the increasingly important role of FEM in the manufacturing process for both design and process and product optimization, it is important to understand how to approach the engineering or scientific problem using this technique and how to interpret the results. Additionally, the drawbacks must be identified and methods to rectify them should be determined. Ultimately, the results of the research will be used to couple data gathered from experimentation and physical simulation enhanced by numerical simulations in order to improve analysis that can be performed using commercially available simulation packages.

Currently, there are several pieces of information that are not predicted by commercial FEM packages and therefore additional experimental and characterization resources are still needed. The ability of FEM code to simulate complex microstructural reactions and chemical changes is still limited. Microstructure development and the resultant mechanical properties cannot easily if at all be modeled today and normally only average or general mechanical properties are given for a deformed work piece. By utilizing FEM software to determine processing variables stress, temperature, strain, and strain rate, physical models can be performed without using actual extrusions.

### **3.2.2 Thermomechanical Simulation**

In order to simulate complex microstructural development on a laboratory scale, thermomechanical simulation is used. State of the art FEM packages are limited in the amount of microstructural development simulation that can be successfully achieved and thus the use of thermomechanical simulation is still widespread.<sup>16,17</sup> Typically, a material is subjected to a processing path that involves a series of time at temperature, strain, strain rate, and pressure steps. This can be achieved by using a unit such as a Gleeble. The Gleeble uses resistive heating so that temperatures can be monitored and controlled with a high degree of accuracy. Samples can be subjected to tension, compression, or torsional loading. Strain rates can be varied over several orders of magnitude. Operations are controlled by a computer, and multiple operations may be performed on a single sample. Data is

collected by the computer as well. Typical uses for a Gleeble unit include flow stress measurements as a function of temperature, strain, and strain rate, welding HAZ development simulations, recrystallization studies, as well as mechanical testing.

For this research, results from FEM simulations are used to simulate the microstructural development between the stainless and plain carbon steels. Temperature is determined from the billet preheat and simulation is performed isothermally. Strain and strain rate values have been taken from the interface in regions of the extrudate that have been examined in the industrially prepared samples. This is used to verify the feasibility of using the Gleeble to model the process. The maximum strain and strain rate for the different extrusion conditions are used to model the bond development between the materials using the Gleeble. This method allows for the simulation of the co-extrusion process to be performed without using an industrial process. Because of the costs associated with manufacturing multi-material billets as well as labor and press time, a movement to modeling in preparation of new and innovative products is underway. Successful and accurate modeling encourages new product development at lower costs and at a faster rate to final product and market.



## 4. Results and Discussion

Results of work carried out during this project are presented under the major topic areas of billet design, analysis of extrusion eccentricity, and metallurgical interface development studies.

### 4.1 Billet Design for Extrusion of Bimetallic Tubes

#### 4.1.1 Billet Materials and Chosen Conditions

In this activity, a new billet design was explored in an effort to control material flow during the co-extrusion of plain carbon/stainless steel tubes. The stainless steel type 304 was used as the core, and carbon steel, 1020, was used as the sleeve. The core and sleeve thickness and length used in this project are summarized in Table 4.1. The billet geometries listed in Table 4.1 were extruded using a low- and high-extrusion ratios of  $R = 3.3$  and  $10.6$ , respectively.

**Table 4.1. Billet geometry identification**

| Sample ID | Core thickness (mm) | Sleeve thickness (mm) | Core length (mm) | Core length (% of billet) |
|-----------|---------------------|-----------------------|------------------|---------------------------|
| Low1      | 11.4                | 38.1                  | 127.0            | 100                       |
| Low2      | 11.4                | 38.1                  | 114.3            | 90                        |
| Low3      | 11.4                | 38.1                  | 101.6            | 80                        |
| High1     | 11.4                | 38.1                  | 127.0            | 100                       |
| High2     | 11.4                | 38.1                  | 114.3            | 90                        |
| High3     | 11.4                | 38.1                  | 101.6            | 80                        |

For each billet set, identified by an extrusion ratio (i.e., low or high), there were three billets: one with a full-length core (designated by the numeral “1” after the letter), one with the core shortened 10% (designated by the numeral 2 after the letter), and one with the core shortened 20% (designated by the numeral 3 after the letter). The center-hole diameter was 38.1 mm, billet length was 127 mm, and the overall billet diameter was 137.2 mm.

#### 4.1.2 Bimetallic Billet Assembly Procedure

Billet preparation for bimetallic extrusions is an important process to ensure that final extrudate properties are optimal. Proper assembly is needed so that the two materials in the composite billet will upset into the die chamber concurrently and so that they do not separate from each other during the initial part of extrusion (breakthrough). For the sleeve material, a slightly oversized plain carbon steel billet is selected. The outer surface of the billet is machined away to remove any impurities, oxidation, and undesirable grain structure resulting from initial production and casting. The center of the billet is machined with a hole slightly smaller than the diameter of the core starting billet size. The core material is prepared in a similar manner, with an outside diameter the size of the initial thickness in the billet and the center hole with a diameter slightly larger than the mandrel size. After final cleaning to remove any machining fluids, the billets are shrink-fitted together. The sleeve material, plain carbon steel, is heated in a furnace with an inert argon atmosphere so that it expands. The core material is chilled in liquid nitrogen in order to cause contraction. The two materials are put together and allowed to come to room temperature, where they are held together by the resulting thermal stresses. Figure 4.1 shows the assembled billet.

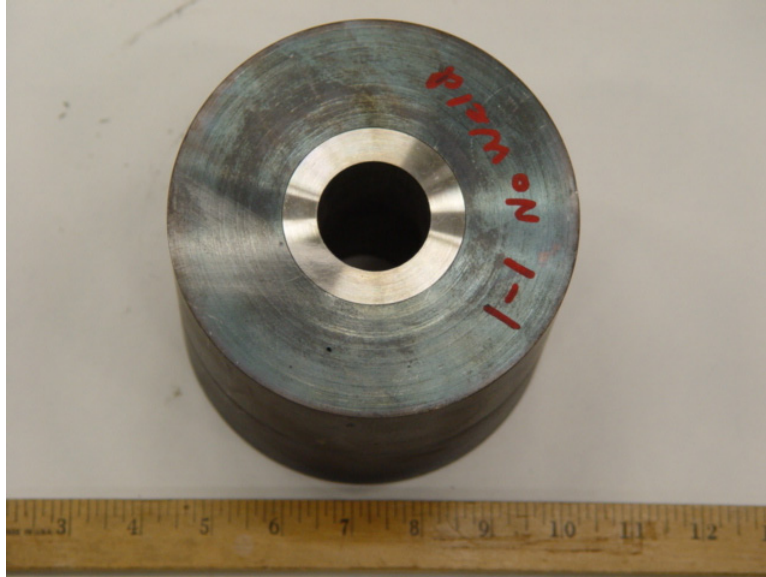


**Fig. 4.1. Front of shrink fitted bimetallic billet before welding (full-length core).** Stainless steel core and plain carbon steel sleeve.

The sleeve and core material are welded together at the front end of the billet where the interface is located. A weld bead is visible in the front end of the billets that are presented in Figs. 4.2 and 4.3 (full length and shortened core-length billets). A plate is welded to the back end of the billet that contains a vacuum degassing tube (Fig. 4.4).

The billets are vacuum degassed for several hours (Fig. 4.5) before the tube is crimped off and cut (Fig. 4.6).

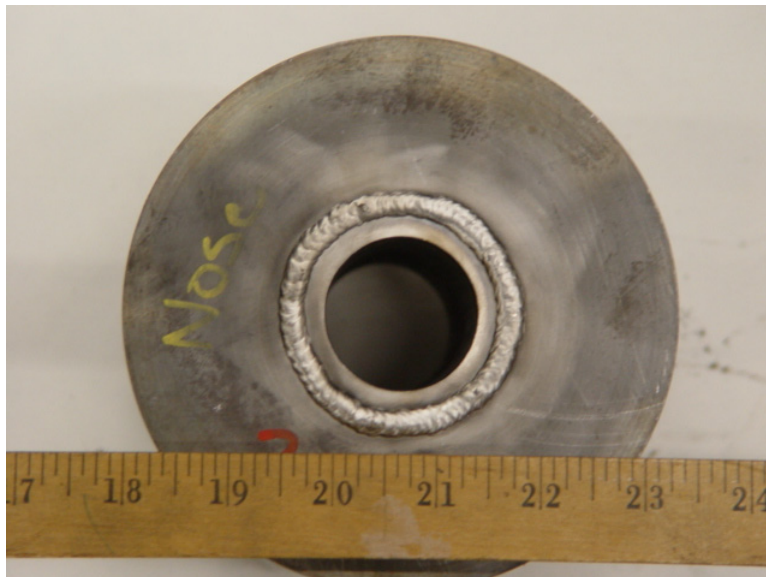


**Fig. 4.2. Front end of bimetallic steel billet with full-length core and weld.**

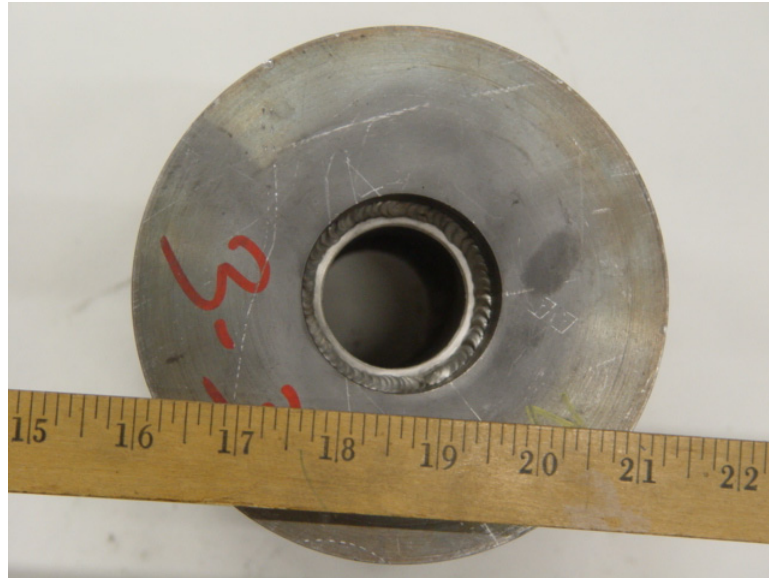


**Fig. 4.3. Front end of bimetallic steel billet with shortened core and weld.**



**Fig. 4.4. Back side of bimetallic steel billet with welds, weld plate, and degassing tube.**



Fig. 4.5. Bimetalllic billets being degassed.



Fig. 4.6. Back side of bimetalllic steel billet with welds, weld plate, and crimped-off degassing tube.

### 4.1.3 Extrusion Conditions

The low extrusion ratio billet set was preheated at 1100°C for two hours, and the high extrusion ratio billet set was preheated at 1200°C for approximately 2.5 h in a box furnace with a nitrogen atmosphere. They were lubricated with a graphite-based lubricant and extruded with a mandrel attached to the dummy block on a hydraulic press. A graphite pad (preheated with the billet) was placed between the dummy block and the billet so that the entire billet could be extruded. The die orifice was 82.6 mm for the low extrusion ratio and 55.6 mm for the high extrusion ratio.

After extrusion, the tubes were cut into either 25.4-mm- (low extrusion ratio samples) or 50.8-mm- (high extrusion ratio samples) thick slices, with one side prepared for optical measurement. Core and sleeve thicknesses were measured at four positions for each slice (12, 3, 6, and 9 o'clock). Prior to sectioning the tube, a reference mark was made so that the four measurement positions were constant throughout the tube length. Measurements were made using a macro camera interfaced with a Leco 3001A Image Analysis software package.

Figures 4.7 and 4.8 show the average actual core thickness measurements versus distance from the front of the extrudate for each of the two experimental billet sets (see Table 4.1). For the low extrusion ratio samples, the 80% length core samples show that the maximum front end core thickness is the lowest (sample Low3). The results for the high extrusion ratios show that 80% recessed core samples exhibit nearly the same core thickness distribution. It is important to note that the first core thickness measurement was taken approximately 50.8 mm from the front of the extrudate for the high extrusion ratio (which showed some uneven breakthrough flow) and may not have captured the initial maximum core thickness.

#### 4.1.4 Finite Element Modeling Simulation using DEFORM-2D and Experimental Validation (Case 1)

The FEM simulation was performed using DEFORM-2D software version 8.1. To simulate the performed experiments, an isothermal simulation was run with the material temperature at either 1100 or 1200°C, corresponding with the actual extrusion experiments. The core deformation was modeled using a mesh with 2000 elements, and the sleeve simulation used a mesh of 1500 elements. Since the simulation was axi-symmetric, only one-half of the billet and process was simulated. Friction was

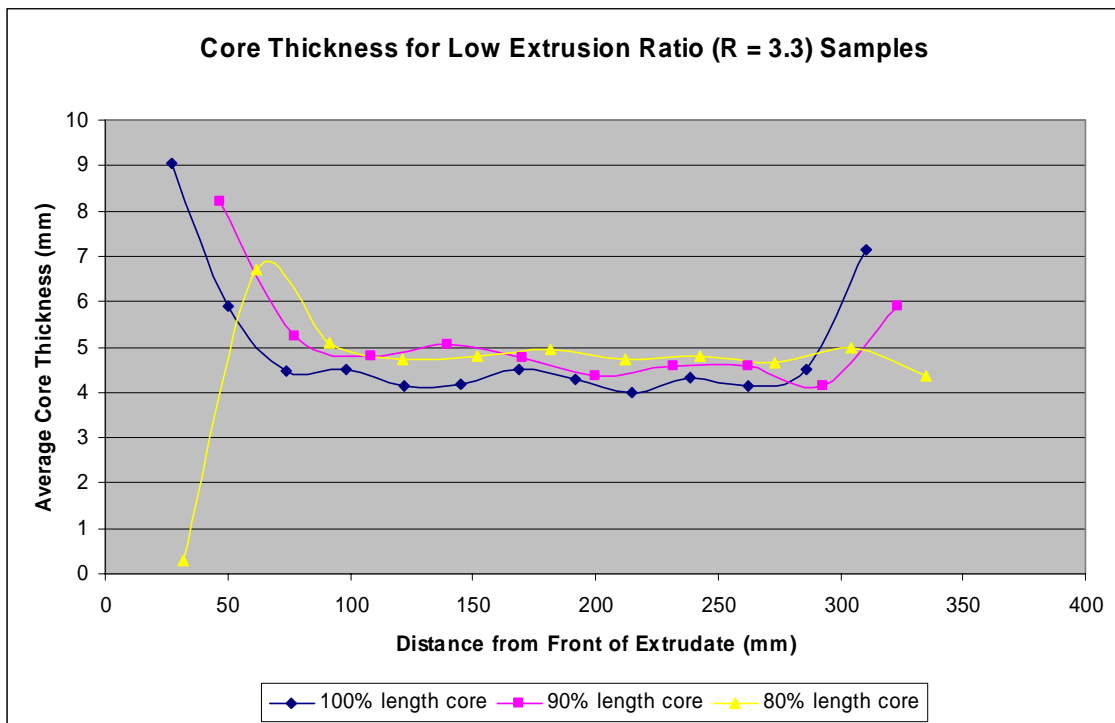
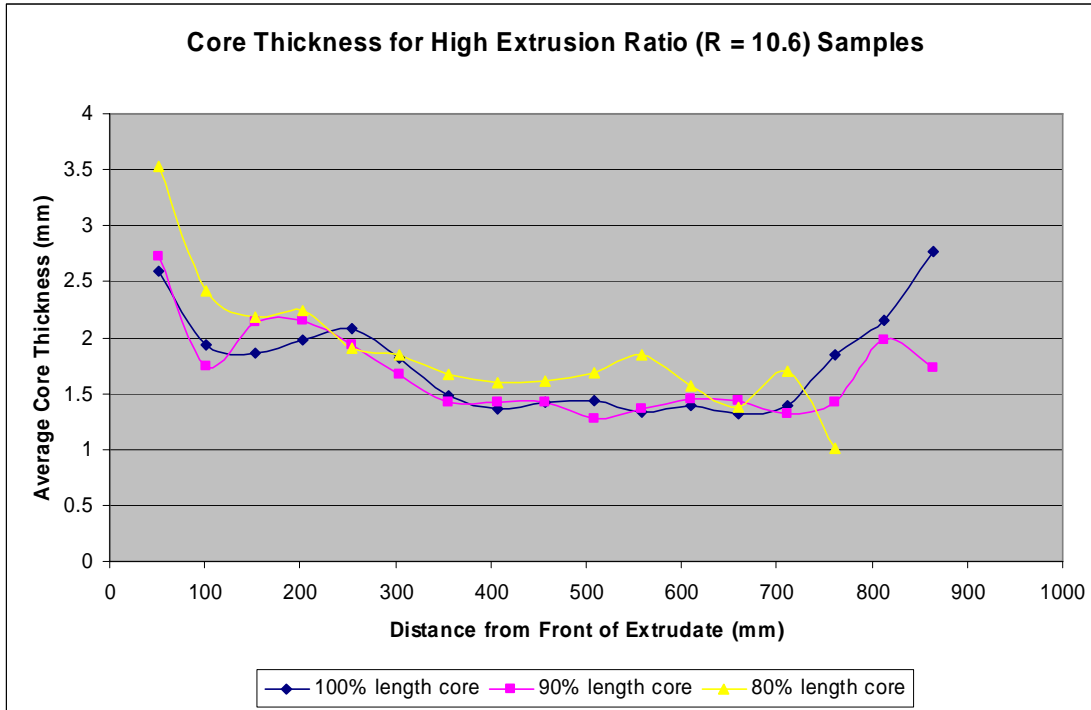


Fig. 4.7. Comparison of average core thickness for the low extrusion ratio extrudates.



**Fig. 4.8. Comparison of average core thickness for the high extrusion ratio extrudates.**

defined as shear equal to 0.3 between all billet surfaces (regardless of material) and the die, container, and mandrel. Between the core and sleeve material, friction was set as shear equal to 0.7, with sticking friction at the end nodes on both the front and back of the billet between the two materials (to simulate the welds on the billet). The die and container were modeled as one object. The flow stress data for 1025 plain carbon steel is included with the software database and was used to simulate the 1020 steel. The 1020 and 1025 plain carbon steels exhibit similar flow stress and extrusion characteristics at the simulation temperature.

Core thickness data points were extracted from the FEM simulations and were compared to the core thicknesses measured on the actual extrudates. For the extrudates, the average core thickness value was calculated for each slice from the four measurements. Core thickness was plotted as a function of tube length from the front of the extrudate. It is important to note that for the actual extrudates, data points only exist at discrete intervals and not in a continuous manner like the results from the FEM simulations. Due to uneven flow that is present at the front of the extrudate, the best effort was made to create the first slice after the core material began to extrude (as in the case of recessed core billet geometries). Because the early flow of the core material exhibits the most eccentricity during the initial extrusion, it is the most difficult to accurately measure the core thickness in the front of the extrudates. In all but one case for the results presented here, as well as in the overwhelming majority of the cases that were investigated but not presented here, the maximum eccentricity is observed within the front 20% of the extrudate, which occurs before the onset of steady state extrusion. In the few cases where the eccentricity was not in the initial part of the extrudate, it came at the last portion of the extrudate as a result of being extruded with a graphite pad. Graphite pad(s) are placed between the billet and the mandrel so that 100% of the billet can be extruded, which is caused by the graphite pad deforming and fracturing as it is pushed through the die (a small amount may remain on the mandrel and the dummy block). When the pad deforms, it causes a cone-shaped defect at the back end of the extrudate. The back ends of the extrudates were generally unable to be measured due to the cone defect.

Comparison of FEM results and the actual extrudates is presented for many process conditions in the form of graphs (Figs. 4.9–4.11 and 4.13–4.15). Development of the extrudate front end is illustrated

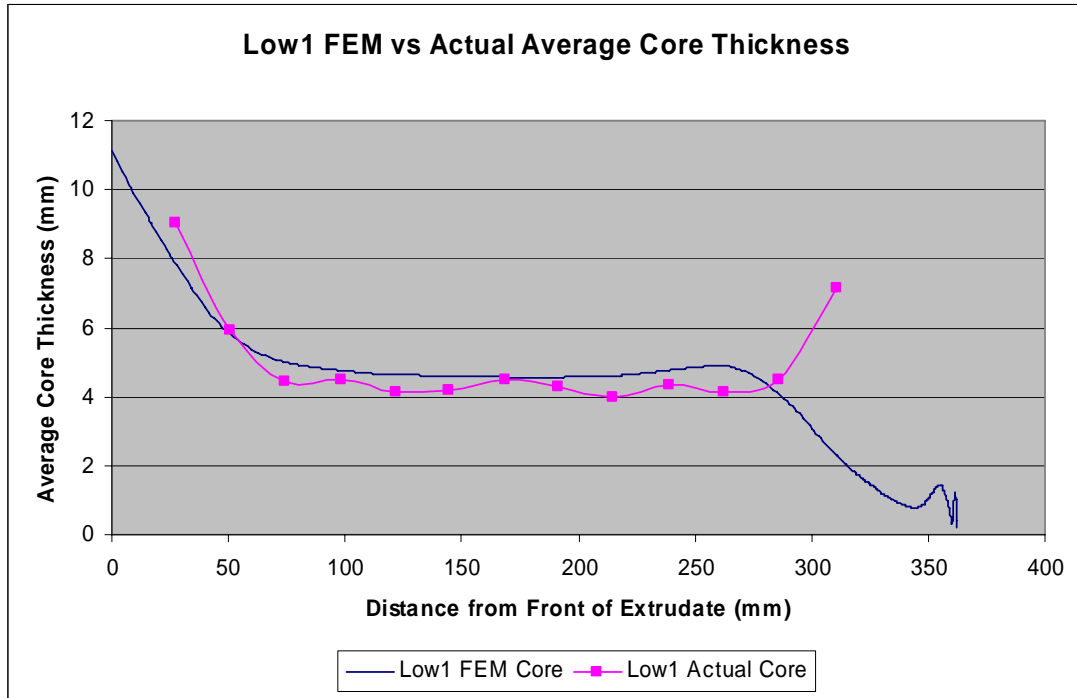


Fig. 4.9. Finite element modeling versus actual average core thickness as a function of distance for sample Low1.

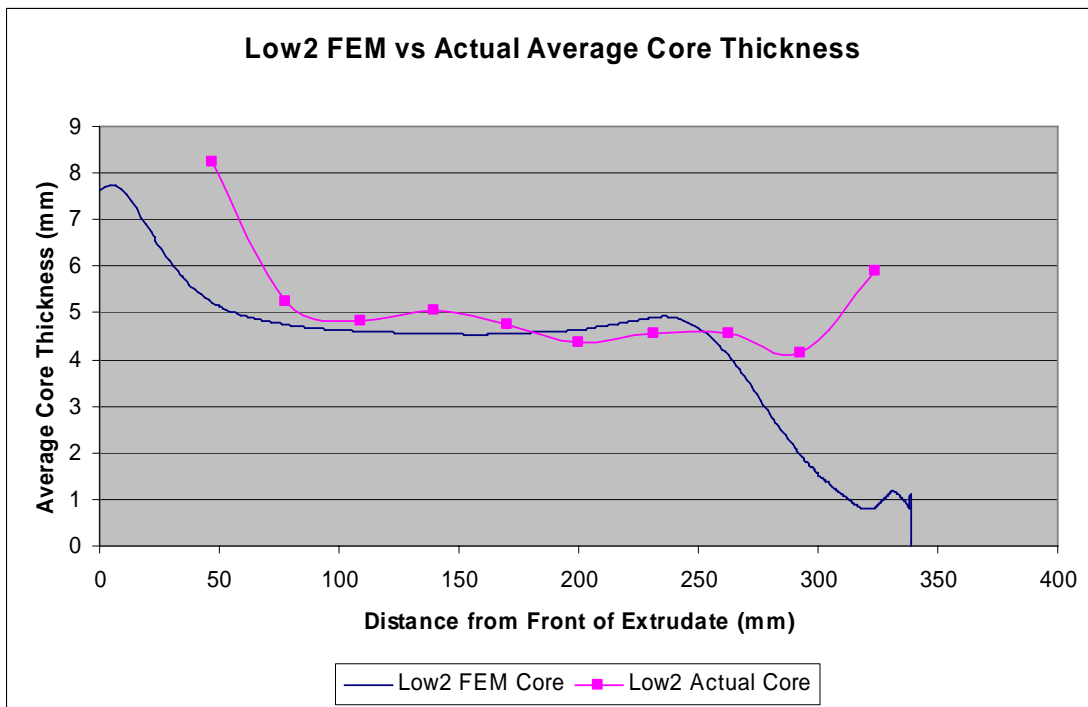


Fig. 4.10. Finite element modeling versus actual average core thickness as a function of distance for sample Low2.

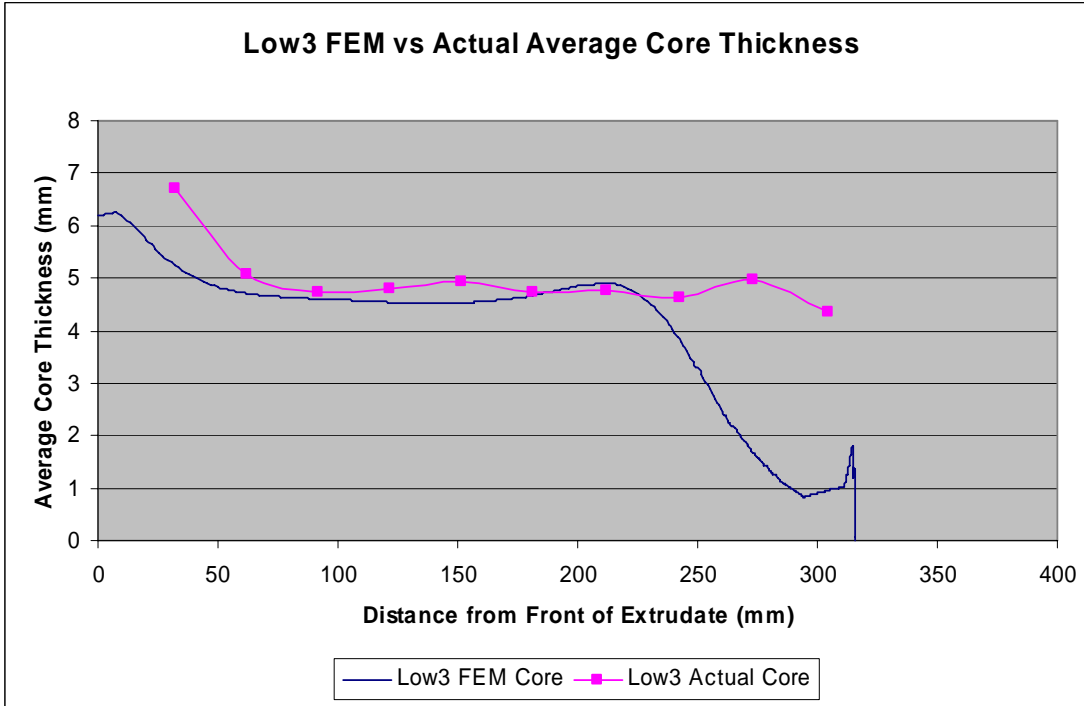


Fig. 4.11. Finite element modeling versus actual average core thickness as a function of distance for sample Low3.

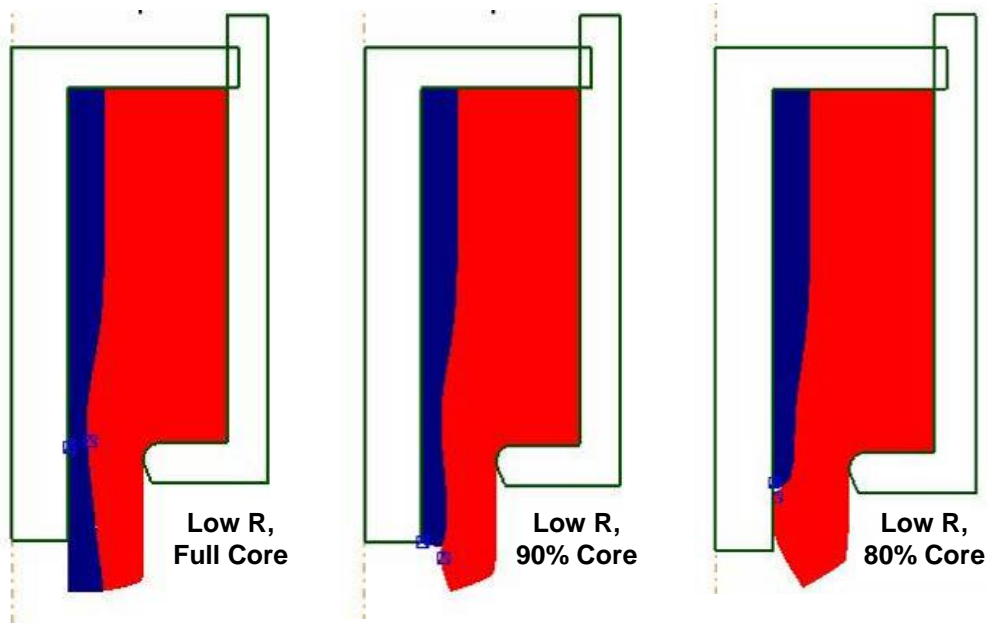


Fig. 4.12. Finite element modeling at early stage of extrusion and front-end geometry development for low extrusion ratio extrudates.



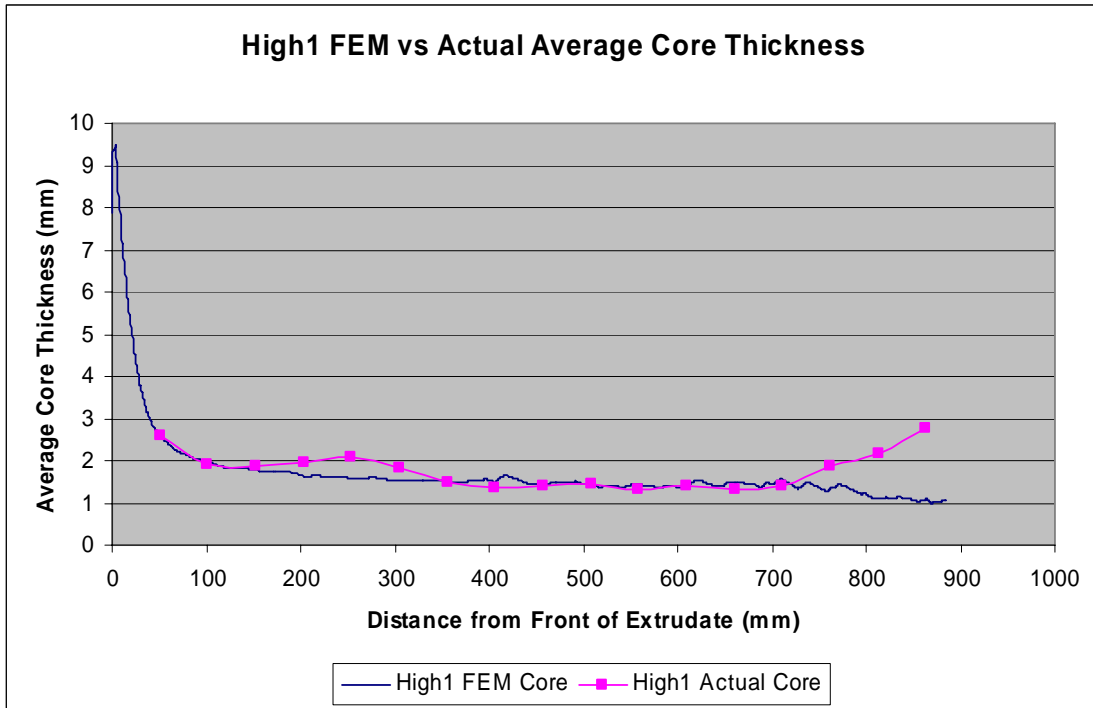


Fig. 4.13. Finite element modeling versus actual average core thickness as a function of distance for sample High1.

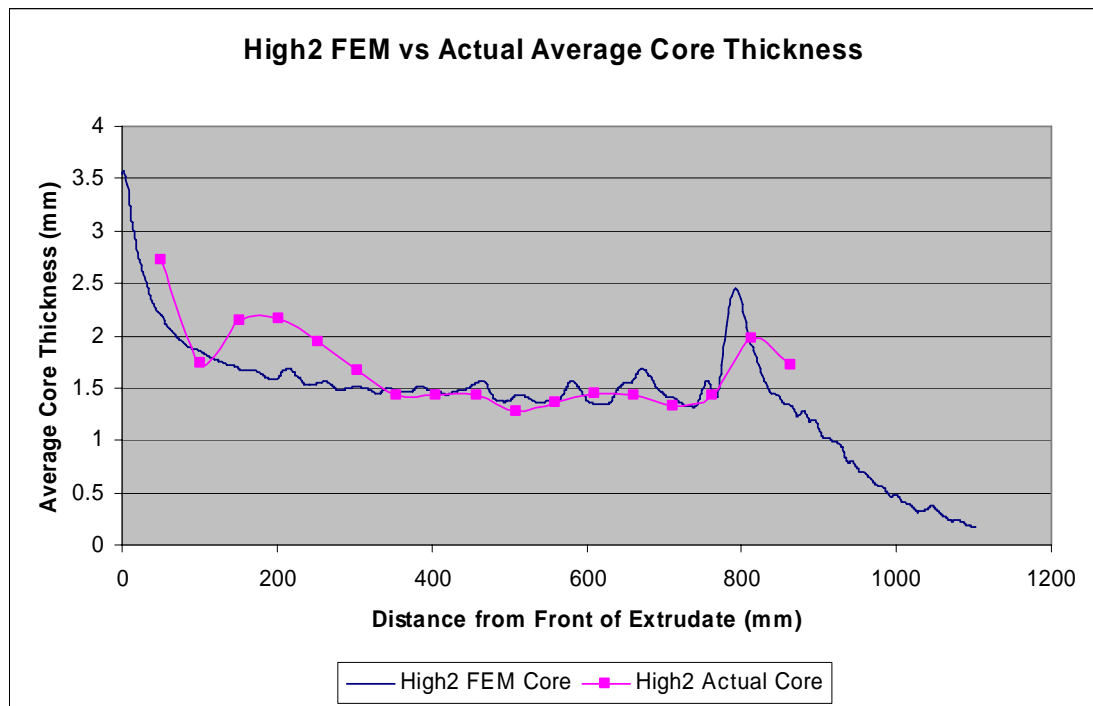
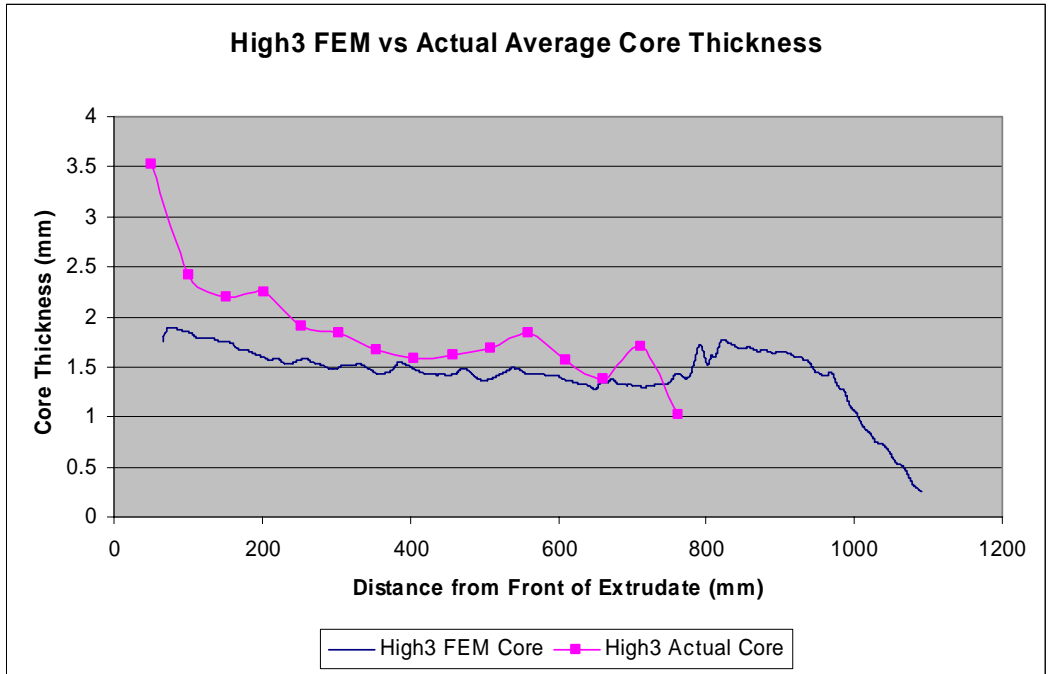
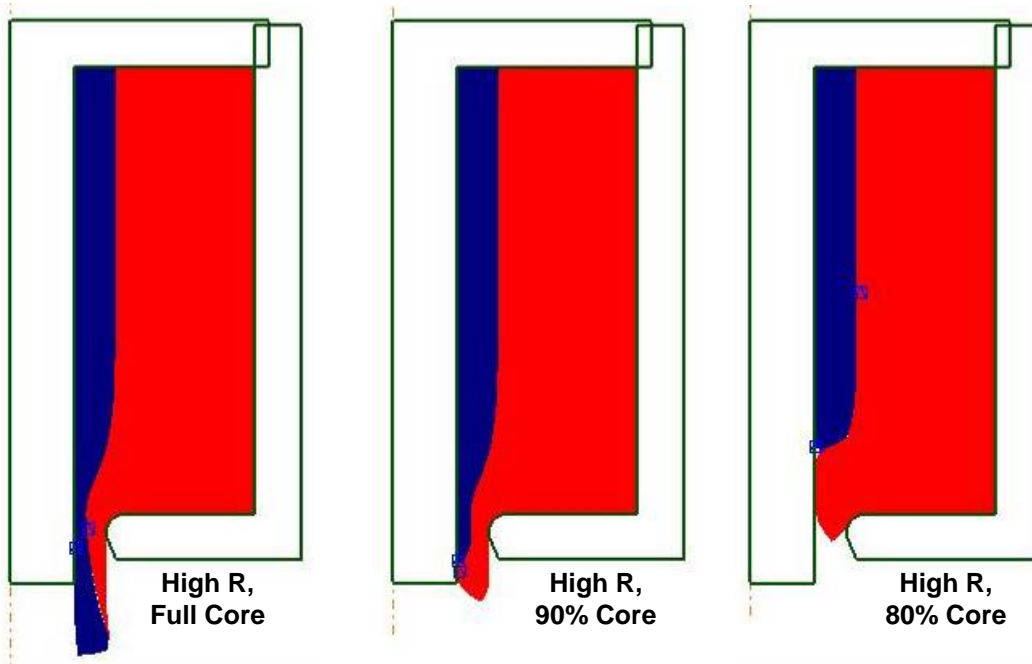


Fig. 4.14. Finite element modeling versus actual average core thickness as a function of distance for sample High2.



**Fig. 4.15. Finite element modeling versus actual average core thickness as a function of distance for sample High3.**

in Figures 4.12 and 4.16, based on the FEM predictions. Figure 4.17 shows a comparison of the FEM results for the high extrusion ratio sample set, which is representative of the results for all of the simulations. All three extrusions show similar results except for the front end core thickness. Note that the graph has been truncated at 4 mm on the y-axis and 1000 mm on the x-axis, cutting off some of the core thickness for the full-length core sample.



**Fig. 4.16. Finite element modeling at early stage of extrusion and front-end geometry development for high extrusion ratio extrudates.**

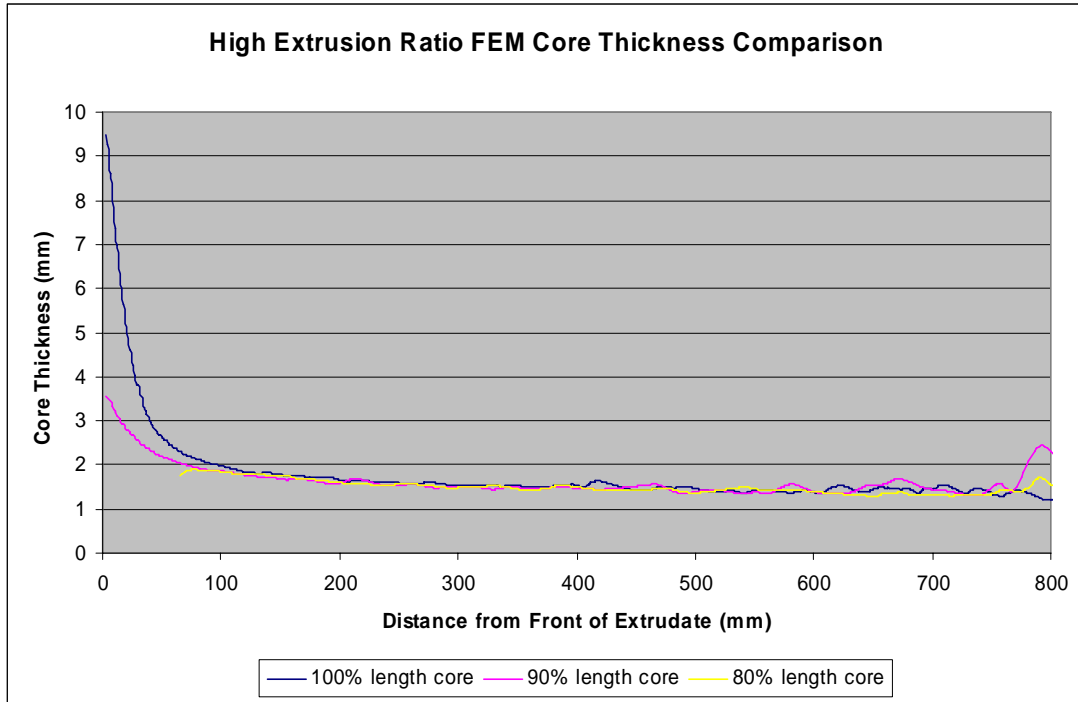


**Fig. 4.17. Comparison of finite element modeling predicted core thickness for high extrusion ratio samples.** Note that the graph has been truncated at 800 mm on the x-axis.

The ratio of core to sleeve material was calculated for the initial billet (0.3) as well as in the steady state region of extrusion for both the billet sizes (shown in Figs. 4.1 through 4.6) experiments and the FEM simulations. The results are presented in Table 4.2.

**Table 4.2. Ratio of core to sleeve thickness from the steady state region after extrusion<sup>a</sup>**

| Sample | Actual $D_{cf}/D_{sf}$ | FEM $D_{cf}/D_{sf}$ | Core length (%) |
|--------|------------------------|---------------------|-----------------|
| Low1   | 0.22                   | 0.24                | 100             |
| Low2   | 0.25                   | 0.24                | 90              |
| Low3   | 0.26                   | 0.24                | 80              |
|        |                        |                     |                 |
| High1  | 0.16                   | 0.18                | 100             |
| High2  | 0.16                   | 0.17                | 90              |
| High3  | 0.21                   | 0.17                | 80              |

<sup>a</sup>Ratio for unextruded material = 0.3.

Both experiments show strong agreement between the results predicted by FEM and the results that were obtained from the actual extrusion experiments. The low extrusion ratio simulations show that the onset of core material thickness shifted slightly towards the front end of the extrudate; however, the distribution is similar to the actual results.

#### 4.1.5 Finite Element Modeling Simulation Using DEFORM-2D and Experimental Validation (Case 2)

The second case of the FEM analysis was carried out on the billet geometry given in Table 4.3.

**Table 4.3. Billet geometry identification for Case 2**

| Sample ID | Core thickness (mm) | Sleeve thickness (mm) | Core length (mm) | Core length (% of billet) | Extrusion ratio |
|-----------|---------------------|-----------------------|------------------|---------------------------|-----------------|
| B1        | 24.8                | 24.8                  | 127.0            | 100                       | 3.3             |
| B2        | 24.8                | 24.8                  | 114.3            | 90                        | 3.3             |
| B3        | 24.8                | 24.8                  | 101.6            | 80                        | 3.3             |
| F1        | 6.35                | 43.2                  | 127.0            | 100                       | 10.6            |
| F2        | 6.35                | 43.2                  | 114.3            | 90                        | 10.6            |
| F3        | 6.35                | 43.2                  | 101.6            | 80                        | 10.6            |

Figures 4.18 and 4.19 show the results of the average core thickness for the extrudates produced from billets extruded at ORNL. Figure 4.18, the B-Series extrudates, show that there is no difference in the core thickness during steady state extrusion and that the onset of steady state occurs sooner in the shortened core samples. Figure 4.19 shows that in the case of the high extrusion ratio with low initial core thickness, there is variation in thickness throughout the extrudate. This variance in core thickness occurs regardless of the initial core length.

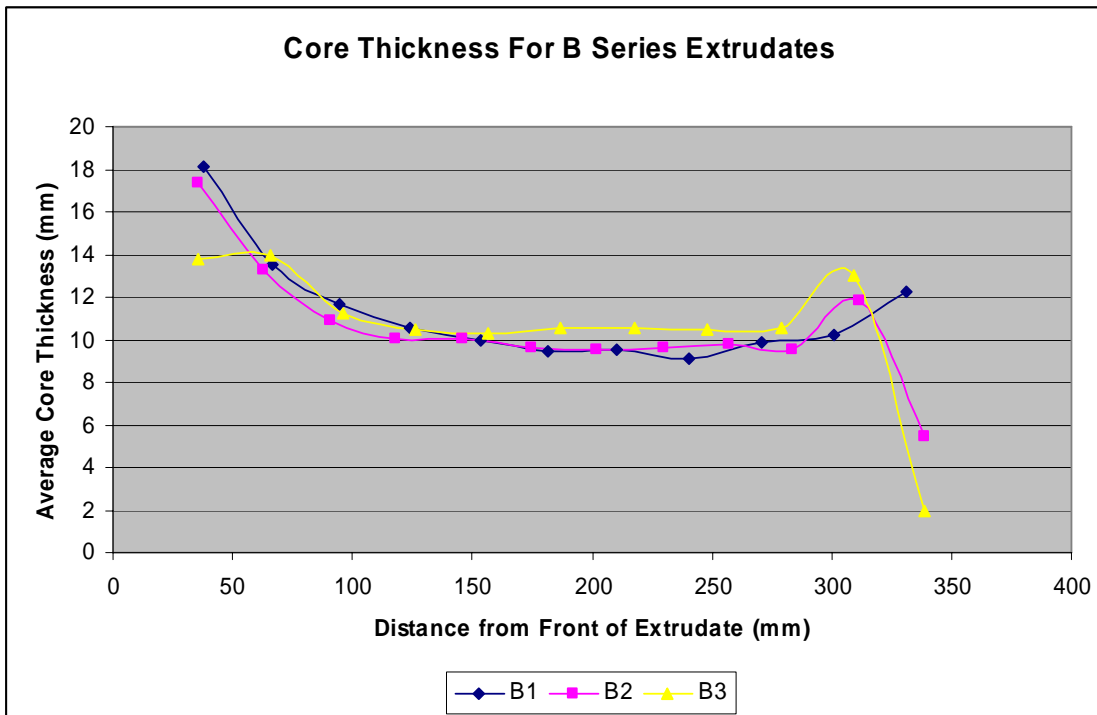


**Fig. 4.18. Comparison of average core thickness for the B-Series extrudates.**

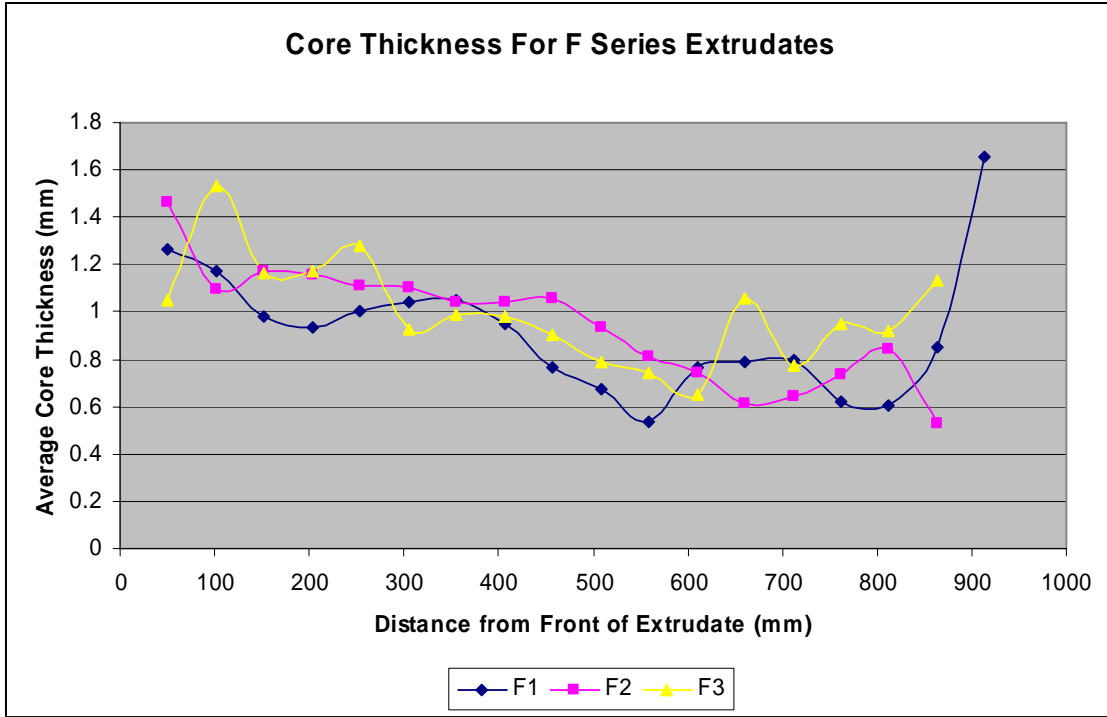


Fig. 4.19. Comparison of average core thickness for the F-Series extrudates.

Figures 4.20, 4.22, and 4.24 show the comparison of the FEM simulation results to the measured average core thickness results for the B-Series extrudates. The results are in agreement. Figures 4.21, 4.23, and 4.25 show the early stage extrusion behavior of the B-Series extrudates. As initial core

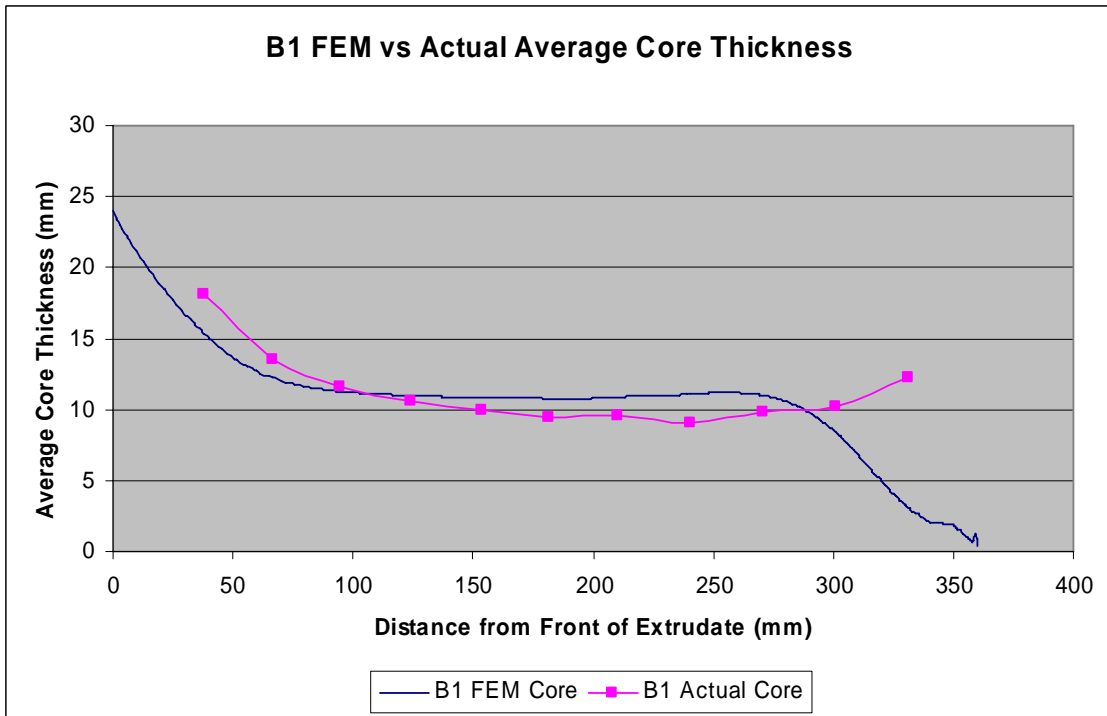


Fig. 4.20. Finite element modeling versus actual average core thickness as a function of distance for Sample B1.

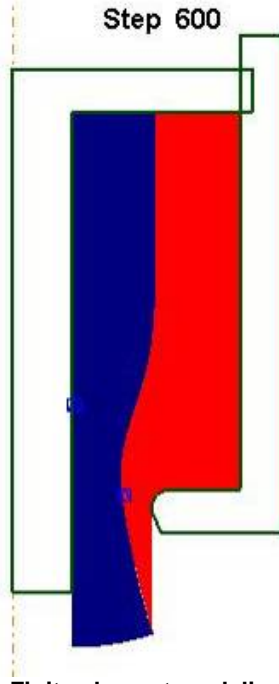


Fig. 4.21. Finite element modeling at early stage of extrusion and front-end geometry development for Sample B1.

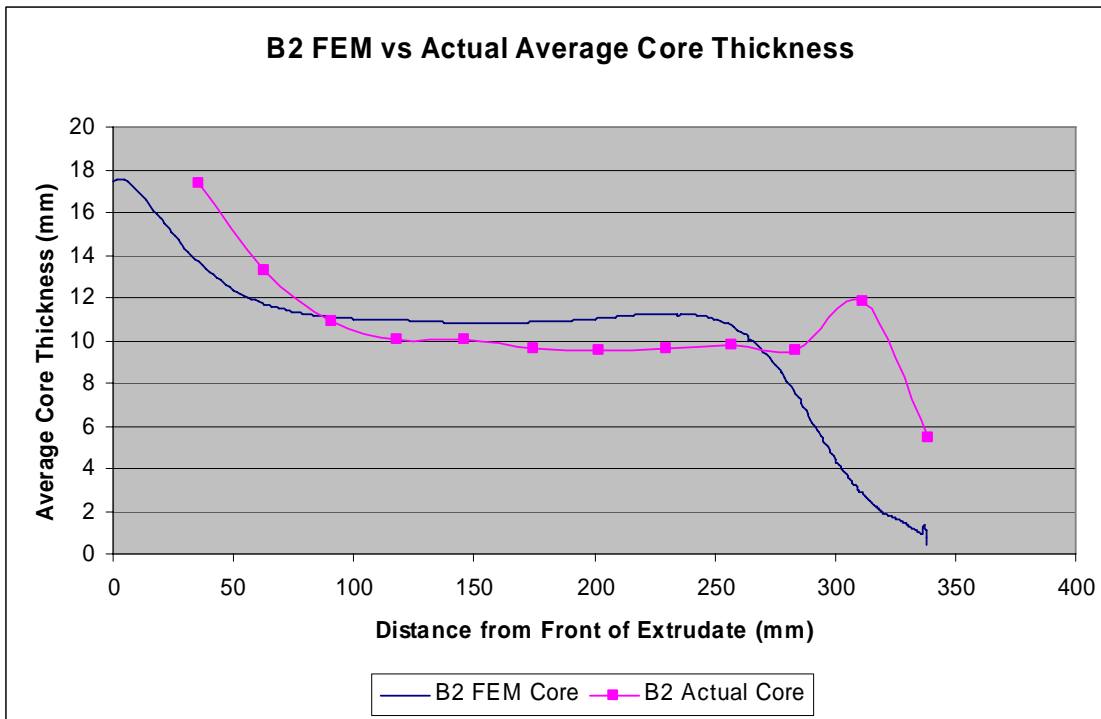


Fig. 4.22. Finite element modeling versus actual average core thickness as a function of distance for Sample B2.

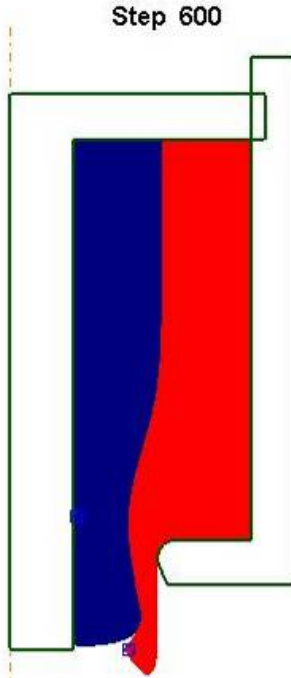


Fig. 4.23. Finite element modeling at early stage of extrusion and front-end geometry development for Sample B2.

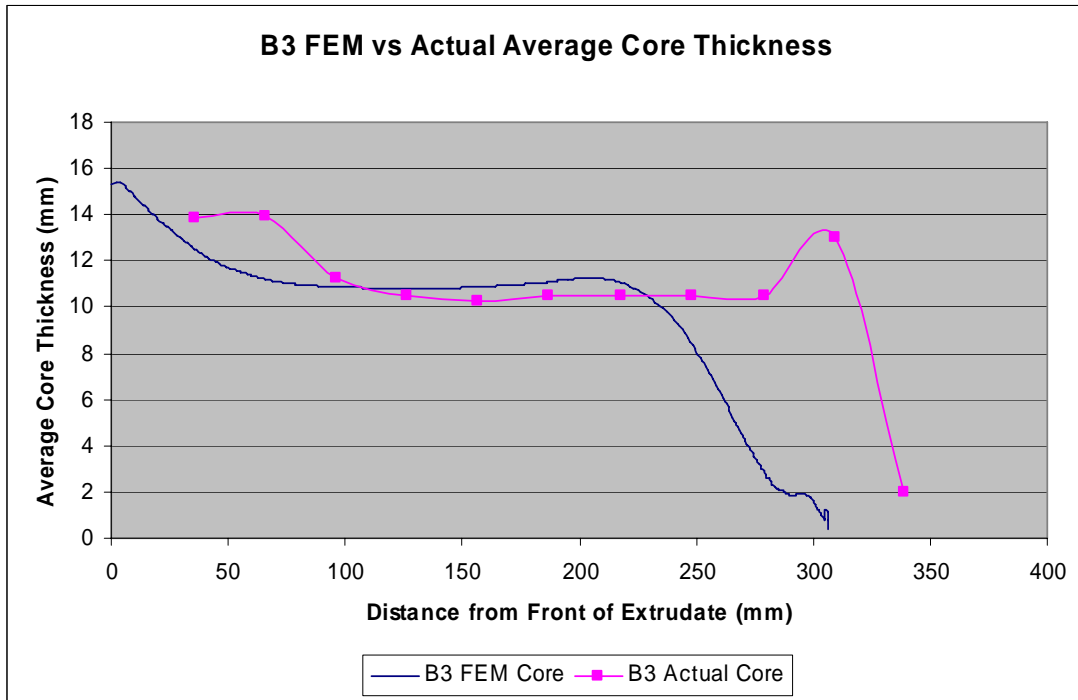
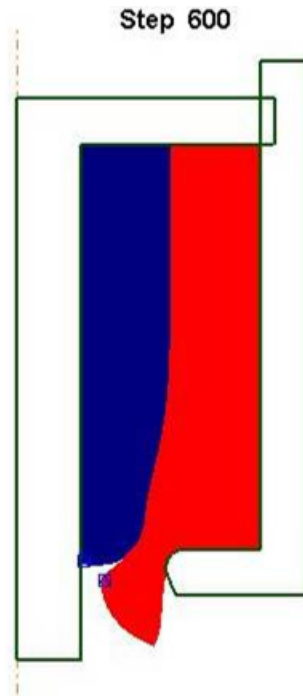


Fig. 4.24. Finite element modeling versus actual average core thickness as a function of distance for Sample B3.



**Fig. 4.25. Finite element modeling at early stage of extrusion and front-end geometry development for Sample B3.**

length decreases (progressively from Figs. 4.21 through 4.25), the amount of inward upsetting of the sleeve material increases. Concurrent flow is most prominent in the 10% recessed core.

Figures 4.26, 4.28, and 4.30 show the comparison of the FEM simulation results with the measured average core thickness results for the F-Series extrudates. It can be noted that agreement in results is good for the full-length core sample, but begins to break down when the core-shortened samples are investigated. This corresponds to the results noted when comparing just the actual extrudate results and the lack of agreement. Figures 4.27, 4.29, and 4.31 show the early stages of extrusion behavior of the F-Series extrudates. Again, concurrent flow is most promoted by the 10% recessed core, while the full-length core shows core ballooning, and the 20% decreased core shows significant sleeve flow prior to core flow.

As shown with other results presented previously in this report, these results show that core shortening of approximately 10% promotes concurrent flow.



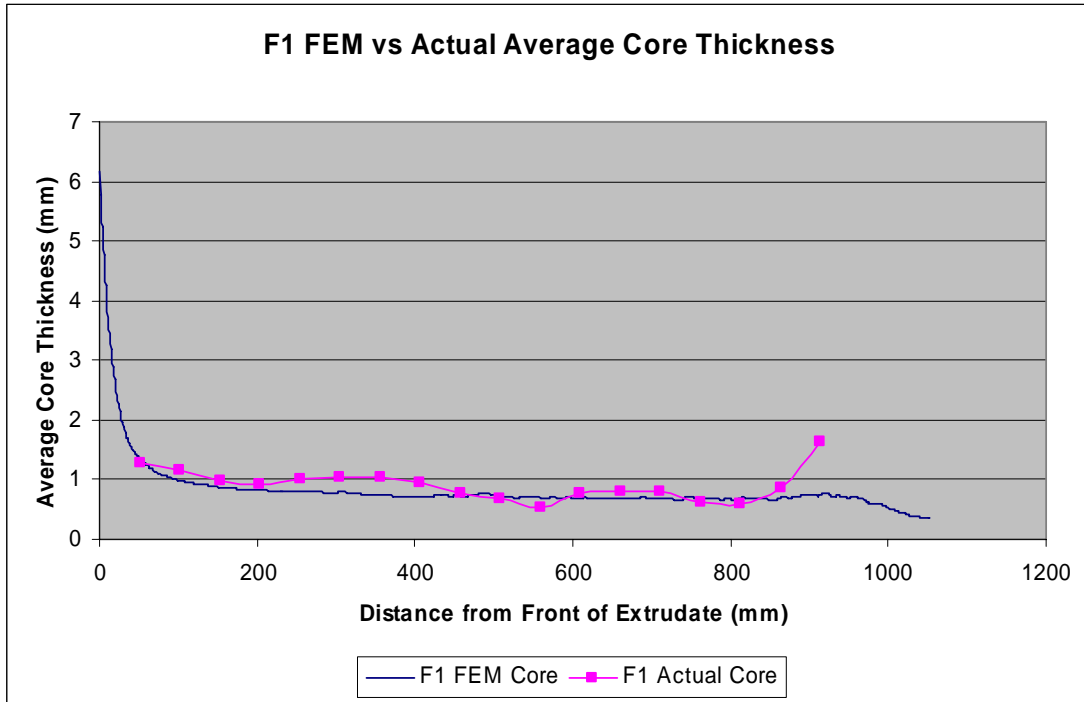


Fig. 4.26. Finite element modeling versus actual average core thickness as a function of distance for Sample F1.

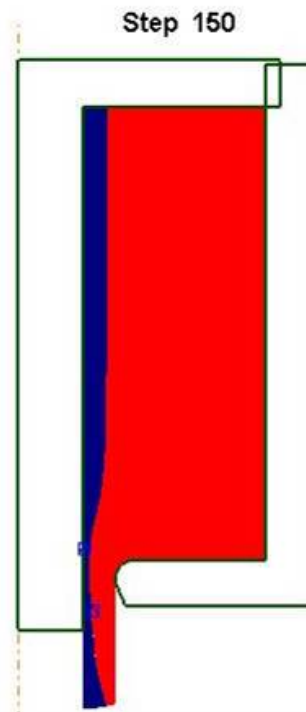


Fig. 4.27. Finite element modeling at early stage of extrusion and front-end geometry development for Sample F1.

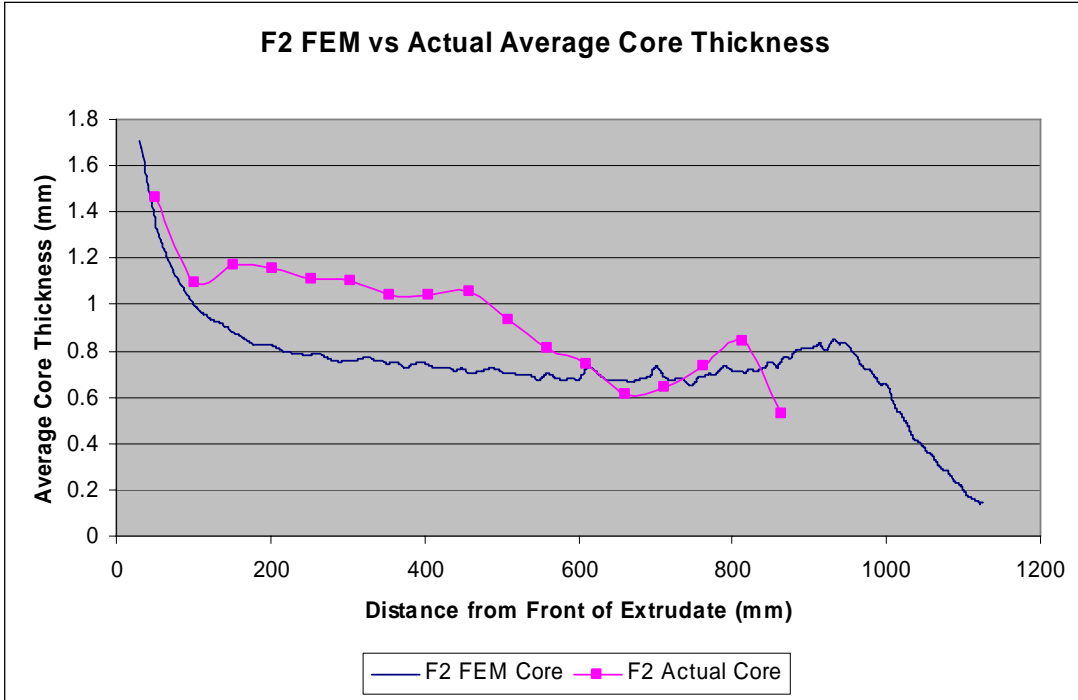


Fig. 4.28. Finite element modeling versus actual average core thickness as a function of distance for Sample F2.

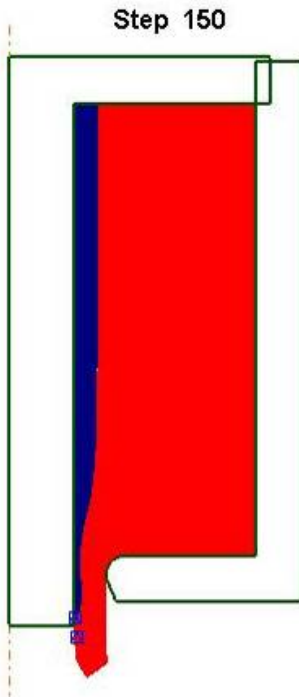


Fig. 4.29. Finite element modeling at early stage of extrusion and front-end geometry development for Sample F2.

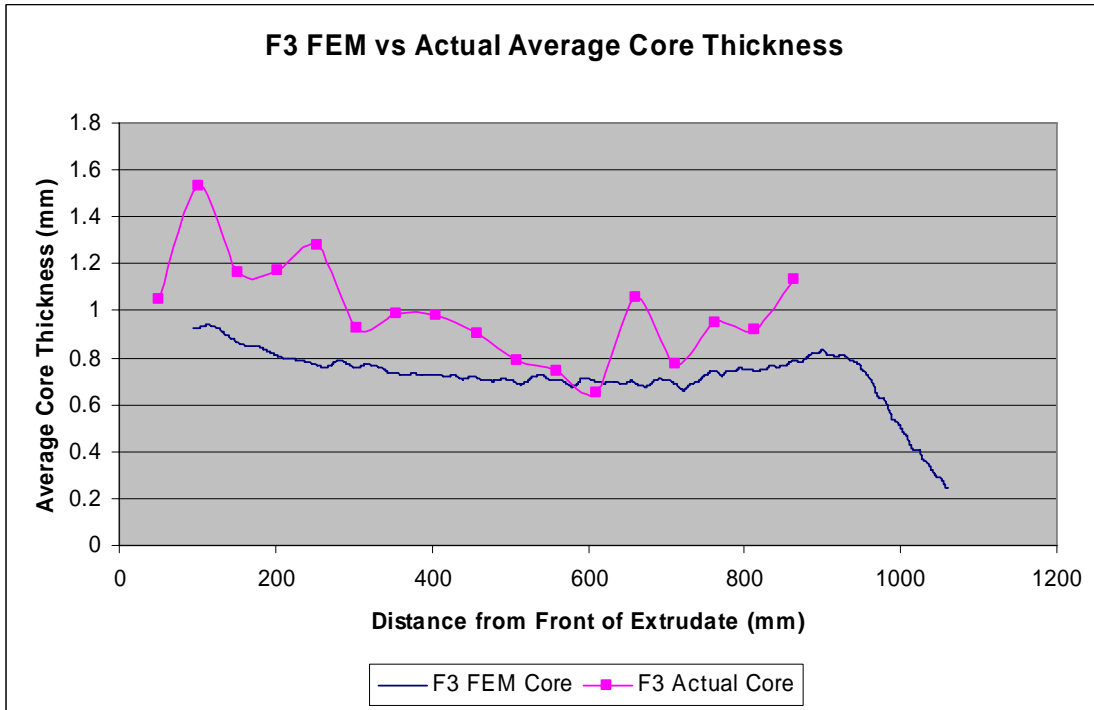


Fig. 4.30. Finite element modeling versus actual average core thickness as a function of distance for Sample F3.

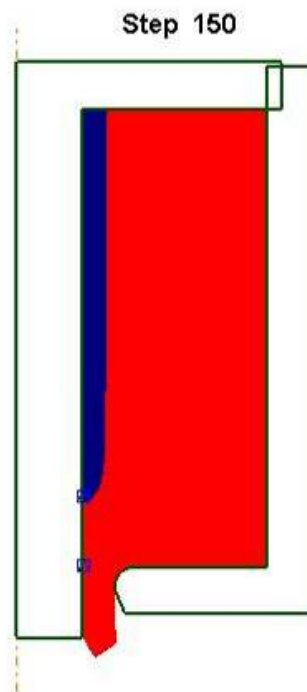


Fig. 4.31. Finite element modeling at early stage of extrusion and front-end geometry development for Sample F3.

#### 4.1.6 Discussion of Results for Finite Element Modeling Analysis of New Billet Design

The underlying motivation for this activity was to determine the feasibility of utilizing a commercial FEM package such as DEFORM-2D to design multi-component billets for co-extruded products. Typically co-extrusion is a process used to produce a composite product that involves one or more expensive alloys coupled with a support alloy that is less expensive. Uneven metal flow leading to front end defects produces waste that minimizes the impact of using a less expensive “backing” alloy. The use of a FEM package to perform initial modeling experiments allows for the design of new billets and reduces the amount of actual physical experiments that need to be performed. This eliminates costly experiments (including billet assembly), press-down time, and unnecessary extrudate analysis.

As shown in Fig. 4.17, the results from a series of FEM experiments for a particular billet set are in good agreement with physical experiments, showing differences only in the early stage extrusion behavior and consistent results during steady state extrusion. The most important and evident difference between the three simulations occurs at the core thickness distribution near the front of the extrudate. Although all three show front-end core thicknesses that are higher than the steady state values, the 80% core length sample shows little material that would be out of tolerance and therefore scrapped. This trend is repeated in all of the simulations, including both extrusion ratios.

When the core thickness data from the actual extrudates is compared to the FEM results, the agreement is good. Samples extruded using the lower extrusion ratio show the same general core thickness distribution as the simulations, but it is shifted back slightly in the extrudate.

The FEM simulations show that a billet with a core length 80% (out of the three conditions simulated) of the overall length produces the optimal extrusion results. For both the low and high extrusion ratios, this proves to be true in the actual extrusion experiments as well. Although low extrusion ratios promote concurrent flow of material,<sup>4</sup> an extrusion ratio of 3.3 appears to be high enough to benefit from a billet with a recessed core. This is illustrated in Figs. 4.9 through 4.11. When the core is the full length of the billet (samples Low1 and High1), the core extrudes at a thickness equal to or greater than its initial value. This is caused by a radial flow of the sleeve material into the core, forced by the full extrusion ratio imposed by the die. This radial flow causes the core material to be upset outward towards the die orifice, even though the initial core thickness may be much less than the die orifice. At lower extrusion ratios (larger die orifice), this phenomenon can be exaggerated more. Figures 4.12 and 4.16 illustrate the core “ballooning.” When the core is recessed to a value 80% of the initial billet length, the sleeve upsets to fill the gap left by the missing core material and extrudes ahead of the core material, causing scrap material. By reducing the core by only 10%, concurrent flow of both materials is promoted in both the low and high extrusion ratio scenarios. A reduction of 20% results in better or comparable material flow (depending on the extrusion ratio) and a savings in material in the initial billet that would become scrap.

Processing variables, such as ram speed, extrusion temperature, and material variables, such as flow stress, are either limited by the extrusion press or by the desired properties of the final product. According to Sliwa<sup>27</sup> in the case of a soft-sleeve/hard-core material, as is the case for this research, the material flow is simplified. For the case where there is a soft core material, the core flow will be promoted more because the sleeve material flow is more difficult. Core/sleeve thickness ratio in the initial billet is limited by the desired ratio in the final extrudate. The extrusion ratio is used to control the final extrudate size (and shape) and is limited by both the press container size and final product geometry. In addition to the length of the core material in the initial billet, front end material flow may be controlled by the die entrance angle. As shown by Apperley et al.,<sup>4</sup> low die angles force the

material to upset towards the core before flowing forward and out of the die, while high die angles cause the core material to flow forward and towards the core simultaneously. When the die orifice is larger than the initial core thickness, there is little resistance to the core material, and it will flow unimpeded during the beginning of extrusion. A low extrusion ratio (large die orifice) will allow the sleeve material to flow more concurrently with the core:<sup>4</sup> however, it has been shown in this work that even a low extrusion ratio of  $R \approx 3$  will benefit by reducing the core length in the billet. The effect of core length reduction is to allow for the sleeve material to “upset” into the region where the core material is missing and allow for it to then flow concurrently as the two materials experience breakthrough at the same time. The result is a reduction of scrap material at the front of the billet, concurrent material flow, and a reduction of costs associated with the reduction of 20% of the core material needed in the original billet. For other nonhollow, round-to-round extrusions using different alloy systems (aluminum), it has been shown that a reduction of approximately 10% is effective in controlling material flow.<sup>28</sup> Depending on the actual process variables, a reduction of 8 to 20% of the length of the core material in the initial billet will result in material scrap savings.

Sound proportionate flow is characterized by the ratio of core-to-sleeve material thickness in the billet equal to the ratio in the extrudate ( $D_{cf}/D_{si} = D_{cf}/D_{sf}$ ). When this ratio is not equal, sound flow may be still achieved, but it is not considered proportionate. Table 4.2 shows the ratio of core-to-sleeve material after extrusion ( $D_{cf}/D_{sf}$ ) for both the industrially prepared extrudates and the FEM simulations. The results from both show that for this set of extrusion conditions (die geometry, friction conditions, and material combination) the material underwent sound flow, but not proportionate sound flow. When comparing the results, good agreement is observed, further validating the use of DEFORM-2D to simulate the co-extrusion process. For both the low and high extrusion ratio industrial tests,  $D_{cf}/D_{sf}$  increases towards the billet value (0.3) as the core is shortened. This suggests that not only does the core-shortening method reduce the amount of front-end scrap, but it may promote proportionate flow.

The sudden rise in thickness of the core material at the back end of the extrudates (Low1, Low2, and High1) may be attributed to the formation of the cone defect caused by the deforming graphite pad during the final part of extrusion. In one of these samples, the eccentricity and material flow was more exaggerated. Previous studies<sup>12,13,14,28</sup> show that the core material behaves as in samples Low3, High2, and High3—it tapers off or “runs out” prior to the completion of extrusion.

Several factors can cause the discrepancy between the FEM and actual results. Friction was defined as equal on die surfaces in the simulations in an effort to simplify the solutions. The friction between the core and the sleeve in the billet was made as shear equal to approximately 0.7. In reality, the determination of the actual friction conditions between the two deforming billet materials is difficult to perform. Sticking friction is not entirely applicable, as evidenced by the need for welds on both the front and back ends of the billet to keep the two components from separating during extrusion. Die geometry varied slightly from the actual processing conditions to the FEM simulation, again, in order to simplify the solutions. Additionally, variations exist in flow stress between the models and actual extrusion. The simulations were run isothermally with no temperature gradient within the billet. For the 80% core length samples, considerable eccentricity occurred at the front of the actual extrudate due to the uneven flow between the sleeve and core materials. The sleeve material was the first to exit the die, and it folded in on itself, which led to considerable deviations in determining the “front” of the extrudate. In the full length core case, often the core extrudes faster and before the sleeve because it is not subject to as large a deformation. An overall extrusion ratio can be easily calculated for the process by comparing initial and final cross-sectional areas. In the case of the core material, very often its thickness is small enough to allow it to be within the die orifice diameter, effectively giving it a zero extrusion ratio if it were considered alone. Thus, in the full-length core case, the first part of

the core to extrude may not be subjected to deformation. As extrusion progresses, the core deforms, which leads to the “ballooning” that is observed in the final extrudate.

The core shortening method acts to control material flow at the front of the extrudate during the initial part of the extrusion process. In addition to minimizing the out of tolerance material in the front of the extrudate which directly corresponds to scrap, a material savings is realized in the initial billet by shortening the amount of core material. Upwards of 20% less of the core material can be used in the initial billet while still extruding the same amount of in-tolerance material. DEFORM-2D FEM software is effective in modeling co-extrusion experiments and can be used to design a process and limit the number of verification experiments needed in a short amount of time.

#### **4.1.7 Conclusions for Use of Finite Element Modeling Analysis for New Billet Design**

Based on the performed numerical and physical experiments the following conclusions have been formulated:

1. The FEM code, DEFORM-2D, is an effective tool for experimental design for hollow cross-sectional co-extrusion products and can minimize the number of validation tests needed. Geometrical results from both FEM extrusion simulations and samples produced at ORNL are in good agreement for tube co-extrusion using two billet materials.
2. Extrudates produced using traditional billet geometry show core thicknesses greater than or equal to the initial core thickness in the billet during the initial part of extrusion. In both the low and high extrusion ratio cases, the ratio of core to sleeve material increases with decreasing core length in the initial billet. This value becomes closer to the ratio in the initial billet. Proportionate flow occurs when the two ratios are equal.
3. Reduction in scrap material (due to out-of-tolerance geometry) can be realized by utilizing the core-shortening method. Shortening the core material length 8 to 20% can be effective in managing sound material flow. Core shortening causes the sleeve material to upset into the recessed region of the billet so that concurrent flow is achieved. Less material is lost to early flow out of the die, thus, steady-state core thickness flow conditions are reached sooner. The actual amount of shortening is governed by the specific processing parameters for the intended extrudate geometry. During steady state material flow, there is little or no difference in core material distribution between extrudates produced from a billet with a full-length or shortened core. Maximum savings can be achieved with the amount of upsetting being in balance with the flow of the core material into the die orifice, which is also influenced by the die angle.
4. Reduction in scrap by new billet design with core-shortening results in energy savings from two aspects: (1) energy used in billet heating and extrusion process and (2) energy used in replacing the materials for remaking extrusion billets.

#### **4.2 Analysis of Eccentricity in Bimetallic Extruded Tubes**

A new billet design that utilizes a shorted core length has been identified as a method to control the early stage/breakthrough flow of the material (Sect. 4.1). By having a recessed core, concurrent flow occurs by slowing the core material’s approach to the die orifice as the sleeve material must upset to fill the gap. By properly balancing the amount of recessed material in reference to initial thickness as well as extrusion ratio/die orifice diameter, concurrent material flow is promoted earlier. Because of the additional radial flow that is caused by the recessed core during early stages and breakthrough of

extrusion, the effect on the tube eccentricity must be addressed. This section deals with measuring the wall thickness of co-extruded tubes along the tube length and comparing the observed product with the values of eccentricity.

The extruded tubes used in this project were composed of a stainless steel (UNS S30400, referred to as 304) core and a plain carbon steel sleeve (UNSG10211, referred to as 1020). Testing was performed on multiple billet geometries in reference to initial core and sleeve thicknesses. The extrusion ratio,  $R$ , was equal to 10.6 for the results presented here (a subset of a larger experimental matrix). Table 4.4 outlines the geometry of the billets tested before extrusion.

#### 4.2.1 Eccentricity Measurements

The eccentricity measurements were made on the bimetallic tube produced from a billet design given in Table 4.4. For each billet set—identified by the thickness of the stainless steel core material (i.e., Low or High)—there were three billets: one with a full-length core (designated by the numeral “1” after the core description), one with the core shortened 10% of the overall billet length (designated by the numeral “2” after the core description), and one with the core shortened 20% (designated by the numeral “3” after the core description). The center-hole diameter was 38.1 mm, overall billet length was 127 mm, and the overall billet diameter was 137.2 mm.

**Table 4.4. Billet geometry identification for eccentricity measurements**

| Sample ID | Core thickness (mm) | Sleeve thickness (mm) | Core length (mm) | Core length (% of billet) |
|-----------|---------------------|-----------------------|------------------|---------------------------|
| HighCore1 | 8.9                 | 40.6                  | 127.0            | 100                       |
| HighCore2 | 8.9                 | 40.6                  | 114.3            | 90                        |
| HighCore3 | 8.9                 | 40.6                  | 101.6            | 80                        |
|           |                     |                       |                  |                           |
| LowCore1  | 6.4                 | 43.2                  | 127.0            | 100                       |
| LowCore2  | 6.4                 | 43.2                  | 114.3            | 90                        |
| LowCore3  | 6.4                 | 43.2                  | 101.6            | 80                        |

Each billet set in Table 4.4 was preheated at 1200°C for approximately 2.5 h in a box furnace with a nitrogen atmosphere. The billets were lubricated with a graphite-based lubricant and extruded with a mandrel attached to the dummy block on a horizontal hydraulic press of 1200-ton capacity. A graphite pad (preheated with the billet) was placed between the dummy block and the billet so that the entire billet could be extruded. This graphite pad deforms during extrusion and forces the entire billet through the die so that no billet material is left in the container at the end of extrusion. The die orifice diameter was 55.6 mm.

After extrusion, the tubes were cut into 50.8-mm-thick slices, with one side prepared for optical measurements. Core and sleeve thicknesses were measured at four positions for each slice (12, 3, 6, and 9 o’clock also referred to as North, East, South, and West, respectively) as shown in Fig. 4.32.

Prior to sectioning the tube, a reference groove was cut into the tube along the length so that the four measurement positions were constant throughout the tube. Measurements were made using a macro camera interfaced with a Leco 3001A Image Analysis software package.

Two assumptions were made so that the eccentricity could be calculated: the ID was constant and equal to mandrel diameter (35.6 mm) and the outer diameter (OD) was constant, which was determined by die orifice (55.6 mm).

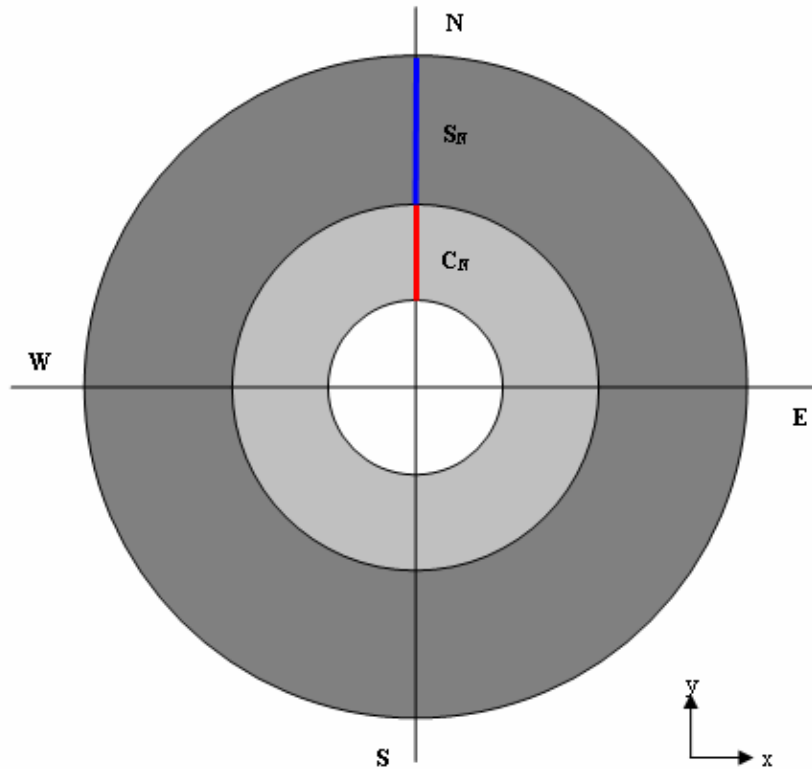


**Fig. 4.32. Schematic representation of the cross section of a co-extruded tube showing orientation definitions and sleeve and core thickness designations.**

Eccentricity was calculated by summing the core and sleeve thickness for each position and comparing that value to the nominal value, given the assumed ID and OD for the tube. This was calculated for each slice of the extrudate; however, it should be noted that the last ~75 to 100 mm of the extrudate were discarded and not measured due to a funnel back-end defect that results from using the graphite pad for extrusion. Since a graphite pad is placed between the extrudate and the dummy block during extrusion, the entire billet is extruded, and a conical void is formed in the rear by the deforming graphite pad that acts to push the entire billet through the die orifice.

For each extrudate, the wall thickness eccentricity was measured for each slice, as well as the absolute value of maximum error and its location, as well as the average error. These results are presented in Table 4.5. Additionally, the error was plotted for the entire extrudate as a function of extrudate length, as shown in Figs. 4.33 through 4.38. The maximum deviation covers a significant range from 11 to 40%. For the majority of the cases, the maximum deviation occurs in the front end of the extrudate. The average value of percentage error is generally near 5% for the majority of cases, with one anomalous value corresponding to the High Core2 sample, as shown in Fig. 4.34. The large error is a result of the funnel-shaped back end defect that was captured in the back-end of the extrudate.



**Table 4.5. Percentage of the absolute maximum error in wall thickness from nominal for extrudates, along with location and average error and deviation for the entire tube**

| Sample    | Absolute max error (%) | Location–fraction of extrudate length | Average % error $\pm$ deviation |
|-----------|------------------------|---------------------------------------|---------------------------------|
| HighCore1 | 30.9                   | 0.059                                 | 6.17 $\pm$ 6.9                  |
| HighCore2 | 41.4                   | 0.071                                 | 10.51 $\pm$ 8.8                 |
| HighCore3 | 10.0                   | 0.78                                  | 4.32 $\pm$ 2.5                  |
| LowCore1  | 11.3                   | 0.056                                 | 4.43 $\pm$ 3.0                  |
| LowCore2  | 13.7                   | 0.94                                  | 4.02 $\pm$ 3.1                  |
| LowCore3  | 19.3                   | 0.059                                 | 5.51 $\pm$ 4.0                  |

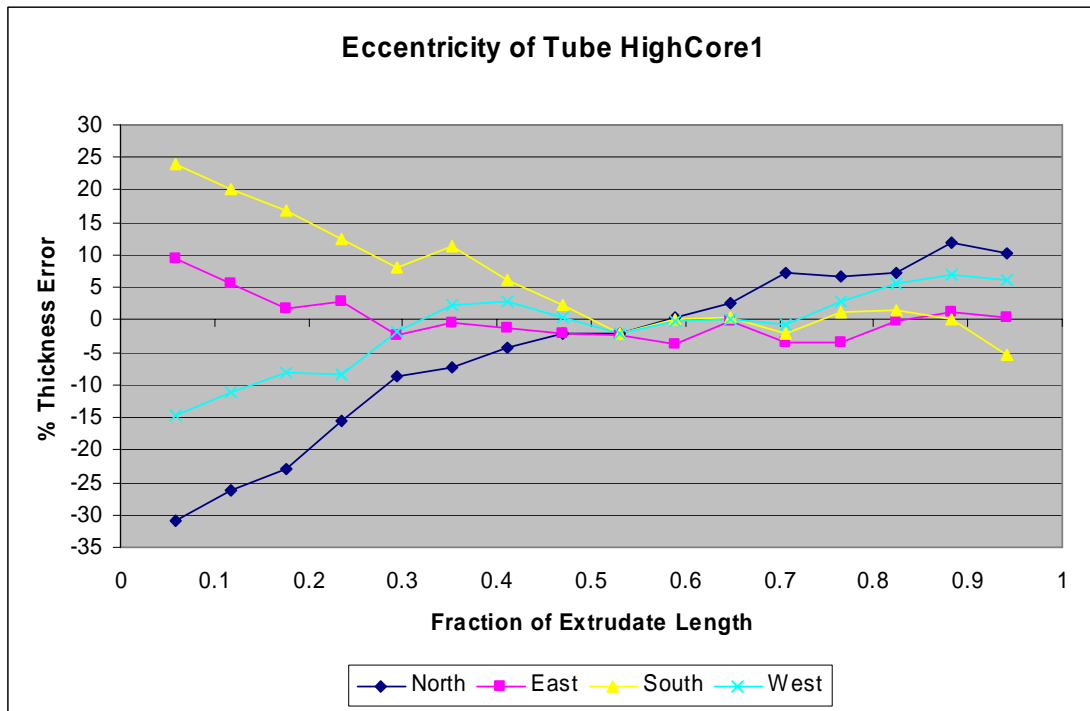


**Fig. 4.33. Eccentricity of tube HighCore1 (extrusion ratio of 3.3, full-length core); percentage of error in wall thickness versus fraction of extrudate length.**

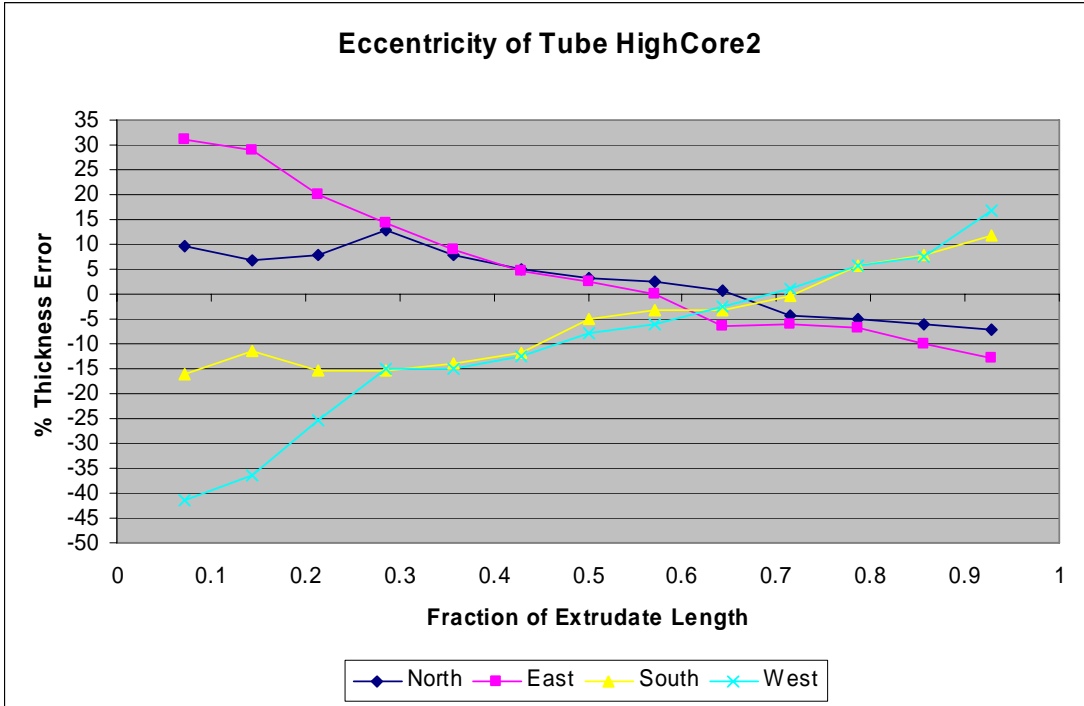


Fig. 4.34. Eccentricity of tube HighCore2 (extrusion ratio of 3.3, 90% length core); percentage of error in wall thickness versus fraction of extrudate length.

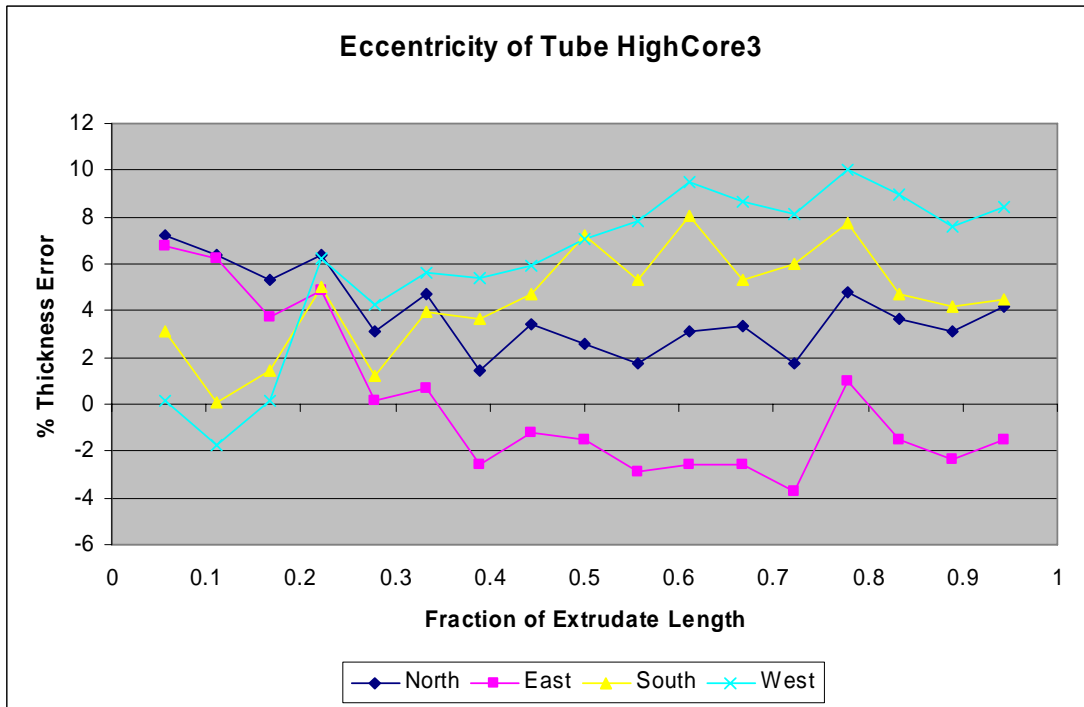


Fig. 4.35. Eccentricity of tube HighCore3 (extrusion ratio of 3.3, 80% length core); percentage of error in wall thickness versus fraction of extrudate length.

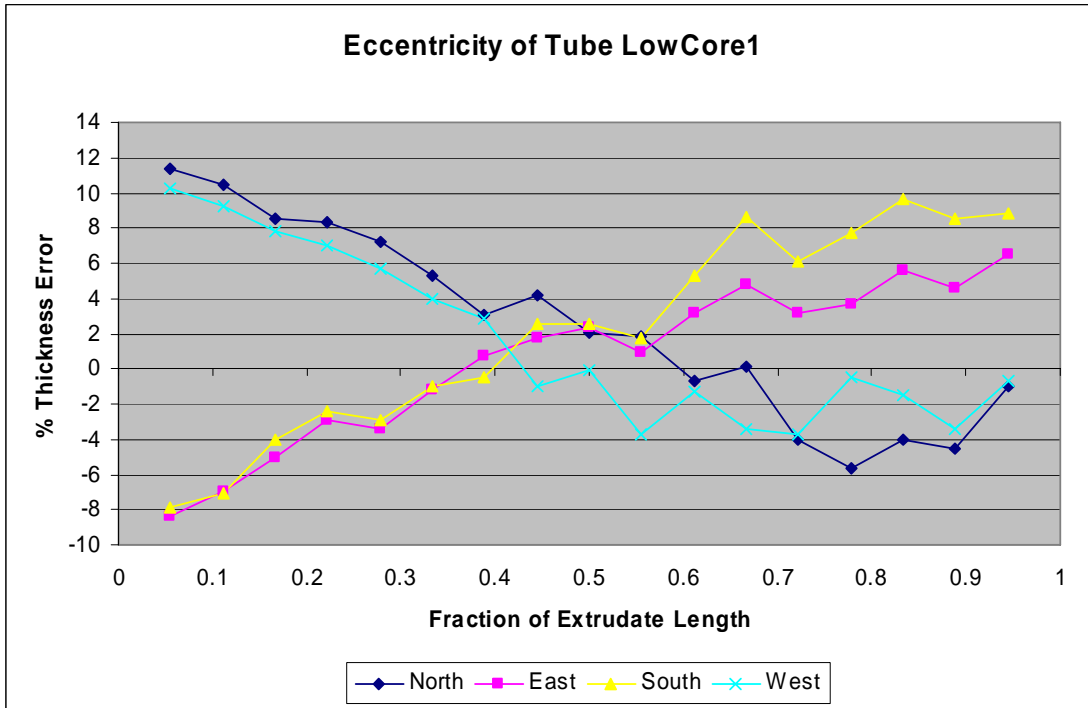


Fig. 4.36. Eccentricity of tube LowCore1 (extrusion ratio of 10.6, full-length core); percentage of error in wall thickness versus fraction of extrudate length.

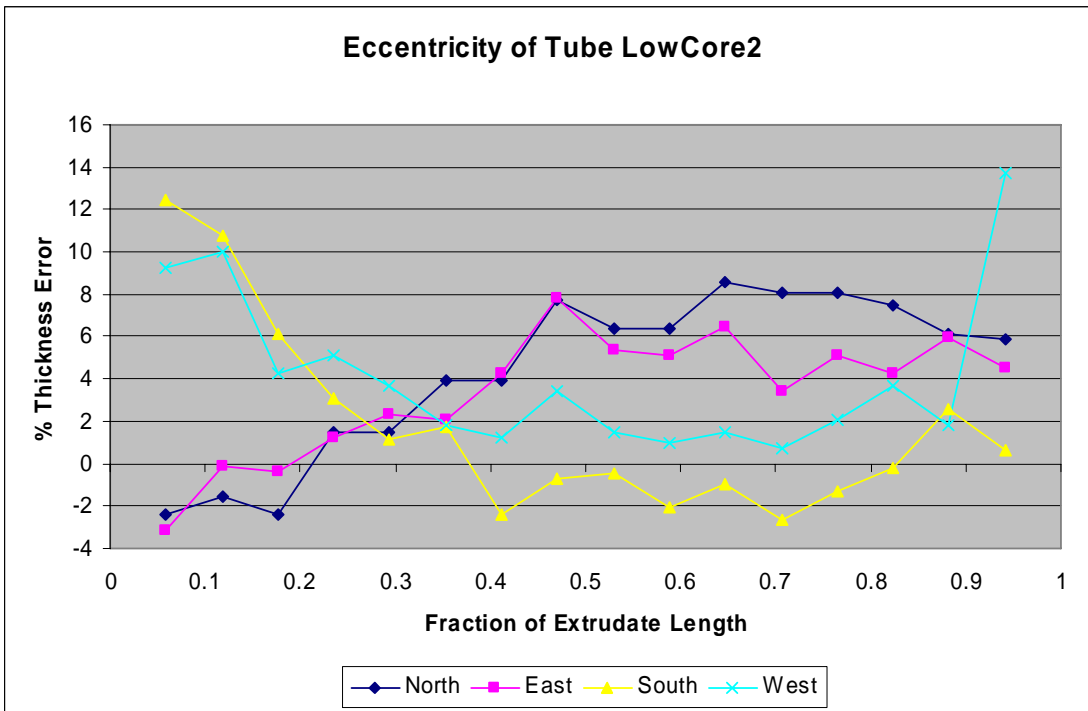


Fig. 4.37. Eccentricity of tube LowCore2 (extrusion ratio of 10.6, 90% length core); percentage of error in wall thickness versus fraction of extrudate length.

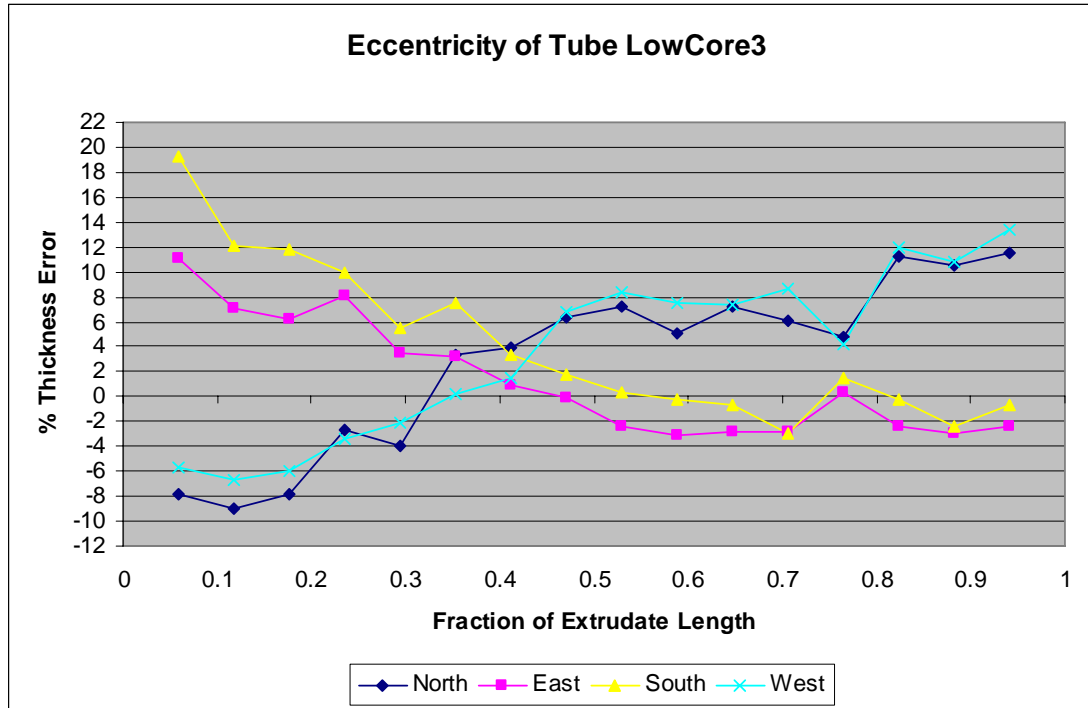


Fig. 4.38. Eccentricity of tube LowCore3 (extrusion ratio of 10.6, 80% length core); percentage of error in wall thickness versus fraction of extrudate length.

#### 4.2.2 Discussion of Eccentricity Observations

As shown in Table 4.5, the maximum eccentricity occurs within the first 10% of the extrudate for the majority of the cases. This corresponds to the region of the extrudate that occurs before the onset of steady state extrusion. In single-material extrusion, very often the nose of the extrudate shows signs of torturous material flow that can be characterized as eccentricity.<sup>1</sup> This condition is exaggerated when multiple materials are extruded concurrently, especially with the shortened core geometry. The sleeve material must upset into the region where the core material is not present; this occurs as the billet upsets into the container. If the extrusion chamber is not fully filled prior to material flow through the die orifice, eccentricity may be significantly increased. For the cases where the maximum eccentricity was not located in the nose of the extrudate, the maximum occur in the last 25% of the extrudate. This is approaching the region where the deforming graphite pad may act to cause exaggerated eccentricity as it forms the conical back-end defect.

As can be seen in Figs. 4.33. through 4.38, there are several trends worth noting.

1. As expected, corresponding orientations (i.e., East and West, North and South) show opposite sign errors.
2. Negative error values correspond to regions of the extrudate where the wall thickness was greater than the nominal, and positive error values correspond to regions where the wall thickness was less than the nominal.
3. During progression of extrusion, which can be noted by an increasing fraction of extrudate length, the trend is for the wall thickness to approach the nominal value, and then switch the sign of the error value.
4. Approximately midway through extrusion, the four measurements reach a minima in error value, and this corresponds to the steady state region. For extrudates of a greater length (i.e., a higher

extrusion ratio), it is believed that the region corresponding to the lowest error/steady state material flow will be greater. In the case of short extruded billets that use a relatively low extrusion ratio (10.6), there is not enough time for the material to reach optimal flow. Typical extrusion ratios for ferrous products are closer to 20–25 value.<sup>1</sup>

Regardless of the core length for a given billet geometry, the maximum absolute wall thickness error is within a standard deviation for the set of extrudates (Table 4.5). This shows that the core-shortening method, which has been shown in Section 4.1 to properly manage material flow during the co-extrusion process does not negatively affect eccentricity. Eccentricity that occurs near the end of the extrudate is a result of extrusion with a graphite pad and will not be present in traditional extrusion processing where a portion of the billet remains un-extruded in the press chamber. As the pad deforms and ultimately fails, it causes a cone- or funnel-shaped defect. Heterogeneous deformation occurs at the ID of the tube, and wall thickness is not constant. This region must be discarded in practice. The funnel defect may also form in extrusion using only a dummy block, but is caused by a non-continuous metal flow velocity flow. When extruding with only a dummy block, a portion of the billet remains un-extruded in the press chamber and is discarded.

Additional sources contribute to eccentricity in the extrusion of tubes that have not been addressed here. Temperature gradients that develop in the billet prior to and during extrusion play an extremely significant role in eccentricity. As a result of a temperature gradient, there is a flow stress gradient that leads to non-homogeneous material flow. Extrusion press variables, such as alignment, also influence eccentricity; however, since all of the extrudates analyzed in this work were produced using the same press and same tooling, and tooling wear is considered negligible, and the effect of these variables is not considered.

Use of the core-shortening method does not significantly influence eccentricity in the extruded product. The highest amount of eccentricity occurs during the non-steady state portion of extrusion, which occurs at either the front or back end of the extrudate. Values of eccentricity calculated for full-length core and shortened-core billets are comparable.

#### **4.2.3 Conclusions from Eccentricity Analysis of Bimetallic Tubes**

1. The maximum eccentricity in reference to wall thickness in co-extruded ferrous tubes generally occurs within the first 10% of the extrudate or at the end of the extrudate (in this case, as a result of extrusion using a deforming graphite pad).
2. The core-shortening method does not negatively affect wall thickness eccentricity, even in the case where the initial core length in the billet is recessed 20%. Eccentricity results were similar regardless of core length in the initial billet except for a few cases where the back-end defect affected eccentricity.

#### **4.3 Metallurgical Interface Development as a Result of Co-extrusion of Ferrous Material Tubes**

The interface between the co-extruded materials is of the most importance because it is the most likely region for failure to occur and will exhibit the most complex microstructure. In the case of two materials joined via co-extrusion, failure may occur at the exact interface, or in either of the two materials in the region adjacent to the new bond TMAZ. The failure is a result of the interaction between the materials and their chemistry and the microstructure that developed as a result of processing.

The goal of this part of the research was to understand the development of the TMAZ in a model system of 304 stainless steel and 1020 plain carbon steel co-extrusion and to successfully model the process on a laboratory scale. The development of a modeling procedure allows for investigation and design of processing parameters for future alloy combinations without the need to produce an actual test-extrudate, which can be costly in terms of materials, labor, and press down time.

#### 4.3.1 Compositions of Steels Used and Their Possible Effects on Interface

In this investigation, plain carbon steel and austenitic stainless steel were co-extruded into bimetallic tubes as described in Section 4.1. Chemical analysis of the two steels is shown in Table 4.6.

The major difference between the stainless steel and plain carbon steel alloys are the elements C, Cr, Mn, and Ni. Plain carbon steel has a much higher amount of C (Table 4.6) and no or lower amounts of Cr, Mn, and Ni than stainless steel. It is expected that carbon will diffuse from the 1020 steel into the stainless steel, and Cr, Mn, and Ni will diffuse from the 304 into the 1020 steel.

**Table 4.6. Chemical analysis in weight percent of the steels used for this project using the arc-spark spectroscopy method**

| Alloy | C    | Cr    | Mn   | Ni   | P     | S     | Si   | Fe      |
|-------|------|-------|------|------|-------|-------|------|---------|
| 1020  | 0.19 | -     | 0.71 | -    | 0.009 | 0.050 | -    | Balance |
| 304   | 0.02 | 18.27 | 1.13 | 9.32 | 0.028 | 0.025 | 0.41 | Balance |

Bonding between austenitic stainless steels and plain carbon steels has been extensively investigated for applications produced using fusion welding.<sup>2,4</sup> Commonly, two deleterious microstructures will form in the HAZ upon cooling to room temperature. In dissimilar welds involving austenitic stainless steels and carbon steels with appreciable levels of carbon, chromium carbides may form in the stainless steel. These carbides typically form on grain boundaries and result in a region denuded of chromium directly adjacent to the precipitates. This structure is known as a sensitized microstructure or as weld decay and is susceptible to degraded corrosion resistance. Intergranular corrosion occurs, leading to undesirable corrosion performance.<sup>26</sup>

The second deleterious microstructure that may form is a region of martensite. Different alloying elements influence the martensite start temperature. A potency coefficient is assigned to the various elements, in this case C, Mn, Ni, Cr, and Mo. Equation 1 shows<sup>29</sup> the effect of various elements on the martensite start temperature ( $M_s$ ) developed for martensitic stainless steels and was shown to be accurate for determining martensite layer thicknesses in dissimilar austenitic/ferritic steel welds.<sup>30</sup>

$$M_s(^{\circ}\text{C}) = 540 - 497C - 6.3\text{Mn} - 36.3\text{Ni} - 10.8\text{Cr} - 46.6\text{Mo} \quad , \quad (2)$$

where C, Mn, Ni, Cr, and Mo represent the concentration of these elements in weigh percent. For martensite to form, a critical cooling rate must be reached so that the other microstructural phases (ferrite, cementite, bainite) will not form.

#### 4.3.2 Experimental Details for Interface Study

Table 4.7 lists the geometry of the initial billet and the extrusion ratio for the co-extruded tube used for detailed interface study. As shown in this table, low- and high-extrusion ratios of R equal to 3.3 and 10.6, respectively, were investigated with the initial billet geometries being the same.

**Table 4.7. Extrudate sample information for the geometry of the initial billet**

| Sample ID | 304—Core thickness (mm) | 1020—Sleeve thickness (mm) | Extrusion ratio | Preheat temp. (°C)/time (h) | FEM calculated strain | FEM calculated strain rate |
|-----------|-------------------------|----------------------------|-----------------|-----------------------------|-----------------------|----------------------------|
| Low R     | 11.4                    | 38.1                       | 3.3             | 1100/2                      | 1.2                   | 2.1 s <sup>-1</sup>        |
| High R    | 11.4                    | 38.1                       | 10.6            | 1200/2.5                    | 2.9                   | 22.0 s <sup>-1</sup>       |

To model the microstructural changes as a result of the preheat treatment of the as-assembled billet, a 7-mm-thick slice was cut from the billet. It is important to note that the stresses from shrink fitting during assembly held the core material within the sleeve material. The material was wrapped in stainless steel foil to prevent/minimize decarburization to the atmosphere and placed in a furnace at 1200°C for 2.5 h in a nitrogen environment. Only the high extrusion ratio preheat schedule was simulated in the laboratory environment. After being removed from the furnace, the sample was allowed to air-cool to room temperature. Note: no excessive oxidation or decarburization to the environment was observed. The preheat treatment was also modeled on the Gleeble thermomechanical simulator at the same time and temperature of the extrusion process.

Samples were cut from the extrudate and from the preheat test slice as well as from the stock billet material and prepared using standard metallographic grinding and polishing techniques. The final polishing step was 30 to 60 min on a vibratory polishing unit using MasterPrep. Both transverse and longitudinal samples were prepared. In an effort to determine the different precipitates and transformation products in the vicinity of the bond between the co-extruded materials, a multistep etching procedure was used. After polishing, the sample was etched in Murakami's reagent (10g K<sub>3</sub>Fe(CN)<sub>6</sub>, 10g KOH, and 100 mL H<sub>2</sub>O) for approximately four minutes. When used at room temperature, the etch attacks chromium carbides while cementite (Fe<sub>3</sub>C) is not affected.<sup>31</sup> A microhardness indent is used to mark regions of interest for photomicrographs and electron microprobe analysis (EMPA). The second etching step was performed using a mixture of equal parts HCl, HNO<sub>3</sub> and distilled H<sub>2</sub>O. The sample was placed on its side and etched for 30 to 45 s in the solution that was agitated using a magnetic stirring bar to reveal the Fe<sub>3</sub>C, ferrite, and austenite grain boundaries. Photomicrographs can then be obtained from the same regions as before by using the microhardness indents for orientation.

Measurements of the decarburized layer thickness and the carbide-precipitated layer thickness were made on the etched extruded samples using a Leco 3001A image analysis system.

### 4.3.3 Finite Element Modeling

FEM was performed using DEFORM-2D software version 8.1. To simulate the performed experiments, an isothermal simulation was run with the material temperature at either 1100 or 1200°C, corresponding with the actual extrusion experiments. The core was modeled using a mesh with 2000 elements and the sleeve using a mesh of 1500 elements. Since the simulation was axisymmetric, only one-half of the billet and process was simulated. Friction was defined as shear equal to 0.3 between all billet surfaces (regardless of material) and the die, container, and mandrel. Between the core and sleeve, material friction was set as shear equal to 0.7, with sticking friction at the end nodes on both the front and back of the billet between the two materials (to simulate the welds on the billet). The die and container were modeled as one object. The flow stress data for 1025 plain carbon steel is included with the software database and was used to simulate the 1020 steel. The 1020 and 1025 plain carbon steels exhibit similar flow stress and extrusion characteristics at the simulation temperature.

Maximum effective strain and strain rate experienced by the material was determined from the FEM simulations for the regions of microstructure examined after extrusion. This was performed by determining the position of the material in the un-extruded billet in reference to its final position in the extrudate using point tracking in the FEM simulation. Two points were measured for each simulation—one starting on the interface between the stainless and plain carbon steel, and one at the mid-thickness of the core material (stainless steel), which was 5.7 mm from the plain carbon steel surface. For the low-extrusion ratio sample, the maximum strain and strain rates were 1.2 and  $2.0 \text{ s}^{-1}$ , respectively (Figs. 4.39 and 4.40). For the high-extrusion ratio sample, the maximum strain and strain rates were 2.9 and  $22.0 \text{ s}^{-1}$ , respectively (Figs. 4.41 and 4.42).

#### 4.3.4 Gleeble Simulation of Extrusion Process

Samples of the two materials were machined into 6-mm-thick by 10-mm-diam cylinders. The materials were butted together at a force of 445 N, held at the preheat temperature for the extrusion ratio conditions for the corresponding time, and deformed at the corresponding extrusion temperature using a Gleeble Hydrowedge system. The grips were displaced a total of 11.3 mm, and the final sample height was 0.7 mm for the high extrusion ratio Gleeble simulation; the grip displacement and final sample height were 8.4 mm and 3.6 mm for the low extrusion ratio simulation. The samples were allowed to air cool to room temperature while still in the grips. Additionally, the low extrusion ratio simulation sample was placed back into a box furnace at  $1100^\circ\text{C}$  and allowed to furnace cool to  $200^\circ\text{C}$  (time versus temperature shown in Fig. 4.43) and then was air cooled to room temperature. Samples from the Gleeble simulations were sectioned and prepared in a similar manner to the tubes produced from extrusions carried out at ORNL.

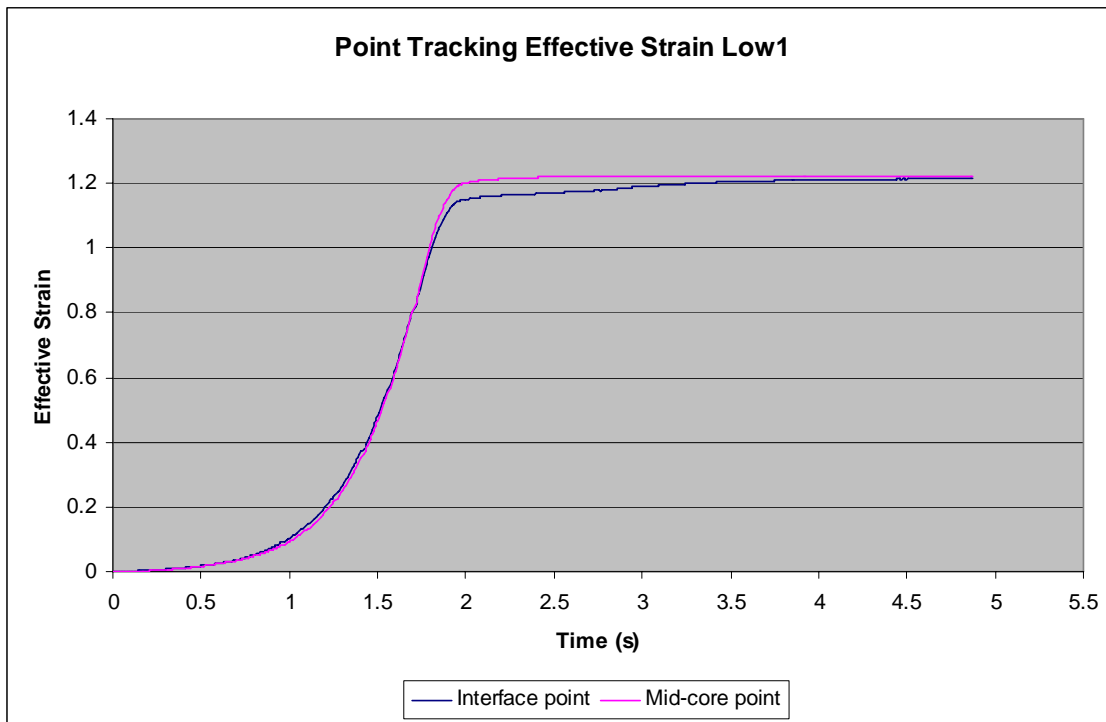


Fig. 4.39. Effective strain measurement from point tracking in finite element modeling of the Low1 sample (total time).



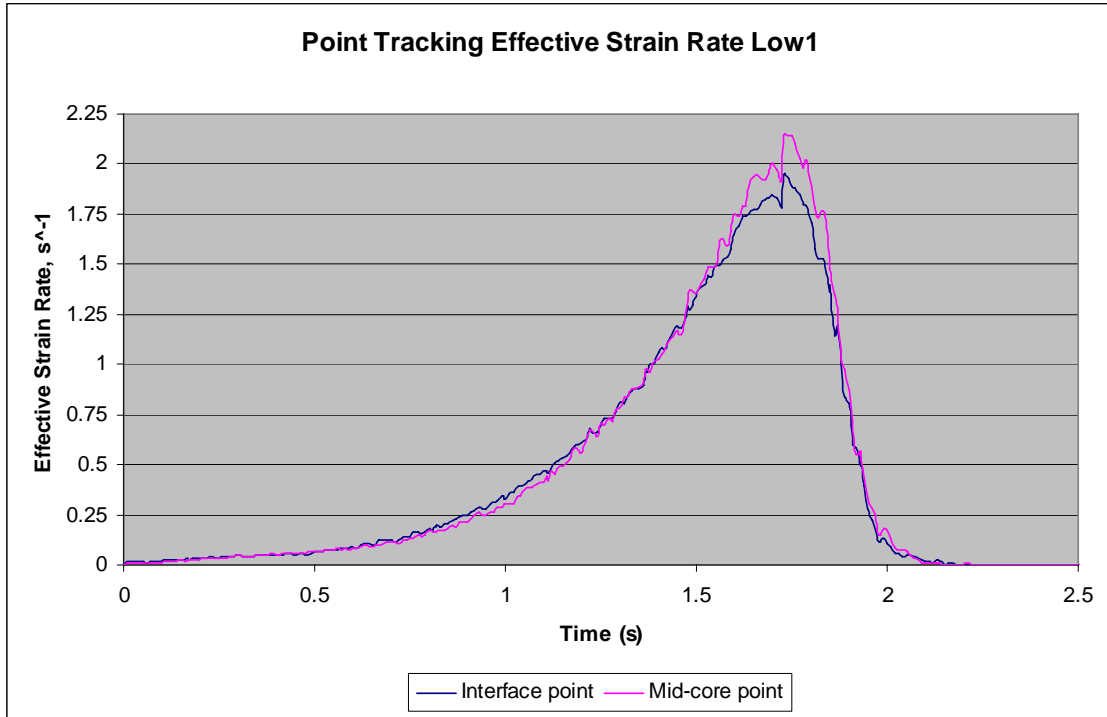


Fig. 4.40. Effective strain rate measurement from point tracking in finite element modeling of the Low1 sample (expanded view).

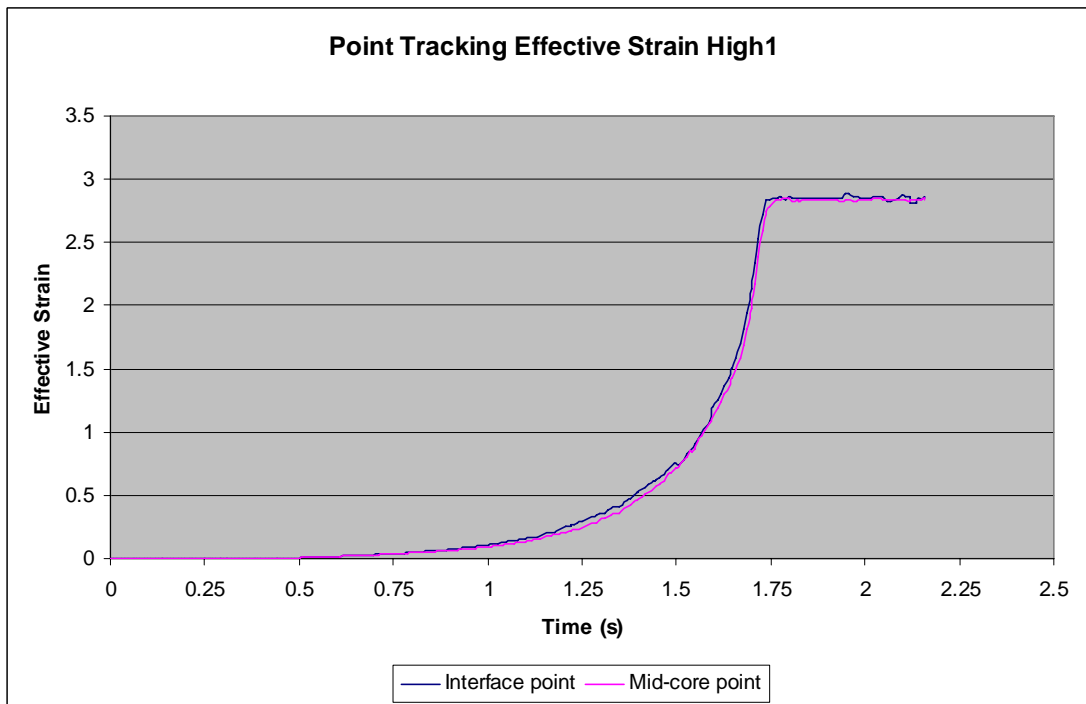


Fig. 4.41. Effective strain measurement from point tracking in finite element modeling of the High1 sample (total time).

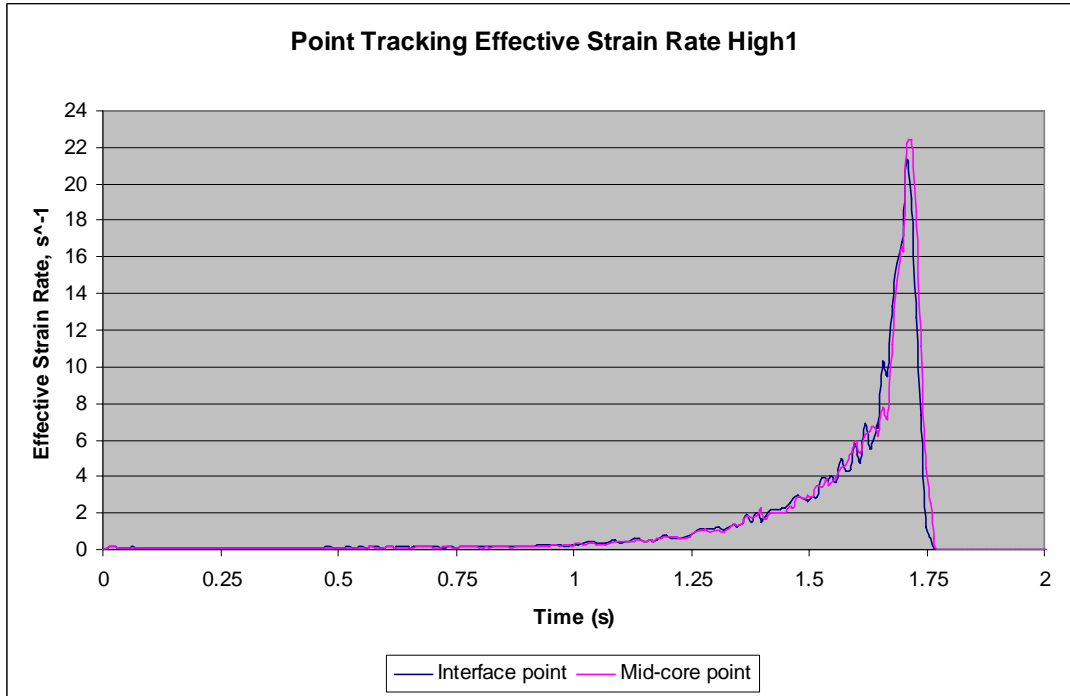


Fig. 4.42. Effective strain rate measurement from point tracking in finite element modeling of the High1 sample (expanded view).

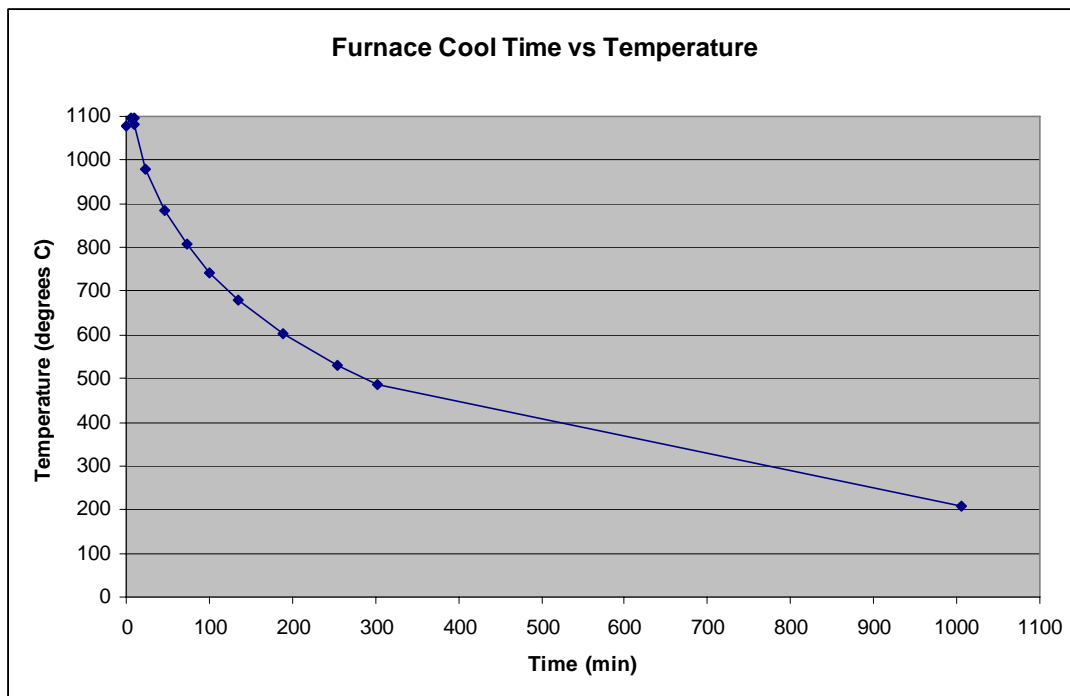


Fig. 4.43. Low strain/strain rate Gleeble sample furnace cool time versus temperature profile.

Electron microprobe analysis was performed at 20 keV using a JEOL 733 electron microprobe with an Advanced Microbeam Control system. Mapping of the interface was performed using electron dispersive spectrum (EDS) for Cr, Ni, and Fe, while wavelength dispersive spectroscopy (WDS) was used to map C with 0.15 s dwell per spot. Quantitative line scans (ZAF corrected) were produced at 2- $\mu\text{m}$  steps. The LiF crystals were used for Cr, Ni, Fe, and Mn while a LDEII crystal was used for C. For each element, the on-peak time was 40 s, while the off-peak times were 20 s. Samples from the Gleeble and industrial experiments were used for orientation imaging microscopy characterization. EBSD was performed using an EDAX/TSL Digiview Camera interfaced with a Philips XL-30 Environmental scanning electron microscopy (SEM).

#### 4.3.5 Microstructural Analysis

Effective strain and strain rate from the point tracking in FEM for the two extrusion ratios are shown in Figs. 4.39 through 4.42. Values of strain and strain rate used for the Gleeble simulation were the maximum that the material was subjected to during extrusion. Once the material passed through the die orifice, the strain or strain rate did not increase.

The microstructure of the stock 1020 plain carbon sleeve material can be observed in Fig. 4.44. The material exhibits banded pearlite/ferrite microstructure, which is typical of extruded or rolled materials. The microstructure of the stock 304 stainless steel consists of equiaxed austenite grains with delta ferrite stringers (Fig. 4.45).

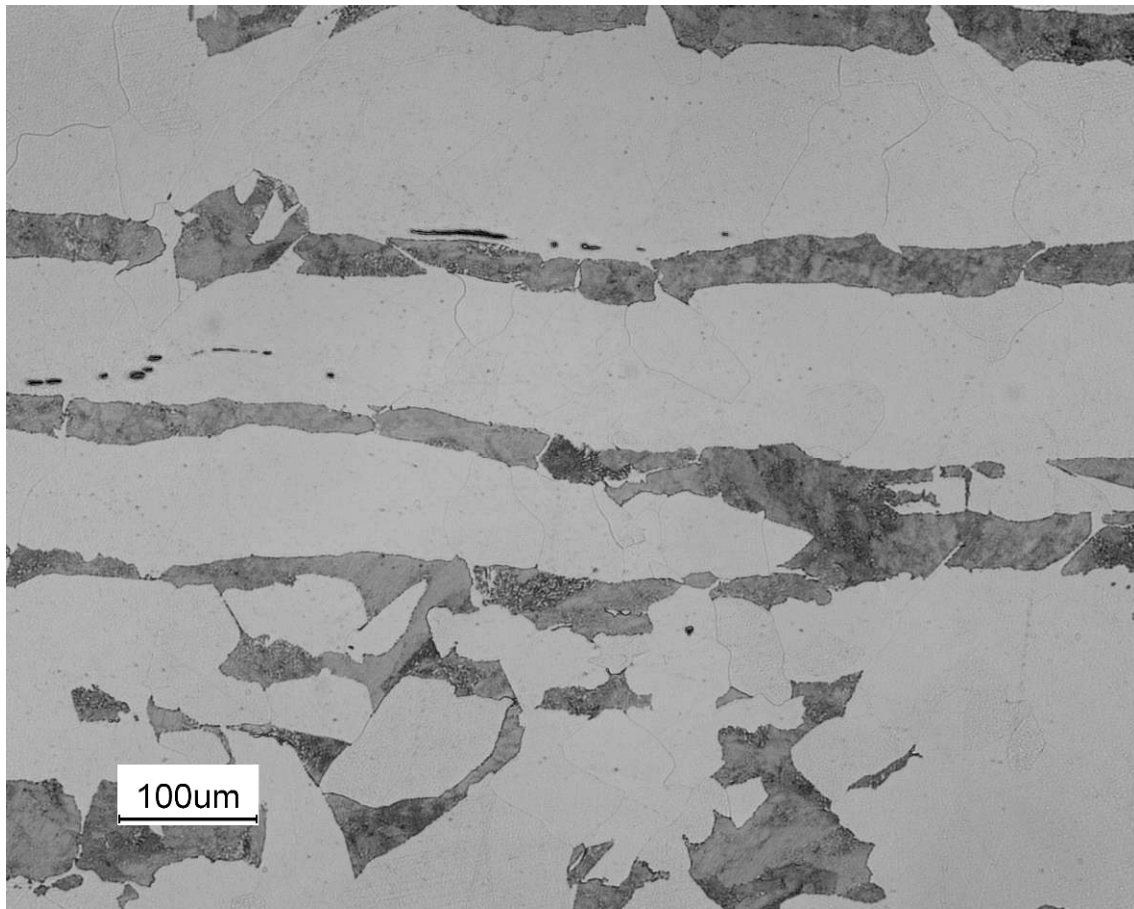
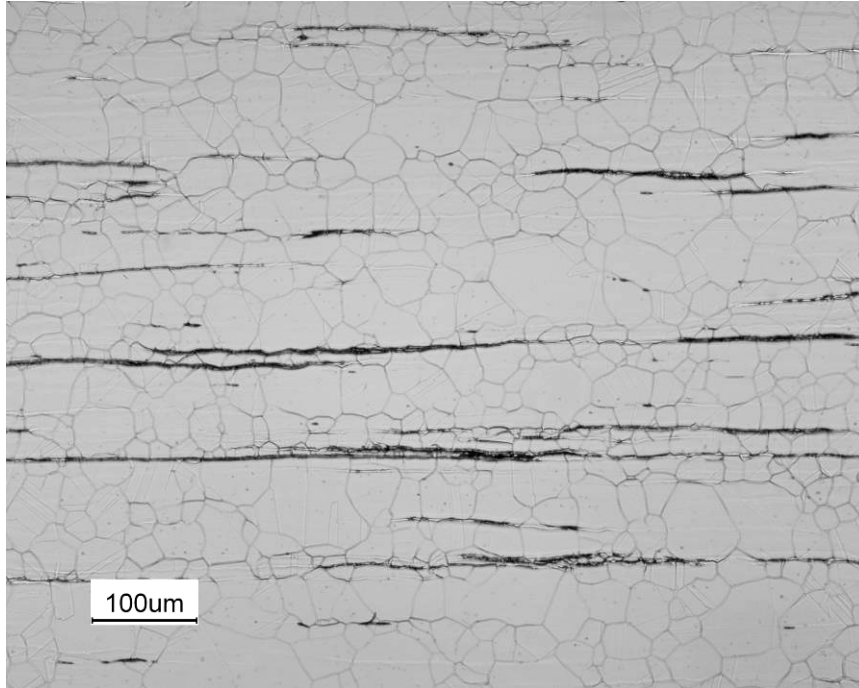
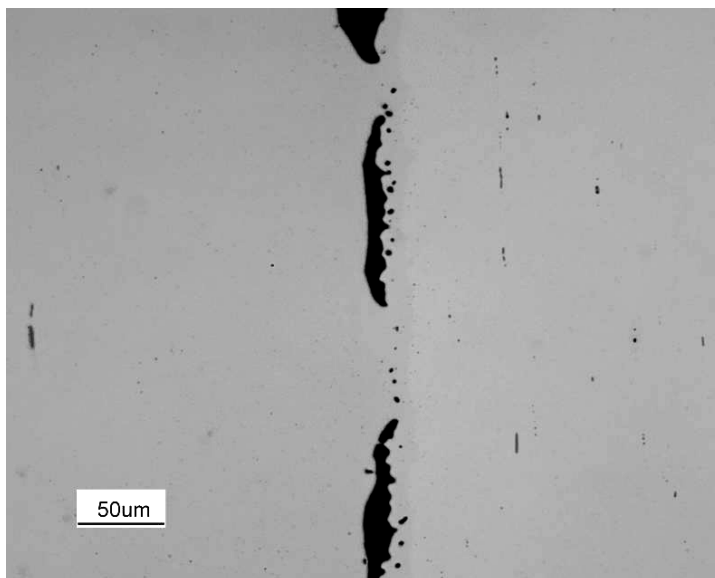


Fig. 4.44. Banded pearlite in a longitudinal section of 1020 plain carbon steel stock material prior to processing: etched using 4% picral for 25 s.



**Fig. 4.45. Equiaxed austenite and delta ferrite in longitudinal section of stock 304 stainless steel material: electrolytically etched using 60% HNO<sub>3</sub>/40% H<sub>2</sub>O at 3V for 6 s.**

Figure 4.46 shows the interface development between the two steel alloys as a result of the preheat treatment of 2.5 h at 1200°C, as simulated using a box furnace. The photomicrograph is of the as-polished specimen and shows characteristic diffusional bond morphology. The asperities have grown into bridges, leaving isolated, rounded pores at the bond. A comparable schematic of the stages of diffusion bonding is shown in Fig. 4.47.<sup>26</sup> After the preheat treatment, the material is transitioning from stage a to stage b (Fig. 4.47). Figure 4.48 shows the etched interface and microstructure after



**Fig. 4.46. Interface between (left) 1020 steel and (right) 304 stainless steel after 2.5 h at 1200°C: unetched.**

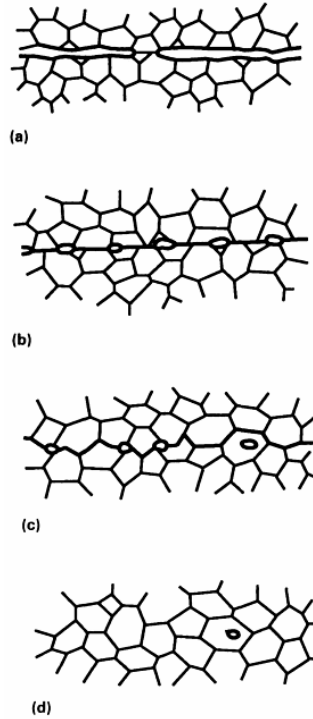


**Fig. 4.47. Development stages in diffusional bonding/ solid state welding.** (a) Initial contact—limited to a few asperities (room temperature), (b) first stage—deformation of surface asperities by plastic flow and creep, (c) second stage—grain boundary diffusion of atoms to the voids and grain boundary migration, and (d) third stage—volume diffusion of atoms to the voids (*Source*: "Coextrusion Welding," *ASM Handbook*, Vol. 6: Welding, Brazing, and Soldering, ASM International, USA, 1993).

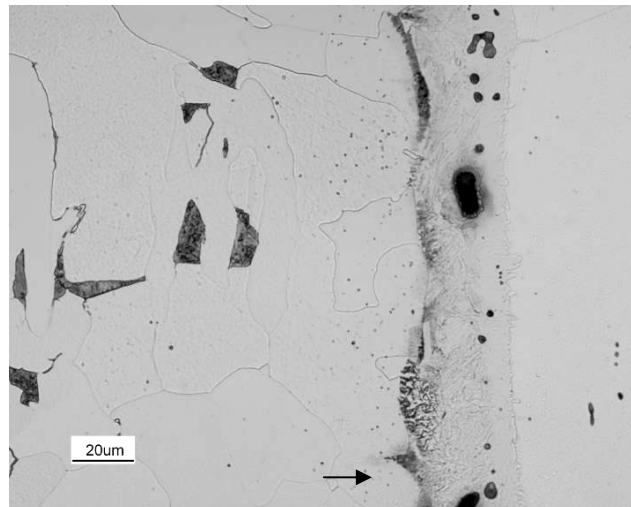
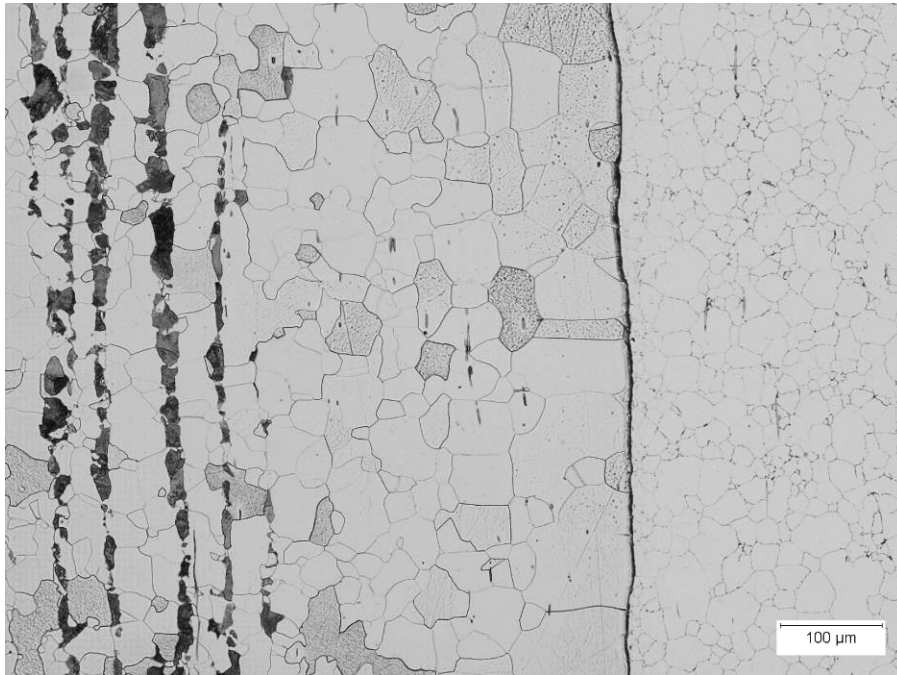


**Fig. 4.48. Interface between (left) 1020 steel and (right) 304 stainless steel cut from the shrink-fit billet after 2.5 h at 1200°C.** The sample was etched with agitated 60 mL HCl, 60 mL HNO<sub>3</sub>, and 60 mL distilled H<sub>2</sub>O for 30 s.

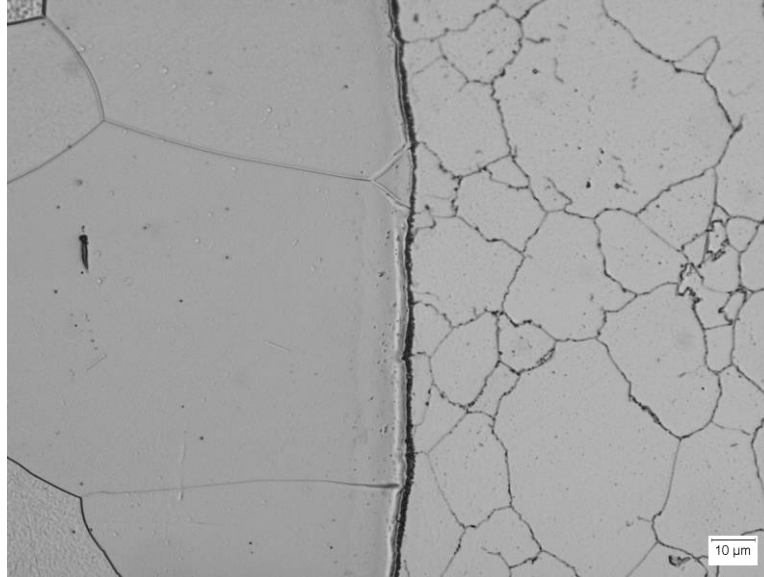
preheat. The plain carbon steel side shows ferrite and islands of pearlite in the bulk of the material. At the interface, a change of contrast can be observed in the material. A layer of pearlite is visible on the plain carbon side of the interface and is denoted by the arrow. No carbides or sensitized structure is revealed in the stainless steel side after etching. After deformation and cooling, carbides were observable on grain boundaries and grain interiors when etched (Fig. 4.49).

Figure 4.49 shows the microstructure of the low extrusion ratio extrudate. The plain carbon steel exhibits banded pearlite in the bulk of the material. This is common to many extruded and rolled plain carbon materials that were also present in the stock material. The plain carbon steel also exhibits a decarburized layer with large ferrite grains adjacent to the bond. The stainless steel exhibits profuse chromium carbide precipitation on the grain boundaries in the vicinity of the bond and austenite and annealing twins in the bulk of the material. Grain boundary carbide precipitation is observed readily in the stainless steel in Figs. 4.50 and 4.51.

The actual interface is shown in greater detail in Figs. 4.50 and 4.51. A thin, high-density layer of iron carbides on the order of a few microns thick exists on the bond. Figure 4.52 shows a composite micrograph of the longitudinal view of the as-extruded microstructure of the high extrusion ratio extrudate. It is important to note that this microstructure is similar to the low extrusion ratio extrudate and is the characteristic microstructure regardless of the extrusion ratio. The thickness of this decarburized region varies somewhat from sample to sample, the measurement of which can be seen in Fig. 4.53.



**Fig. 4.49. Interface between (left) 1020 steel and (right) 304 stainless steel after 2 h at 1100°C and co-extruded followed by air cool to room temperature.** In the low extrusion ratio sample, effective strain ( $1.2$ ) and strain rate ( $2.1 \text{ s}^{-1}$ ) were calculated using DEFORM. The sample was etched with agitated 60 mL HCl, 60 mL HNO<sub>3</sub>, and 60 mL distilled H<sub>2</sub>O for 30 s.



**Fig. 4.50. Higher magnification of the interface between (left) 1020 steel and (right) 304 stainless steel after 2 h at 1100°C and co-extruded followed by air cool to room temperature.** In the extrusion ratio sample, effective strain (1.2) and strain rate ( $2.1 \text{ s}^{-1}$ ) were calculated using DEFORM. The sample was etched with agitated 60 mL HCl, 60 mL  $\text{HNO}_3$ , and 60 mL distilled  $\text{H}_2\text{O}$  for 30 s.

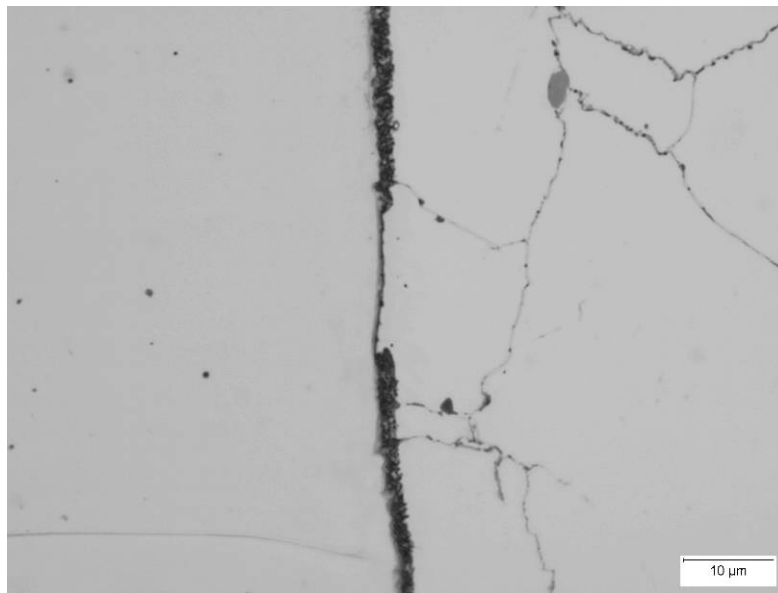


**Fig. 4.51. Higher magnification of the interface between (left) 1020 steel and (right) 304 stainless steel after 2 h at 1100°C and co-extruded followed by air cool to room temperature.** In the low extrusion ratio sample, effective strain (1.2) and strain rate ( $2.1 \text{ s}^{-1}$ ) were calculated using DEFORM. The sample was etched with agitated 60 mL HCl, 60 mL  $\text{HNO}_3$ , and 60 mL distilled  $\text{H}_2\text{O}$  for 30 s.



**Fig. 4.52. Composite micrograph of the regions adjacent to the interface after extrusion with high extrusion ratio.** The effective strain (2.9) and strain rate ( $22 \text{ s}^{-1}$ ) were calculated using DEFORM of (left) 1020 steel and (right) 304 stainless steel. The sample was etched with agitated 60 mL HCl, 60 mL  $\text{HNO}_3$ , and 60 mL distilled  $\text{H}_2\text{O}$  for 30 s.

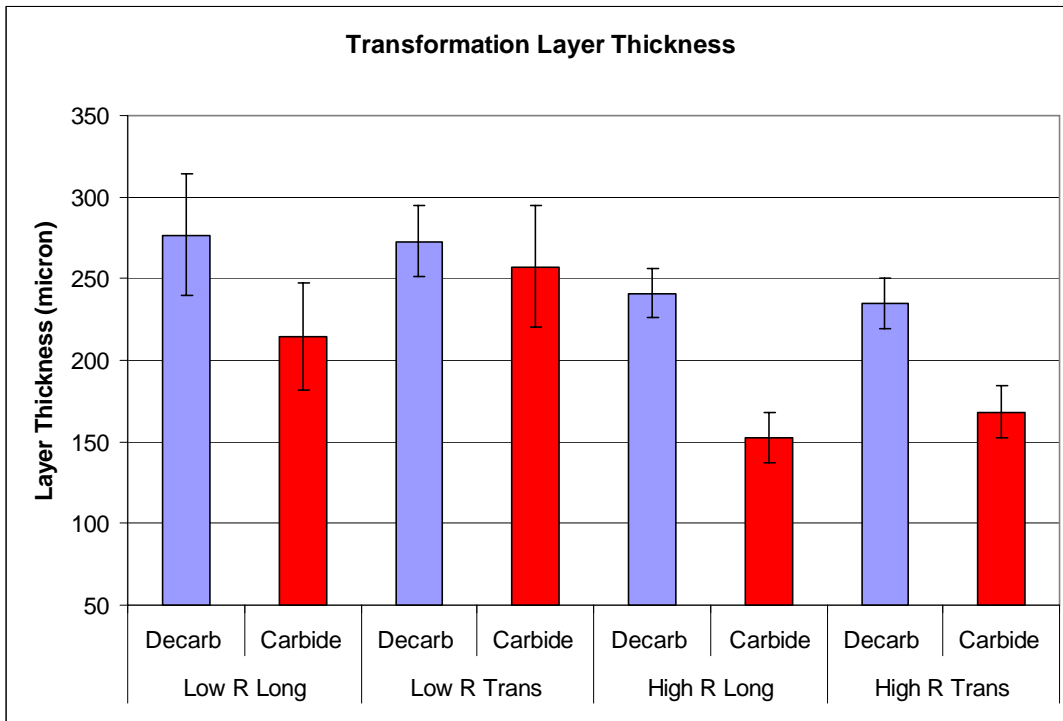


**Fig. 4.53. Transformation layer thickness measurements taken from the etched, extruded samples.** Decarb-decarburized layer, carbide-precipitated carbide layer, long-longitudinal measurements, trans-transverse measurements.

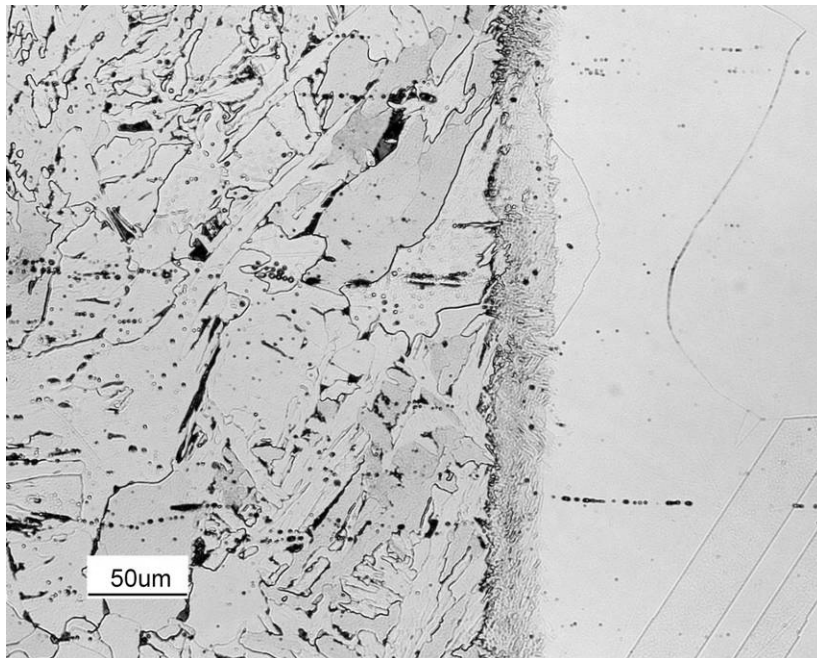
Figure 4.53 shows the transformation layer thickness measurements. For each sample, the decarburized region thickness is greater than the carbide precipitation layer thickness; however, in the low extrusion ratio samples, the difference is within measurement error.

Figure 4.54 shows the undeformed and deformed Gleeble test specimens. Figures 4.55 and 4.56 show the bond development for the various extrusion conditions. After preheating, the microstructure is different than (Fig. 4.55) that observed from the shrink-fit billet slice subjected to the preheat cycle





**Fig. 4.54. Gleeble samples for deformation simulation.** From left to right, stock material (half of pair), low extrusion ratio simulation, high extrusion ratio simulation.



**Fig. 4.55. Interface between (left) 1020 steel and (right) 304 stainless steel after 2.5 h at 1200°C held at 100 lb-f in Gleeble Hydrowedge unit.** The sample was etched with agitated 60 mL HCl, 60 mL HNO<sub>3</sub>, and 60 mL distilled H<sub>2</sub>O for 30 s.

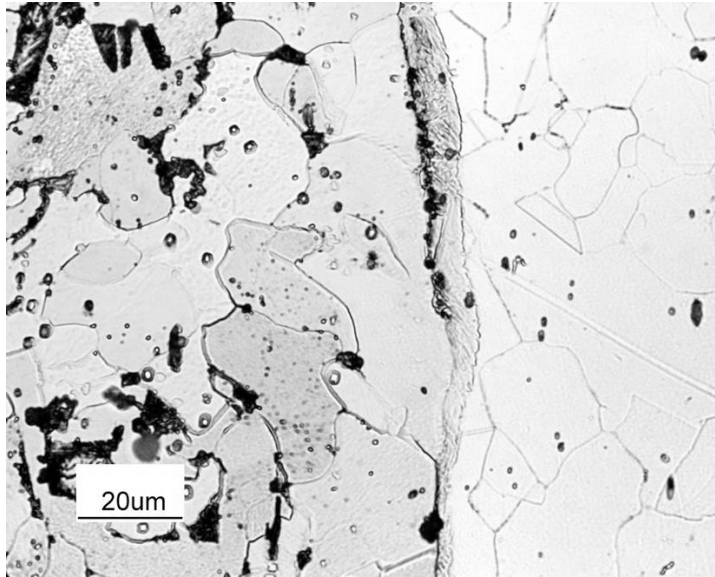


**Fig. 4.56. High magnification of the interface between (left) 1020 steel and (right) 304 stainless steel after 2.5 h at 1200°C held at 100 lb-f in Gleeble Hydrawedge unit and deformed to a strain of 2.74 at a strain rate of 22.8 s<sup>-1</sup> and air cooled. The sample was etched with agitated 60 mL HCl, 60 mL HNO<sub>3</sub>, and 60 mL distilled H<sub>2</sub>O for 30 s.**

(Fig. 4.48). The interface lacks the porosity and exhibits a martensite layer at the interface that is approximately 25- to 30-μm thick.

Figure 4.57 shows the low strain/strain rate interface after being reheated to 1100°C and furnace cooled. It can be observed that the microstructure closely resembles that from the actual extrudates

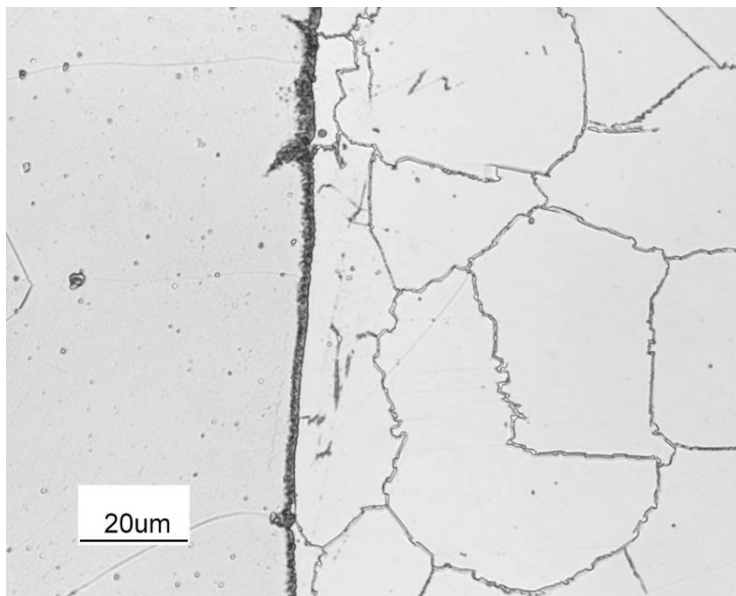


**Fig. 4.57. Light optical micrograph of the interface between (left) 1020 steel and (right) 304 stainless steel after 2 h at 1100°C held at 100 lb-f in Gleeble Hydrawedge unit and deformed to a strain of 1.2 at a strain rate of 2.10 s<sup>-1</sup> and air cooled. After cooling, it was reheated to 1100°C and furnace cooled. The sample was etched with agitated 60 mL HCl, 60 mL HNO<sub>3</sub>, and 60 mL distilled H<sub>2</sub>O for 30 s.**

produced using the low extrusion ratio. Figure 4.58 is a secondary electron micrograph that illustrates the carbide morphology at the interface, which is characteristic of pearlite in plain carbon steel.

After etching using Murakami's reagent at room temperature, chromium carbides are visible on the austenite grain boundaries of the stainless steel in both the actual and simulated extrusions (Figs. 4.59 and 4.60). No carbides are revealed at the interface or in the plain carbon steel.

When etched using the agitated solution of H<sub>2</sub>O, HCl, and HNO<sub>3</sub>, annealing twins and austenite grain boundaries are visible in the stainless steel, and banded pearlite and ferrite is visible in the plain carbon steel (Figs. 4.61 and 4.62). At the interface, a thin band of Fe<sub>3</sub>C/cementite is visible that is on the order of several microns thick. Due to the etching procedure, it can be concluded that the chromium carbides only form in the stainless steel at the grain boundaries in the vicinity of the interface, but do not form a layer at the interface itself.

Qualitative elemental maps were produced using EDS K $\alpha$ -lines for Fe, Ni, and Cr, and WDS using a LDEII crystal to map C. Figures 4.63 and 4.64 compare the maps for the actual and simulated bond interfaces respectively. For the actual extrudate, two C-rich layers can be observed near the bond: one layer that is located in the stainless steel that is also rich in Cr, and one layer that is C and Fe (Fig. 4.63).

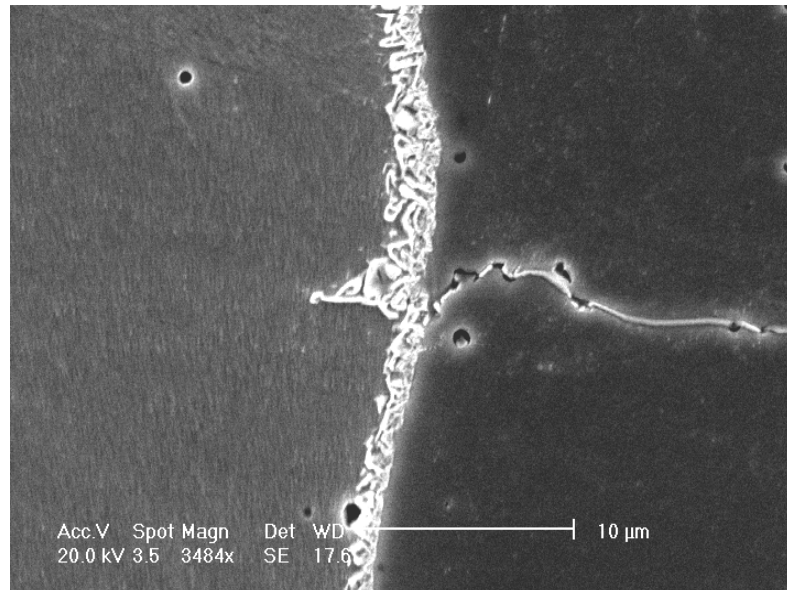


**Fig. 4.58. Scanning electron microscopy secondary electron image of the interface between (left) 1020 steel and (right) 304 stainless steel after 2 h at 1100°C held at 100 lb-f in Gleeble Hydrawedge unit and deformed to a strain of 1.2 at a strain rate of 2.10 s<sup>-1</sup> and air cooled. After cooling, it was reheated to 1100°C and furnace cooled. The sample was etched with agitated 60 mL HCl, 60 mL HNO<sub>3</sub>, and 60 mL distilled H<sub>2</sub>O for 30 s.**

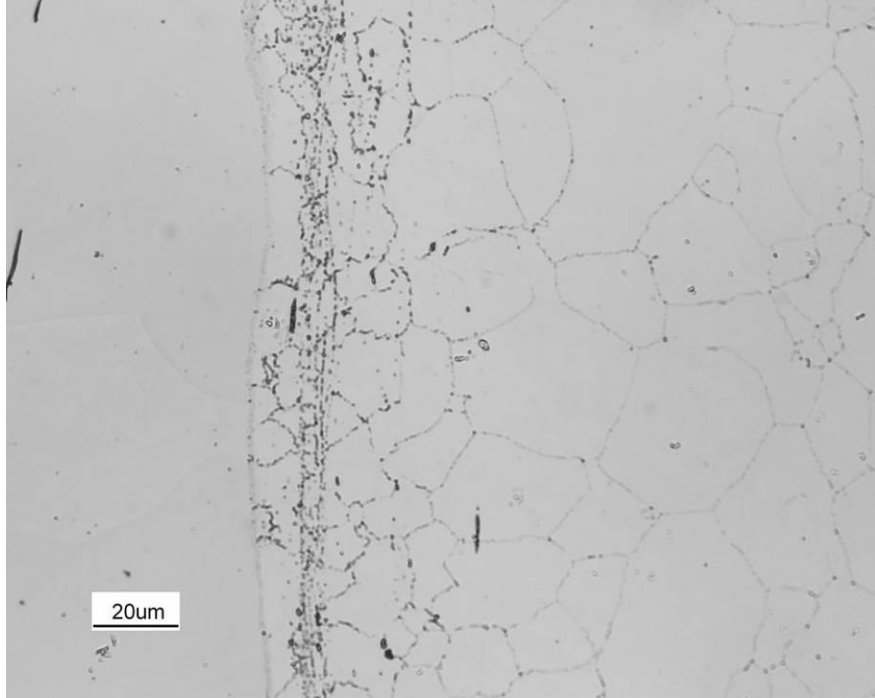


**Fig. 4.59.** Low strain/strain rate extrudate sample etched for 240 s using Murakami's reagent.

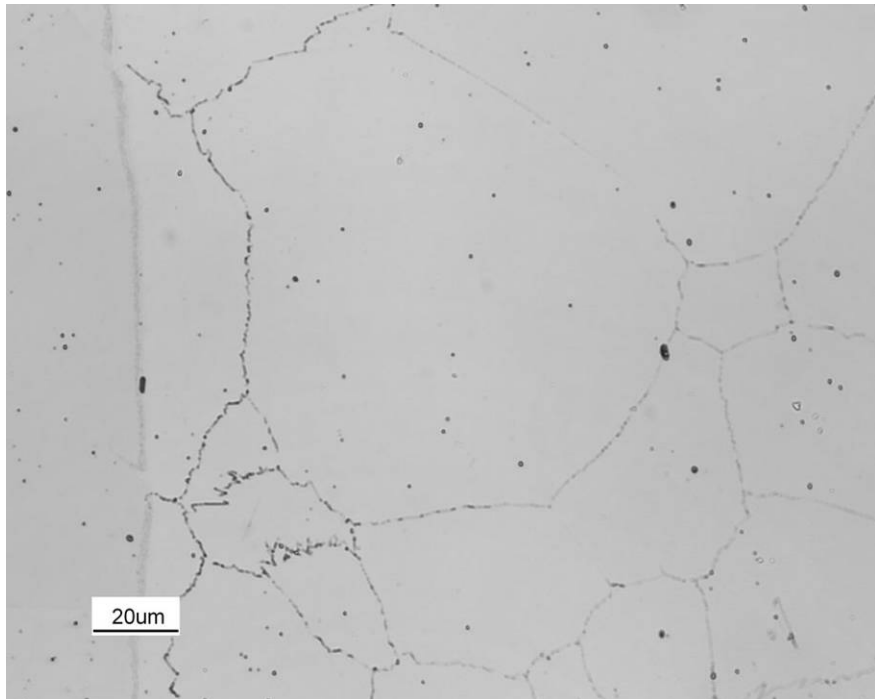


**Fig. 4.60.** Low strain/strain rate Gleeble simulated sample etched for 240 s using Murakami's reagent.

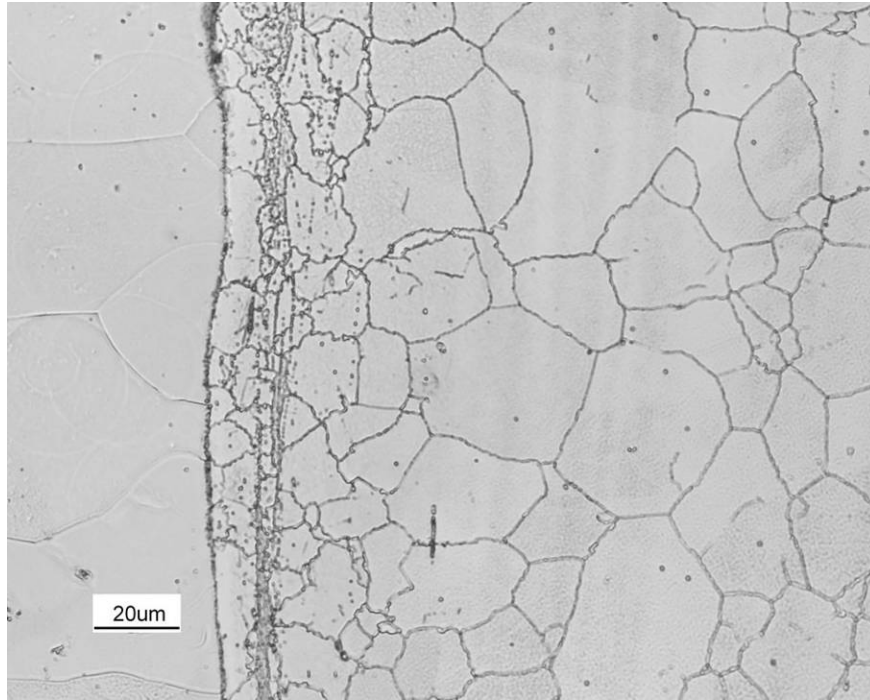


**Fig. 4.61.** Low strain/strain rate extrudate sample etched for 240 s using Murakami's reagent followed by 15 s using equal parts agitated  $\text{H}_2\text{O}$ ,  $\text{HCl}$ , and  $\text{HNO}_3$ . This same region is shown in Fig. 4.59.

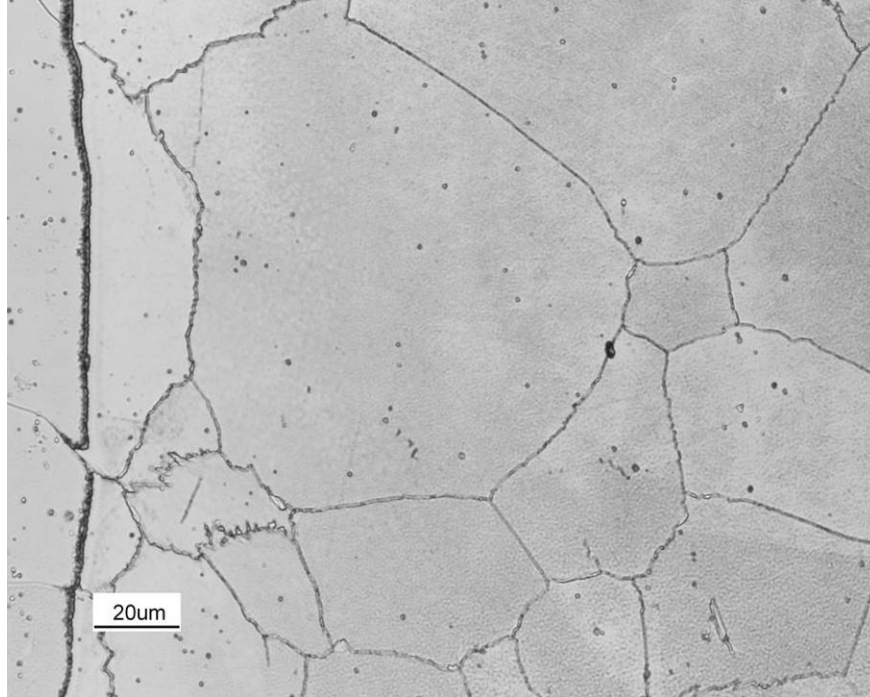


**Fig. 4.62.** Low strain/strain rate Gleeble simulated sample etched for 240 s using Murakami's reagent followed by 15 s using equal parts agitated  $\text{H}_2\text{O}$ ,  $\text{HCl}$ , and  $\text{HNO}_3$ . The same region is shown in Fig. 4.60.

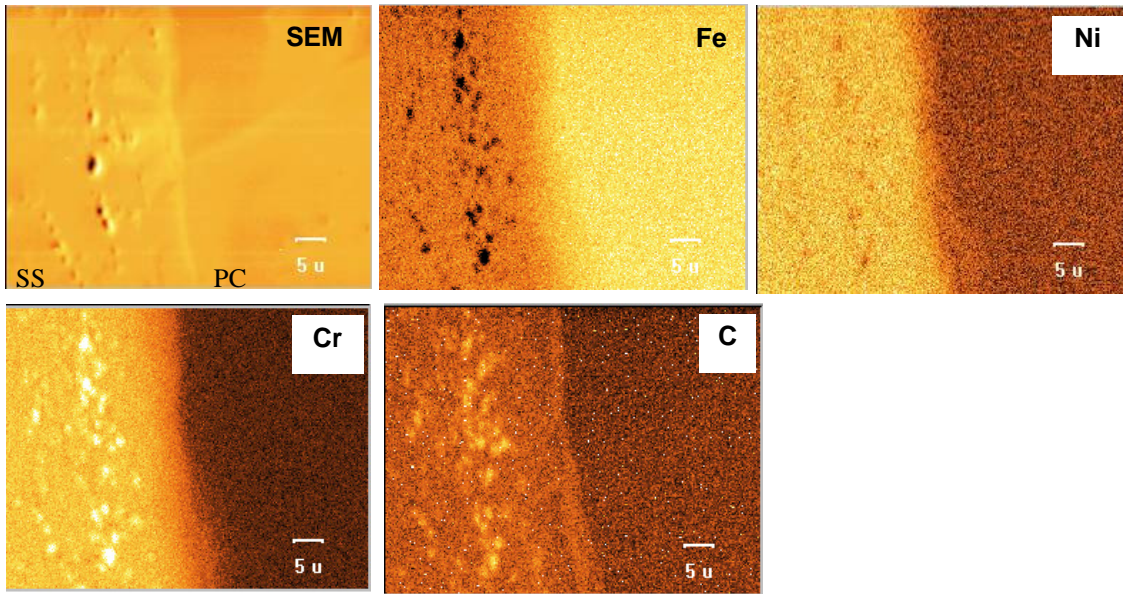


**Fig. 4.63. Qualitative elemental maps of the interface of the low strain/strain rate extrudate.** Stainless steel to left of interface, plain carbon steel to the right of the interface.

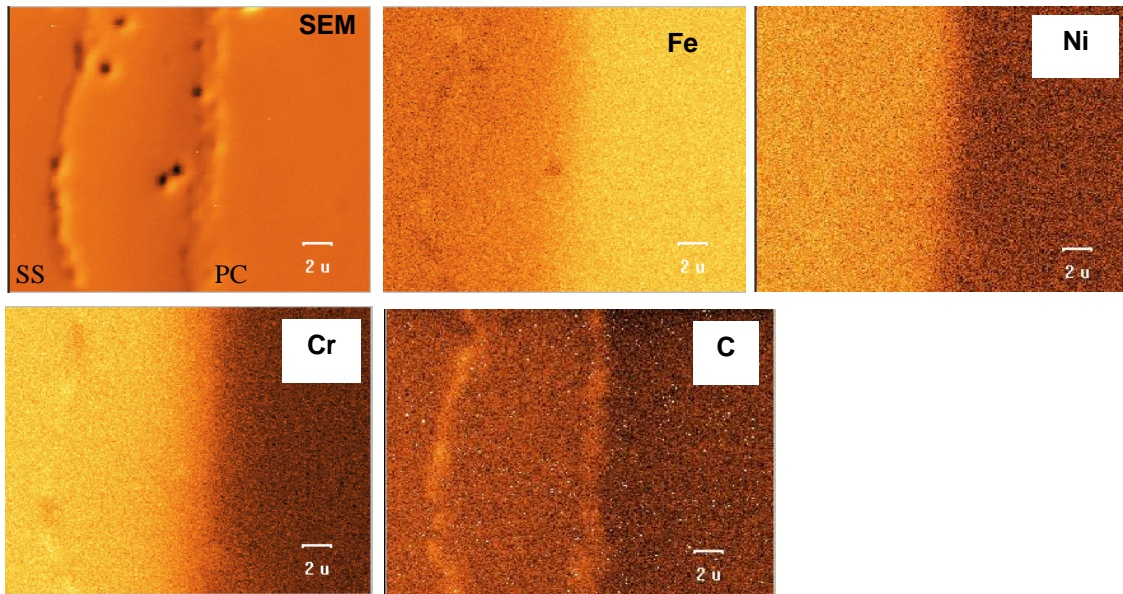


**Fig. 4.64. Qualitative elemental maps of the interface of the Gleeble simulated low strain/strain rate extrudate.** Stainless steel is on the left of interface; plain carbon steel is on the right of the interface.

In the simulated extrudate, the Cr-rich carbide layer does not appear as distinct carbides but rather as a thin band (Fig. 4.64). Quantitative line scans on the interface of the simulated preheat (Fig. 4.65) and simulated extrusion (Fig. 4.66) show a diffusion profile of Cr, Ni, and Mn with a gradient caused by transport from the stainless steel into the plain carbon steel. After deformation, the thickness of this diffusion layer is greatly reduced. Figure 4.67 shows the WDS line scan performed on the actual extrudate, which is comparable to the simulated extrusion. Cr shows the greatest diffusion distance.

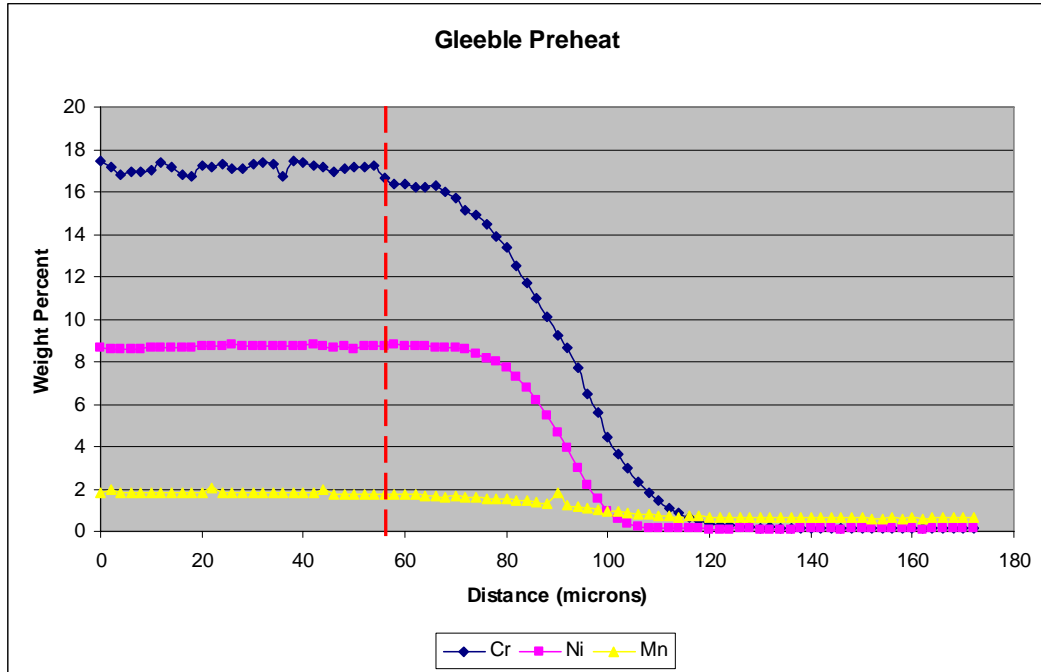


Fig. 4.65. Quantitative wavelength dispersive spectroscopy line scan across interface of sample subjected to 2 h at 1200°C in Gleeble and then is air cooled. Stainless steel is on the left of interface; plain carbon steel is on the right of the interface.

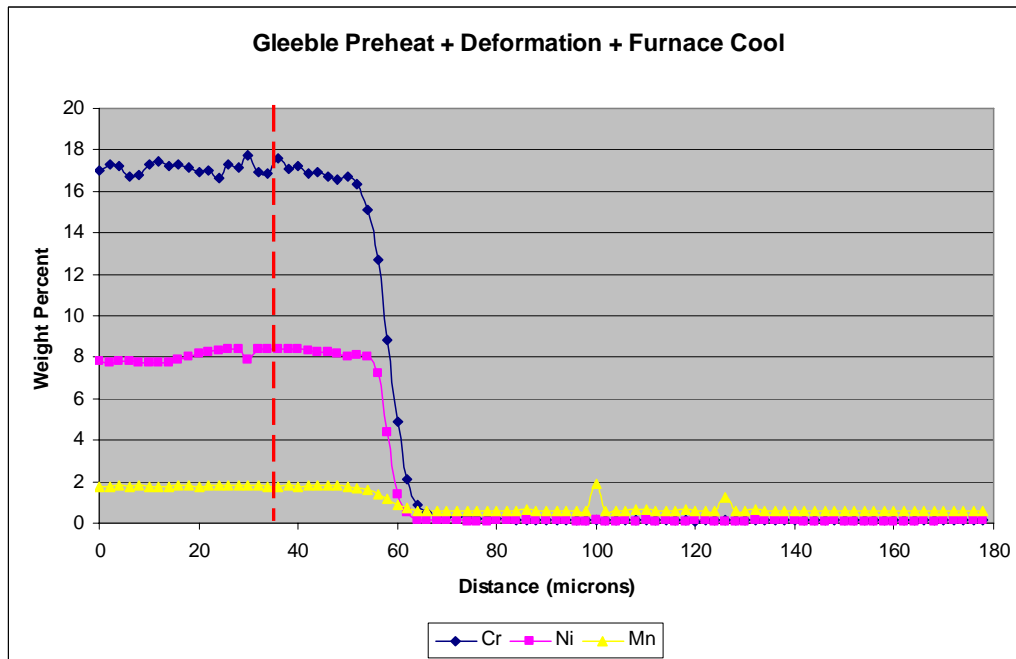
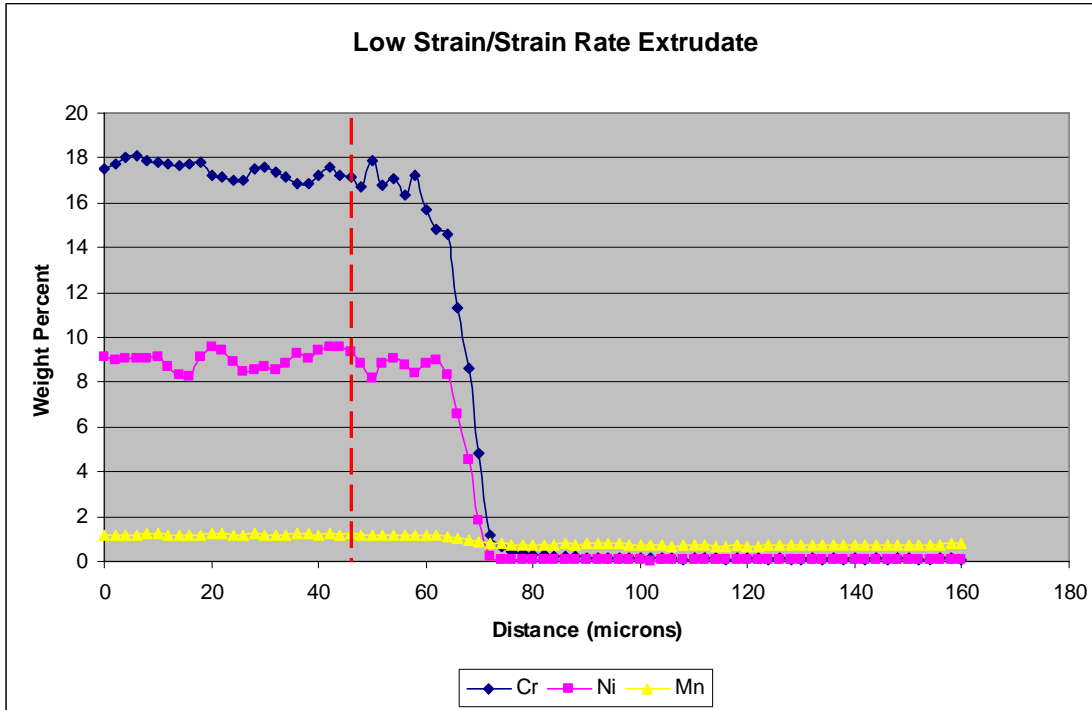
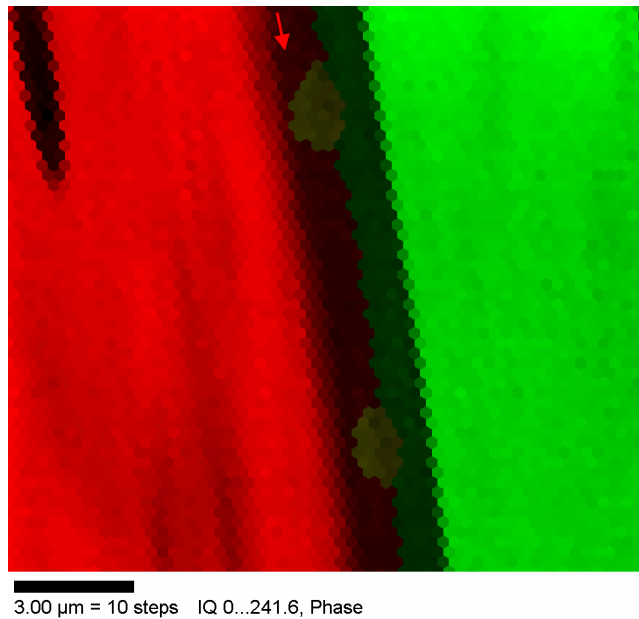


Fig. 4.66. Quantitative wavelength dispersive spectroscopy line scan across interface of sample subjected to 2 h at 1100°C in Gleeble and deformed according to the low strain/strain rate sample and is furnace cooled. Stainless steel is on the left of interface; plain carbon steel is on the right of the interface.



**Fig. 4.67. Quantitative wavelength dispersive spectroscopy line scan across interface of extrudate that has a designated low strain/strain rate.** Stainless steel is on the left of interface; plain carbon steel is on the right of the interface.

The EBSD analysis was performed on the regions directly adjacent to the bond. Figure 4.68 shows the phase map of the region, where the plain carbon steel is on the left and the stainless steel is on the right, and the interfacial layer composed of pearlite is represented by the dark region in the middle.



**Fig. 4.68. Electron backscatter diffraction phase map of interface.** Plain carbon steel is shown on the left, stainless steel on the right. Note the loss of image quality at the bond due to the profuse iron carbide layer. The arrow indicates the interface.



Figure 4.69 is the EBSD orientation map of the same region, and it shows orientations corresponding to the ferrite (plain carbon steel) and austenite (stainless steel). It should be noted that there is a distinct boundary between the two orientations, and that the plain carbon steel side corresponds to ferrite, further confirming that the dark carbide phase is composed of ferrite plus cementite.

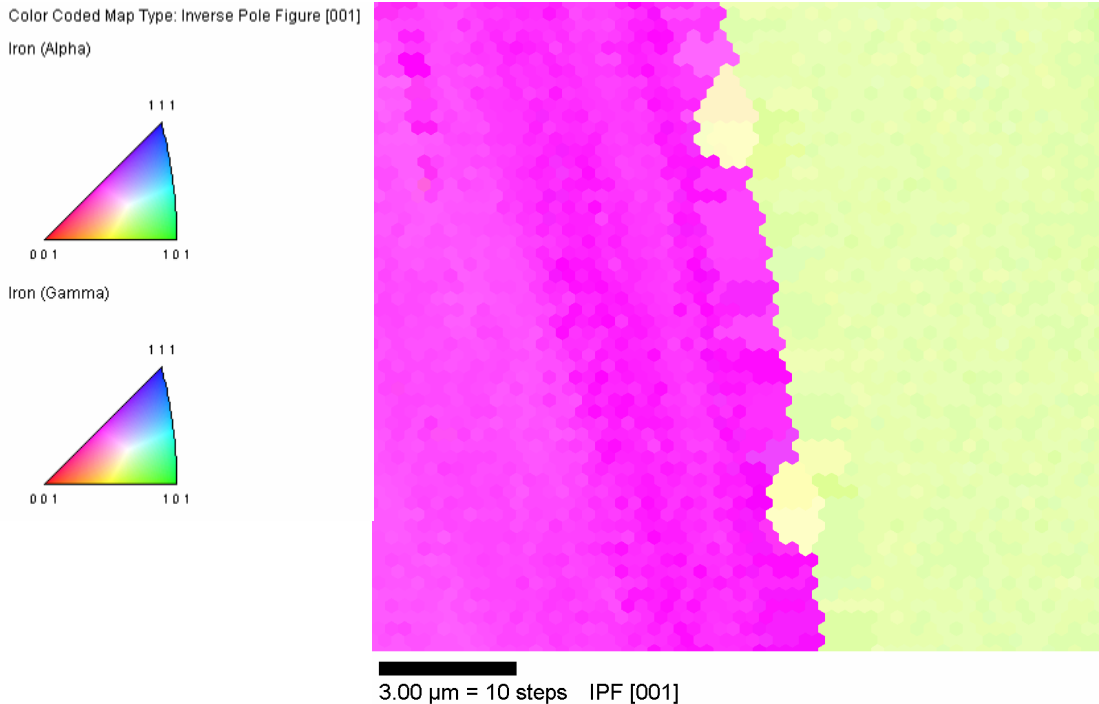


**Fig. 4.69. Electron backscatter diffraction orientation map and inverse pole figure of the regions directly adjacent to the interface.** Plain carbon steel (ferrite) is on the left; stainless steel (austenite) is on the right.

#### 4.3.6 Discussion of Results for Interface Study of Co-extruded Tubes

The interfacial bonding process can be separated into three different stages: primary bonding, bond-surface extension, and elimination of original joining surface.<sup>26</sup> Figure 3.11 is a schematic representation of the development of the interface and the different stages: (a) faying surfaces are covered by a layer of surface oxidation/film, (b) primary bonding: initial contact of surfaces causes break up of surface oxide as asperities deform locally, (c) bond-surface extension: bulk plastic deformation (metal flow) occurs which generates new film-free surface area, small amounts of film/oxide are still trapped in the interface, and (d) elimination of original surface: film is dissolved into solution, microstructural changes occur in the regions near the bond.

During primary bonding, Fig. 3.11 asperities and localized deformation act to break up surface oxidation and surface layers (surface layers are indicated by the heavy black line in the figure). This allows for metal-metal contact and the beginnings of the bond to develop. Fresh material is exposed, allowing for initial diffusion between the materials. Surface oxidation may be present as a result of room temperature or preheat surface oxidation. Oxides typically reduce diffusion of atomic species, which prevents a full adherent and tenacious bond between the two alloys. Pressure at the interface between the materials composing the pre-extruded bimetallic billet may result from either initial deformation/upsetting in extrusion or residual stresses from “shrink fitting” of billet components.

Prior to deformation, the chemical profile of the area near the interface resembles that shown in Fig. 4.65, which is measured on the bond that was simulated using the Gleeble with an isothermal sample hold. The affected region is approximately 45  $\mu\text{m}$  wide and exhibits a characteristic multi-element diffusion profile where Cr, Ni, and Mn are diffusing towards the plain carbon steel. If the material is quickly cooled (in the grips of the Gleeble unit for example) from the preheat temperature, a layer of martensite develops at the bond, approximately 30  $\mu\text{m}$  wide (Fig. 4.55). When the material is slowly cooled (air cooled outside the furnace) martensite does not form; instead, the layer exhibits ferrite and finely spaced pearlite (Fig. 4.48). Typically, it is believed that the preheat cycle does not result in large-scale diffusion bands.<sup>8</sup> In this situation, decarburization and sensitization of the plain carbon and stainless steel was not observed; however, a significant transformation layer is present.

Bond-surface extension, the second stage of the solid-state weld development, occurs when large-scale plastic deformation begins, as shown in Fig. 3.11(c). Plastic flow is governed by applied stress and the mechanical properties of the materials involved. Conservation of volume governs that the surface area between the two materials will increase with deformation for a process such as extrusion and axial flow. Bonding improves due to several different effects: surface films and impurity layers may dissolve and return to solution, diffusion of elements across the interface may take place, and atoms located near the interface may re-orient themselves to facilitate stronger bonding via grain boundary migration. As a result of deformation heating (internal material friction and external frictional forces) and temperature increase, these processes may be accelerated above the initial processing temperature.

After the material undergoes deformation (either from extrusion or upsetting as in the simulation), the width of the diffusional layer decreases to approximately 10  $\mu\text{m}$  wide and the change in composition is much more severe (Figs. 4.66 and 4.67). This is caused by the bond surface extension as a result of conservation of material volume. If the material is again rapidly cooled from the deformation temperature, as in the grips of the Gleeble unit, this layer transforms to martensite as shown in Fig. 4.56. In the bimetallic tubes produced at ORNL, the cooling time from extrusion temperatures was much greater and was on the order of several hours. To simulate this, one of the deformed Gleeble test specimens was placed in a furnace at the deformation temperature, held for several minutes to allow the dissolution of the martensite, carbides, and pearlite, and then was furnace cooled to 200°C, removed, and allowed to air cool to room temperature. The time-temperature (TT) profile is shown in Fig. 4.43. The long furnace cool does not significantly affect the chemical distribution but does affect the morphology of the phases that are present. The resulting microstructure strongly resembles that obtained in the industrial extrusion experiments and consists of several layers (listed in order starting in the plain carbon steel) as shown in Fig. 4.57.

1. Pearlite islands or pearlite bands with ferrite; bands occur in the longitudinal direction of the extruded sample.
2. A decarburized region of ferrite.
3. A thin, high-density pearlite band that forms in the low dT/dt samples or a martensite band observed in the high dT/dt samples.
4. Interface between the materials.
5. High-density precipitation region of Cr-rich carbides in austenite grain interiors and grain boundaries.
6. Low-density precipitation region of Cr-rich carbides on austenite grain boundaries.
7. Equiaxed austenite grain boundaries with annealing twins.

In the case where a relatively high cooling rate is achieved, a layer of martensite forms whose width corresponds to the diffusion layer thickness. When there is a slower cooling rate, the layer is composed of a high-density arrangement of Fe-rich carbides ( $\text{Fe}_3\text{C}$ ) or ferrite or pearlite.

Additionally, the profuse Cr carbide precipitation and corresponding decarburization occur only after deformation and during cooling.

The Cr diffusion distance is slightly larger than that for Ni and Mn due to the higher diffusivity. The effect of Mn, Cr, and Ni on transformation behavior of weld heat affected zones has been studied by Kasugai et al.<sup>32, 33, 34</sup> Cr, Ni, and Mn shift the ferrite and pearlite transformation regimes in a continuous cooling transformation (CCT) diagram to longer times. For Cr, any amount greater than 1%,<sup>33</sup> the effect was great on both the ferrite and bainite regions. At times longer than 60 s, Cr acted to reduce the likelihood of forming massive ferrites and normal pearlite; instead, bainite with fine cementite as well as degenerate or fine pearlite colonies formed. It was also shown that when the Cr level is below 4%, Cr carbides do not tend to form in the HAZ.<sup>33</sup> Mn (studied up to 2%) causes changes in the transformation behavior in a similar manner to Cr. Ferrite, pearlite, and bainite transformation regions in the CCT diagram were shifted to longer times and lower temperatures with an increasing amount of Mn, most considerably up to 1%.<sup>34</sup> During long cooling times (greater than 60 s), both bainite and ferrite transformations were affected the most. Ni also caused similar behavior in changing the CCT curves.<sup>21</sup>

During furnace cooling, the material was above the austenite transformation (A3) temperature (900°C) for approximately 2400 s. This provided ample time for the material to miss both the martensite and bainite curves, regardless of the Cr, Mn, or Ni content. Quantitative WDS line scans show Cr values ranging from 15 to approximately 0.2 wt % traversing across the bond starting in the stainless steel. Likewise, Ni values range from 7 to 0.1 and Mn values from 1.2 to 0.6 wt %. This data is taken directly from the region of the sample where the interface is located in the extrudates (simulated and real).

The final stage of the weld development is the elimination of the original joining surface, as shown in Fig 3.11(d). Microstructural and subgrain changes such as recrystallization, grain growth, transformations, precipitation, and diffusion may occur. These reactions render the initial near bond new microstructure and the metallic bond is completed. A new microstructure is noted in Fig. 3.11(d) by the cross-hatched region. This final state may occur concurrently with the other stages and well after extrusion during the return to room-temperature.

The development of a martensitic band in dissimilar ferrous alloys has been well documented in fusion welding processes<sup>30,35</sup> and to a lesser extent in co-extruded products.<sup>16,17,18,20</sup> A Schaeffler diagram is commonly employed to determine near-weld microstructure that occurs as a result of chemical transport during processing. Various alloying elements are converted to a Ni or Cr equivalent according to Eqs. (3) and (4), respectively.

$$Ni_{eq} = \%Ni + 30\%C + 30\%N + 0.5\%Mn \quad (3)$$

$$Cr_{eq} = \%Cr + \%Mo + 1.5\%Si + 0.5\%Cb \quad (4)$$

Nickel acts as an austenite stabilizer along with C and Mn, while Cr acts as a ferrite stabilizer along with Mo, Si, and Cb. Values for  $Ni_{eq}$  and  $Cr_{eq}$  for the stock materials can be seen in Table 4.8. Figure 4.7 illustrates the placement of the stock materials on the Schaeffler diagram with a linear dashed-line connecting the two materials. It can be observed that this line crosses several regions where martensite is predicted to form under normal fusion arc welding cooling conditions. A significant region of martensite exists only between the two base alloys. Measurement of Mn, Cr, Mo, Si, and Cb can easily be performed quantitatively using the EMPA analysis; however, the quantitative measurement of light elements such as C is difficult. For this research, a maximum and minimum  $Ni_{eq}$  value can be calculated by using the nominal C values of the stock alloys as the limits. Others have

**Table 4.8. Cr and Ni equivalent values for stock materials**

| Material            | Ni <sub>eq</sub> | Cr <sub>eq</sub> |
|---------------------|------------------|------------------|
| 1020 plain carbon   | 6.1              | 0                |
| 304 stainless steel | 10.5             | 18.3             |

shown<sup>16,17,18,20</sup> that it is reasonable to expect the formation of a layer of martensite when co-extruding austenitic and ferritic ferrous alloys concurrently at the temperatures used in this project. Figures 4.49 through 4.52 show the bond microstructure after extrusion for both the high and low extrusion ratios. A thin (on the order of several microns) dark carbide band exists where the two materials are joined. In Fig. 4.55, the simulated, undeformed, diffusional bond exhibits a thick (~45  $\mu\text{m}$ ) martensite layer. After deformation simulations using the Gleeble with parameters predicted by FEM, the band is on the order of 1 to 10  $\mu\text{m}$  thick (Fig. 4.56). The cooling rate experienced by the simulated tests is greater than that for the industrially produced extrudates. Because of the large thermal mass as well as insulation in order to evenly cool the industrial tubes to prevent large thermal stresses from developing, slow enough cooling rates exist and martensite does not form. To further characterize the cementite/ferrite layer, EBSD analysis was performed in the region of the bond. Mapping of the region resulted in accurate characterization of ferrite and austenite for the plain carbon and stainless steel halves of the bond; however, poor image contrast and signal was captured at the actual interface (Fig. 4.68). The lighter regions indicate good pattern quality, while darker regions indicate poorer pattern quality. The results from orientation analysis showed that the poor contrast region was indeed a ferritic structure (Fig. 4.69). The high density of iron carbides were not able to be indexed under the operating conditions of the microscope and caused the loss of pattern quality as observed in Fig. 4.68. The results support the hypothesis that the layer is a mixture of ferrite and cementite, as was shown through traditional metallography and as expected via the work of Kasugi et al.<sup>32,33,34</sup>

EMPA analysis of this area shows Cr and Ni equivalent values calculated using Eqs. (3) and (4) that fall in the martensite region of the Schaeffler diagram. For the Ni equivalent calculations, a maximum and minimum carbon concentration is assumed based upon the amount in the stock materials. Both the maximum and minimum Ni equivalent value falls within the martensite region. After application of strain, which can be considered to occur immediately at 2 h, and for a duration of approximately 5 to 10 s (in the industrially prepared tubes), the diffusion layer is elongated and reduced in thickness, depending upon the strain. Upon cooling in the Gleeble, the layer transforms to martensite, at temperature equal to the martensite transformation start temperature ( $M_s$ ) at a short time after deformation ( $t > 2$  h). This structure is observed in the simulated bond shown in Figs. 4.56 but not in the industrially prepared extrudates. Since these samples were relatively small and were produced using a thermomechanical simulator, they cooled to room temperature relatively quickly, producing the martensitic layer. In the case of large industrial extrudates, a much greater time (on the order of several hours) was needed for the material to equilibrate to room temperature. Immediately after extrusion, the low extrusion ratio tubes were placed into a container of Vermiculite (an insulating medium) to slowly cool them while the high extrusion ratio samples were cooled via mildly forced air. There is a danger of the materials developing extremely high internal stresses during rapid cooling that is attributed to the difference in thermal expansion between the ferritic and austenitic structures. Additionally, there is a much larger thermal mass in the industrial extrudates that was not present in the thermomechanical simulation tests. This slow cool to room temperature allows for ample time to exceed the critical cooling rate and instead forming a decarburized region in the plain carbon steel and a thin layer of C-rich, Cr-containing carbides ( $M_7C_3$ ) nearest the interface as well as additional chromium carbide precipitation ( $M_{23}C_6$ ) on austenite grain boundaries in the stainless steel. These layers were extensively characterized by others in similar material and processing situations.<sup>16,17,20</sup> In the high  $dT/dt$  simulated extrusion, there are very few carbides precipitated on the

austenite grain boundaries, and the decarburized layer in the plain carbon steel is virtually nonexistent, supporting the hypothesis that this layer does not form as a result of the preheat treatment nor from the deformation process but rather from being cooled from deformation temperature to room temperature. This was verified by reheating one of the low strain/strain rate Gleeble samples to the deformation temperature (1100°C) and allowing it to furnace cool. The existing microstructure was allowed to solutionize, and after the long cooling time, it appeared similar to the structure obtained from the industrially extruded materials. Figure 4.70 shows the solvus line for precipitation of  $\text{Cr}_{23}\text{C}_6$  in 304 stainless steel. As carbon content increases, the solvus temperature increases. Due to the high processing temperature, carbon diffuses readily into the stainless steel. The greater the increase in concentration and the higher the temperature, the greater the amount of chromium carbides that forms. Longer times at the processing temperatures and slower cooling rates increase the carbide formation.

The difference in thickness of the carbide precipitation layer in the 304 stainless steel and the decarburized layer in the plain carbon steel can be partially explained by the higher solubility of carbon in austenite versus ferrite. When considering the binary Fe-C combination, the maximum solid solubility of C in Fe for the bcc phase (alpha ferrite) is only 0.022 wt %, while the maximum solid solubility of C in face-centered cubic Fe (gamma austenite) is 2.14 wt %. The discrepancy between the low and high extrusion ratio in layer thicknesses can be explained by the amount of time taken to reach room temperature after extrusion. The low extrusion ratio extrudates were placed in Vermiculite and allowed to cool, while the high extrusion samples were cooled by mildly forced air. The forced air resulted in a shorter amount of time to reach room temperature, thus, the amount of time for diffusion for the various elements was shortened.

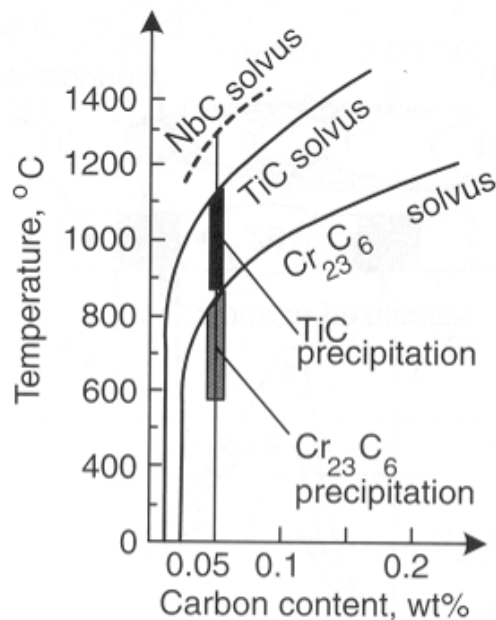


**Fig. 4.70. Solvus curve for  $\text{Cr}_{23}\text{C}_6$  in 304 stainless steel.** (Source: *Principle and Technology of the Fusion Welding of Metals*, Vol. 2, Mechanical Engineering Publishing Co., Peking, 1979.)

Porosity at the bond is not present in the Gleeble simulation due to the increased force (445 N) imposed to hold the two materials together (pressure of 5.7 MPa). In the billet, the only stresses were resultant from the shrink fitting procedure and were likely lower. High pressures increase the densification rate in diffusion bonding.<sup>26</sup>

Qualitatively, the simulated bond microstructure is the same as the microstructure of the extruded material. Both exhibit a decarburized region of plain carbon steel in the vicinity of the bond, as well as a ferrite/pearlite structure in the bulk of the material. In the extruded samples, the pearlite is banded as a result of the processing history, while the pearlite is in the form of discrete islands in the simulated extrusion sample. At the new interface between the two materials, the simulated and the actual extrudate show a layer of cementite. In the simulated sample, this layer is thicker, which is explained by the much slower cooling rate from the deformation temperature (approximately four times longer). The effect of the longer cooling time is also reflected in the larger size of the austenite grains of the stainless steel adjacent to the bond in the simulated extrusion. Cr-rich carbide precipitation on the austenite grain boundaries as well as in the interiors near the interface is common to both samples. In addition to the difference in the cooling of the two samples from deformation temperature, there is a difference in the strain distribution. Effective strain and strain rate values were taken from the FEM simulations and used as deformation parameters for the physical (Gleeble) simulations. Due to the use of the effective values, as well as the cylindrical specimen geometry, the physical simulation samples undergo a relatively homogeneous strain path at the interface. Radial flow occurs in the upsetting with uniform strain in both the x- and y-axis. In the actual extrusion process, this strain is non-homogeneous and is much larger in the y-axis. The simulated samples undergo negative (compressive) strain in the major deformation axis; whereas, the strain is positive (tensile) in the actual extrudate.

Summary of the microstructural development is shown in Fig. 4.71. At the preheat temperature, the microstructure of both the plain carbon and stainless steel is austenite. Cr, Ni, and Mn begin to diffuse from the 304 stainless steel into the plain carbon steel, while C and Fe begin to diffuse into the stainless steel. This creates a decarburized region in the plain carbon steel adjacent to the interface, while a region enriched in Cr, Ni, and Mn begins to form in the plain carbon steel adjacent to the interface. As the material is cooled below the A3 temperature, the austenite in the plain carbon steel begins to transform to ferrite, and begins to eject C into the surrounding austenite. Directly adjacent to the bond in the plain carbon steel, a band of austenite is stabilized for longer times to lower temperatures due to the increase in Ni due to diffusion from the stainless steel. This layer becomes enriched in C and eventually transforms into pearlite at low cooling rates or martensite at high cooling rates. As the temperature reaches the solvus temperature for the Cr-rich carbides (temperature dependant on C content as well as the type of Cr carbide), the carbides begin to precipitate in the stainless steel. Near the interface, where there is a higher amount of carbon, the precipitates form on both the grain boundary and the grain interiors; farther away from the interface, the carbides form only on the austenite grain boundaries.

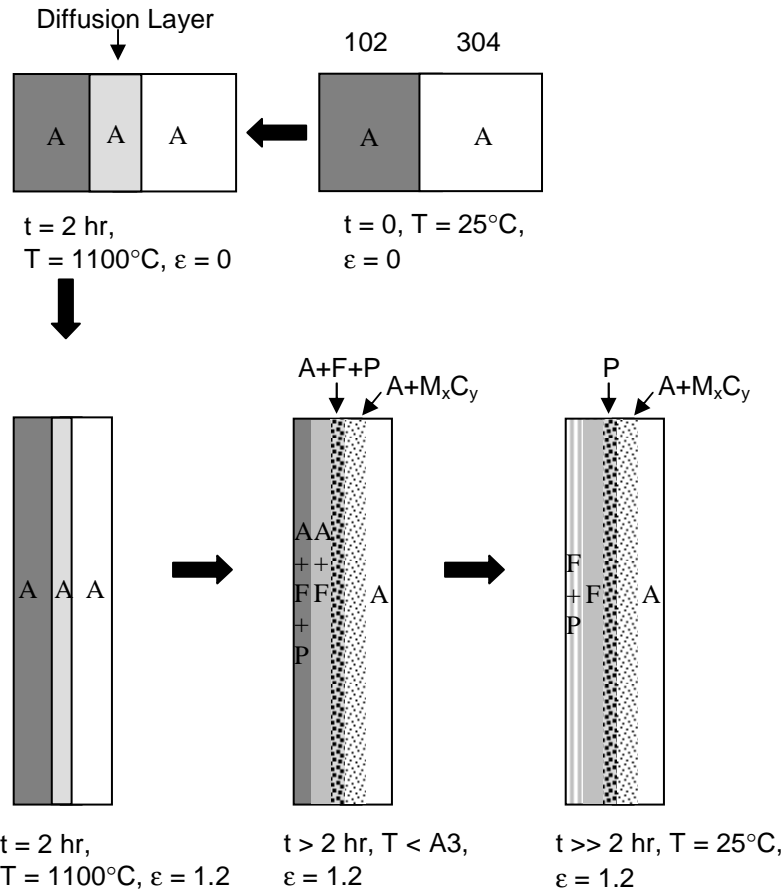


**Fig. 4.71. Microstructural development schematic for the co-extruded stainless and plain carbon steel.** P—pearlite, A—ausenite, F—ferrite, MxCy—Cr-rich carbides.

#### 4.3.7 Conclusions from Interface Study of Co-extruded Tubes

1. Simulation of interface microstructural development show that the majority of carbide precipitation in the stainless steel and decarburization of the plain carbon steel occurs after extrusion during the cool down to room temperature. At higher cooling rates, such as those seen in the Gleeble bonding experiment, a layer of martensite develops at the interface. The effect of strain and strain rate is minimal on the formation of these features other than changing the thickness of the layer after the preheat treatment due to bond surface extension/layer thickness compression. The preheat TT was not long enough to remove all porosity at the interface under normal shrink-fit pressures.
2. Chromium carbides precipitate on the austenite grain boundaries in the stainless steel, and iron carbides precipitate in the ferrite matrix in the plain carbon steel side of the interface.
3. Accurate simulation of bond microstructural development can be performed via a combination of FEM modeling to determine state variables and thermomechanical means, provided that the proper TT profile is followed, including the anticipated cool down to room temperature during industrial processing.
4. Sensitization of the stainless steel can be minimized by using higher cooling rates after extrusion, but subsequent heat treatments will be needed to temper the martensite layer that may develop.





## 5. Accomplishments

### 5.1 Technical Accomplishments

1. A multitool approach has been designed and successfully implemented to simulate the co-extrusion process. Numerical modeling was used to simulate the extrusion process and to understand the metal flow during the co-extrusion process as well as to understand the influence of new billet design involving a shortened core. The FEM simulations were used to also determine state variables (strain and strain rate) that are used to physically model the bonding and interface development that occurs between different alloys during the co-extrusion process. This cross-disciplinary approach provides geometrical and physical metallurgy results that provide understanding of the co-extrusion process as well as to insight into designing the billet and processing steps.
2. Specific conclusions related to the individual components of the research are presented below:
  - a. The FEM code DEFORM-2D is an effective tool for experimental design for hollow cross-sectional co-extrusion products and can minimize the number of validation tests needed. Geometrical results from both FEM simulations and extrudates produced at ORNL are in good agreement for tube co-extrusion using two billet materials, carbon, and 304 stainless steel.
  - b. Extrudates produced using **traditional billet geometry** show core thicknesses greater than or equal to the initial core thickness in the billet during the initial part of extrusion. In both the low and high extrusion ratio cases, the ratio of core-to-sleeve material increases with decreasing core length in the initial billet. This value becomes closer to the ratio in the initial billet. Proportionate flow occurs when the two ratios are equal.
  - c. Reduction in scrap material (due to out-of-tolerance geometry), and therefore energy consumption, can be realized by utilizing the **core-shortening method**, developed in this project. Shortening the core material length by 8–20% can be effective in managing sound material flow. Core shortening acts to cause the sleeve material to upset into the recessed region of the billet so that concurrent flow is achieved. Less material is lost to early flow out of the die and thus steady-state core thickness flow conditions are reached sooner. The actual amount of shortening is governed by the specific processing parameters for the intended extrudate geometry. During steady state material flow, there is little or no difference in core material distribution between extrudates produced from a billet with a full length or shortened core. Maximum savings can be achieved with the amount of upsetting being in balanced with the flow of the core material into the die orifice, which is also influenced by the die angle.
  - d. The maximum eccentricity in reference to wall thickness in co-extruded ferrous tubes generally occurs within the first 10% of the extrudate. In this project, the extrudate end also showed the eccentricity but it is an artifact of using a graphite block to clear the extrusion through the die.
  - e. The **core shortening method** of this project does not negatively affect wall thickness eccentricity, even in the case where the initial core length in the billet is recessed 20%. Eccentricity results were similar regardless of core length in the initial billet except for a few cases where the back-end defect affected eccentricity.
  - f. Through the use of simulation to identify interface microstructural development, it is concluded that the majority of carbide precipitation in the stainless steel and decarburization of the plain carbon steel occurs after extrusion during the cool down to room temperature. At

- higher cooling rates, such as those seen in the Gleeble bonding experiment, a layer of martensite develops at the interface. The effect of strain and strain rate is minimal on the formation of these features other than changing the thickness of the layer after the preheat treatment due to bond surface extension/layer thickness compression. The preheat TT was not long enough to remove all porosity at the interface under normal shrink-fit pressures.
- g. Chromium carbides precipitate on the austenite grain boundaries in the stainless steel, while iron carbides precipitate in the ferrite matrix in the plain carbon steel side of the interface.
  - h. Accurate simulation of bond microstructural development can be performed through a combination of FEM modeling to determine state variables and thermomechanical means provided that the proper TT profile is followed including the anticipated cool down to room temperature during industrial processing.
  - i. Sensitization of the stainless steel can be minimized by using higher cooling rates after extrusion, but subsequent heat treatments will be needed to temper the martensite layer that may develop.
3. The core-shortening billet design method developed in this project uses 8–20% less billet material for core and also reduces scrap in the final product by having to cut shorter lengths because of extrusion defects as opposed to the traditional billet design. These aspects produce savings in energy from a combination of (a) the use of less material in initial billet assembly, (b) the use of less energy in the preheating and extrusion process because of reduced billet mass, and (c) the reduction of the amount of scrap produced from extrusion defects in the final product.

## 5.2 Publications and Presentations

1. P. Kazanowski and W. Z. Misiolek, *Rudy Metale*, R.47, No. 10–11, pp. 485–488 (2002).
2. P. Kazanowski, W. Z. Misiolek, and V. K. Sikka, *Materials Science Forum*, Vols. 426–432, pp. 3795–3800 (2003).
3. P. Kazanowski, W. Z. Misiolek, M. E. Epler, and V. K. Sikka, *Informatyka w Technologii Materialow*, Vol. 1, No. 3–4, pp. 125–138 (2003).
4. P. Kazanowski, M. E. Epler, and W. Z. Misiolek, *Journal of Materials Science & Engineering A*, Vol. 369, No. 1–2, pp. 170–180 (2004).
5. M. E. Epler and W. Z. Misiolek, “Optimization of Co-extrusion of Ferrous Material Tubes,” *Proceedings of XXIV Colloquium on Metal Forming*, Planneralm, Austria, March 2005.
6. P. Kazanowski and W. Z. Misiolek, “Investigation of the Bi-metal Tube Cross-section Geometrical Stability after Extrusion with the Mandrel,” XII Scientific Conference on Production Technologies for Tubes and Pipes in Non-Ferrous Metals Industry, Zakopane, Poland, November 21, 2002.
7. P. Kazanowski, W. Z. Misiolek, and V. K. Sikka, “Analysis of the Influence of the Initial Billet Geometry and Die Design on the Product Geometry During Bi-material Tube Extrusion,” THERMEC 2003 International Conference on Processing and Manufacturing of Advanced Materials, Madrid, Spain, July 7–11, 2003.
8. W. Z. Misiolek, “Using Microstructure Characterization and Modeling to Optimize Physical Properties in Metal Forming,” Boston Scientific, Metals Technology Team, October 5, 2005, Plymouth, MN.

## 5.3 Development of Students

This project resulted in completing a Ph.D. thesis. The student trained from this project is currently employed at Carpenter Technology Corporation because of skills developed during this project. One postgraduate student involved in the project was hired by the extrusion division of Hydro Aluminum, a major aluminum company.

## 6. Summary and Conclusions

### 6.1 Summary

The research and development work for this project was conducted by a team consisting of Lehigh University and ORNL members. Industrial support was provided by Plymouth extruded products.

The project goals were focused on physical and numerical analysis of the extrusion process for the production of bimetallic tubes. The project goals were met through a multitool approach to simulate the extrusion process for bimetallic tubes. The numerical model used was FEM code DEFORM-2D, which described the material flow during the extrusion process. The FEM simulations, based on DEFORM-2D were also used to predict the state variables of strain and strain rate that are used to physically model the bonding and interface development that occurs between the alloys during the co-extrusion process.

The results of multitool approach were validated by preparing bimetallic billets composed of 1020 carbon steel for the outside and 304 stainless steel for the core. The 1020 validation was performed on two types of billets: (1) the **traditional design**, where core and outside are the same length and (2) a **new design**, where the core is reduced in length by 8–20%. The geometrical results from the FEM simulations were validated on experimental extrusions by measuring the thickness of the inside tube as a function of distance. There was good agreement for all conditions tested. In addition to wall thickness, measurements were also made for the wall thickness eccentricity and no adverse effects were noted from the new billet design using core shortening.

The FEM simulation of the state variables was validated by detailed investigation of the microstructure at and on either side of the interface of the co-extruded tubes. The simulation and microstructural analysis indicated that the majority of carbide precipitation in 304 stainless steel and decarburization of the carbon steel occurs after extrusion during cool down to room temperature.

The accurate simulation of the microstructure was possible through the FEM modeling to determine the state variables of strain and strain rate, and thermomechanical means, such as Gleeble, provided the means to apply the TT profile, including the anticipated cool-down profile, to room temperature from the extrusion temperature.

The core-shortening billet design method, developed in this project, uses 8–20% less billet material for core and also reduces scrap in the final product by having to cut shorter lengths because of extrusion defects as opposed to the traditional billet design. These aspects produce savings in energy from a combination of (a) the use of less material in initial billet assembly, (b) the use of less energy in the preheating and extrusion process because of reduced billet mass, and (c) the reduction in the amount of scrap produced from extrusion defects in the final product.

### 6.2 Conclusions

- Use of the simulation based on FEM code DEFORM-2D was successful in predicting the geometrical changes of wall thickness as a function of tube length. Based on the validated simulation method, a new billet design based on **core shortening** was developed with significant reduction in scrap produced during the traditional billet design.

- The FEM simulation of the state variables of strain and strain rate was successful in predicting microstructure development at the bimetallic tube interface.
- The reduction in scrap of the bimetallic tube, based on multiple simulation tools when applied to commercial production of bimetallic tube, has a potential for significant savings in energy.
- The project team of Lehigh University and ORNL was very successful in carrying out this project because of the unique characterization facilities at Lehigh University and the unique facility of the hot-extrusion press at ORNL.
- The project was carried out as a Ph.D. thesis and the training from this project has led the student to accept a job at Carpenter Technology Corporation in the United States.
- The project provided an opportunity to a postdoctoral fellow to gain experience in the simulation of extrusion of bimetallic billets. This postdoctoral fellow is now employed at an aluminum company.

### **6.3 Commercialization Aspects, Plans, Status, and Barriers**

There was no formal commercialization effort undertaken in this project. However, based on papers presented at technical meetings and the U.S. Department of Energy's description of this project on its web site has led to possible benefits from this project to bimetallic tubing producers. One of these producers is Farmer's Marine Copper Works whose staff contacted us in August 2006 (see letter in Appendix) for the outcome of our project. As can be seen from their letter, the information generated from this project could be critical in meeting their customer requirements for a bimetallic system produced from copper and steel. Our plans are to meet with staff at Farmer's Marine Copper Works and further explore how best the outcome from this project can be utilized.

There have also been strong interactions with Plymouth Extruded Shapes regarding this project. ORNL staff has visited their facility, and they have visited the research facilities at Lehigh University.

It is anticipated that the commercial interest in the outcome of this work will further increase as additional presentations are made at technical meetings and as students graduated with Ph.D. degrees from this project start to further disseminate the outcome of this project to their industry employers.

One of the barriers in commercialization of this project could be the access of DEFORM-2D software at companies and dedicated staff to run this type of software. However, project team members intend to continue to run simulation trials for interested companies by using the software available at Lehigh University.

## 7. Recommendations

The project has accomplished nearly all of the proposed goals. However, the following is a list of recommendations to take further advantage from this project:

- Data on possible post treatment of bimetallic tubes and its effect on interfacial bond are needed.
- Possible secondary processing steps are needed for processing of bimetallic tubes to their final size.
- Billet design detail where one of two metals is a powder is the next step that needs to be addressed for bimetallic tube processing.



## 8. References

1. Laue, K., and Stenger, H. *Extrusion*, Metals Park, American Society for Metals (1981).
2. Gildengorn, M. S., *Advanced Performance Materials* **2**, Issue 1 (1995), 79–87.
3. Latham, E. P., Meadowcroft, D. B., Pinder, L., *Mater. Sci. Technol.* **5**, No. 8 (1989), 813–815.
4. Apperley, M. H., Sorrell, C. C., and Crosky, A., *Journal of Materials Processing Technology* **102**, Issues 1–3 (2000), 193–202.
5. Alcaraz, J. L., *International Journal of Plasticity* **15** (1999), 1341–1358.
6. Alcaraz, J. L., Gil-Sevillano, J. L., and Martinez-Esnaola, J. M., *J. Mat. Proc. Techno.* **61** (1996), 265.
7. Sliwa, R., *Journal of Materials Processing Technology* (Netherlands) **67**, Issues 1–3 (1997), 29–35.
8. Sliwa, R., *Materials Science and Engineering A*. **A135**, No. 1–2 (1991), 259–265.
9. Avitzur, B., *Handbook of Metal-Forming Processes*, Wiley, New York (1983).
10. Bandar A., R., Misiolek, W. Z., Kloske, K. E., and Jeong, T. H., *Proceedings of the Seventh International Aluminum Technology Seminar*, Chicago, Illinois, Aluminum Extruders Council and Aluminum Association **2** (2000), 223.
11. E. Erman, E., and Semiatin, S. L., *Physical Modeling of Metalworking Processes*, The Metallurgical Society, Inc., Warrendale, PA (1987), 1.
12. Kazanowski, P., and Misiolek, W. Z., *Rudy Metale* **R.47**, No. 10–11(2002), 485–488.
13. Kazanowski, P., Misiolek, W. Z., and Sikka, V. K., *Materials Science Forum* **426–432** (2003), 3795–3800.
14. Kazanowski, P., Misiolek, W. Z., Epler, M. E., and Sikka, V. K., *Informatyka w Technologii Materialow* **1**, No. 3–4 (2003), 125–138.
15. Epler, M. E., and Misiolek, W. Z., *Proceedings of XXIV Colloquium on Metal Forming*, Planneralm, Austria (2005).
16. Gomez, X., and Echeberria, J., *Materials Science and Engineering A* **348**, Issues 1–2 (2003), 180–191.
17. Gomez, X., and Echeberria, J., *Materials Science and Technology (UK)* **6**, Issue 2, (2000), 187–193.
18. Lopez, B., Gomez, X., and Echeberria, J., *Key Engineering Materials* **127**, Part 1–2 (1997), 695–702.
19. Lopez, B., Gutierrez, I., and Urcola, J. J., *Materials Science and Technology* **12**, Issue 1 (1996), 45–55.
20. Gutierrez, I., Urcola, J. J., Bilbao, J. M., and Villar, L. M., *Materials Science and Technology (UK)* **7**, No. 8 (1991), 761–769.
21. Osakada, K., Limb, M., and Mellor, P. B., *International Journal of Mechanical Science* **15** (1972), 291–307.
22. Story, J. M., Avitzur, B., and Hahn, Jr., W. C., *J. Eng. Ind. (Trans. ASME B)* **98**, No. 3 (1976), 909–913.
23. Zoerner, W., Austen, A., and Avitzur, B., *Transactions of the ASME: Journal of Basic Engineering* **94 C–D** (1972), 78–80.
24. Holloway, C., Sheppard, T., and Bassett, M. B., *4th International Conference on Production Engineering* **18–20**, Tokyo (1980), 736–745.
25. Avitzur, B., Wu, R., Talbert, S., and Chou, Y. T., *J. Eng. Ind. (Trans. ASME)* **104**, Issue 8 (1982), 293–304.
26. “Coextrusion Welding,” ASM Handbook, Vol. 6: Welding, Brazing, and Soldering, ASM International, USA (1993).
27. Sliwa, R., *J. Mat. Proc. Techno.* **67** (1996), 29.

28. Kazanowski, P., Epler, M. E., and Misiolek, W. Z., *Journal of Materials Science & Engineering A* **369**, No. 1–2 (2004), 170–180.
29. Gooch, T., *Weld. Inst. Res. Bull.* **18** (1977), 343–349.
30. Kusko, C. S., DuPont, J. N., and Marder, A. R., *Proceedings from Materials Solutions Conference 1999 on Joining of Advanced and Specialty Materials 1–4*, USA (1999), 125–131.
31. Vander Voort, G. F., *Metallography, Principles and Practice*, McGraw-Hill, New York (1984).
32. Kasugai, T., and Inagaki, M., *Transactions of National Research Institute for Metals* **24**, No. 1 (1982), 22–35.
33. Kasugai, T., and Inagaki, M., *Transactions of National Research Institute for Metals* **23**, No. 3 (1981), 191–203.
34. Kasugai, T., and Inagaki, M., *Transactions of National Research Institute for Metals* **22**, No. 4 (1980), 258–265.
35. Kou, S., *Welding Metallurgy*, John Wiley and Sons, Inc. (2003).



## **Appendix: Farmer's Marine Copper Works Letter**



# FARMER'S MARINE COPPER WORKS

LTD.

P.O. BOX 748 - 1908 STRAND  
GALVESTON, TEXAS 77553

PETRO-CHEMICAL FABRICATION  
MARINE AND INDUSTRIAL REPAIRS

GALVESTON (409) 765-6261  
HOUSTON (281) 488-2655  
FAX (409) 765-8513

## Mechanical Engineering Department

August 26, 2005

Professor Wojciech Z. Misiolek  
Loewy Chair in Materials Forming and Processing  
Institute for Metal Forming  
Lehigh University  
5 E. Packer Avenue  
Bethlehem, PA 18015

**Subject:** Numerical Analysis of Extrusion Process for Production of Bimetallic Tubes

Dr. Misiolek

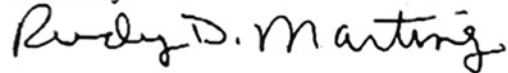
Per our discussion on the above subject matter I wanted to follow up on those discussions with this brief synopsis. The work that you and your colleagues are conducting could be of vital interest to us pertaining to a very large industrial size project that we are in receipt from a very good client of ours. Because we have had to execute many nondisclosure confidential agreements, I can not go into all of the exact details but here are some of the high lights of what the project entails.

The project, which could be an on going one, consists of a drawing process of a bimetallic system of copper and steel. The bimetallic system will be in very long lengths of about twenty (20) to thirty (30) feet long. The purpose of this bimetallic system is to achieve a thermal and electrical circuit to be used in onshore and offshore drilling oil and gas operations. The copper tubing which is draw over the steel tubing serves as the electrical and thermal conductor of energy while the steel serves as the strength mechanism once many of the joints are connected and lowered into a oil or gas well. The client is, of course a major oil and gas producer and we have been chosen for the project because of expertise and engineering knowledge base of copper and copper derivatives. Further we currently have a very elementary drawing system for such a bimetallic system that we have adapted for test runs of the bimetallic system, for our client, but by no means can the current system be used for a full blown commercial application. We are in the first stages of mechanical design of our commercial system.

Because of the aspects of induced plasticity during the drawing process we have developed some simple plasticity models both analytically and numerically ( using nonlinear finite element analysis) but we are lacking in combining both the what goes on at both the micro and macro scale. Using concepts of continuum mechanics only gets us half of the physical reality of the process. As such our models only address the macro scale so we are indeed interested and hope that your research into these similar matters at the academic level would be something that industry could prosper from. It is research of the sort that you are conducting that would be very important to us, as well as others in industries, who have limited access to laboratory and physical testing methodologies.

I truly hope that the results of your research at the academic level can be shared with industry since it would be extremely valuable to my employer as well as me, as a practicing engineer, in order for us to keep pace with the exponential change that technology seems to be taking.

Cordially

A handwritten signature in black ink that reads "Rudy D. Martinez". The signature is written in a cursive style with a large, prominent initial "R".

Dr. Rudy D. Martinez, Ph.D., P.E.  
Senior Mechanical Engineer and Engineering Manager